Radiative transfer in the exosphere of Saturn's moon Titan

vorgelegt von Diplom-Physiker
Pascal Hedelt
Berlin

Von der Fakultät II - Mathematik und Naturwissenschaften
der Technischen Universität Berlin
zur Erlangung des akademischen Grades
Doktor der Naturwissenschaften
Dr. rer. nat.

genehmigte Dissertation

Promotionsausschuss:
Vorsitzender: Prof. Dr. rer. nat. M. Dähne
Berichter/Gutachter: Prof. Dr. rer. nat. H. Rauer
Berichter/Gutachter: Prof. Dr. rer. nat. E. Sedlmayr

Tag der wissenschaftlichen Aussprache: 01.09.2009

Berlin 2009
D 83

Diese Arbeit wurde im Institut für Planetenforschung am Deutschen Zentrum für Luft- und Raumfahrt e.V. in Berlin-Adlershof in der Abteilung "Extrasolare Planeten und Atmosphären" unter Betreuung von Frau Prof. Dr. H. Rauer angefertigt.

ZUSAMMENFASSUNG

Diese Arbeit beschäftigt sich mit der Wasserstoffverteilung in der Exosphäre des Saturnmondes Titan. Grundlage dieser Arbeit sind Messungen des HDAC Instrumentes (Hydrogen Deuterium Absorption Cell), welches an Bord der Cassini-Raumsonde das D/H Verhältnis direkt durch die Messung der Emissionslinien von atomarem Wasserstoff und Deuterium im Ultravioletten bei 121.567 nm bzw. 121.533 nm bestimmen sollte.

Mit HDAC wurden am 26. Dezember 2005 beim neunten Titanvorbeiflug der Cassini-Sonde Messungen vorgenommen. Leider konnte die Menge an Deuterium in der Absorptionszelle nicht bestimmt werden, sodass HDAC seinen vorgesehen Zweck nicht erfüllen konnte. Die Menge an Wasserstoff in der Zelle ist jedoch bekannt, so dass zumindest die Wasserstoff-Lyman-α Messungen verwendet werden kann, um Titan's Exosphäre zu untersuchen.

Ziel dieser Arbeit war es, die HDAC Messungen zu simulieren und somit Rückschlüsse auf die Exosphäre von Titan ziehen zu können, wie z.B. die Verteilung von atomarem Wasserstoff in der Exosphäre.

In dieser Arbeit wurde ein Modell der Titanexosphäre entwickelt, welches atomaren Wasserstoff und Methan berücksichtigt. Für das Exosphärenmodell wurden zwei unterschiedliche Dichtemodelle gewählt, welche die Dichteverteilung von Wasserstoff in der Exosphäre unterschiedlich berechnen und insbesondere in der unteren Exosphäre voneinander abweichen. Der Strahlungstransport durch die Modell-Exosphäre wurde mit Hilfe der Monte-Carlo-Methode gelöst.

Detaillierte Strahlungstransportrechnungen haben gezeigt, dass die HDAC Messungen mit Dichteprofilen aus beiden Dichtemodellen reproduziert werden können. Dabei konnte gezeigt werden, dass das von HDAC gemessene Signal aus Höhenschichten 2000 km oberhalb der Exobase stammt. Die mit den Dichtemodellen bestimmten Exobasendichten unterscheiden sich dabei um einen Faktor vier. Somit konnte keine Aussage darüber getroffen werden, welches Dichtemodell die HDAC Messung am besten beschreibt. Dennoch liegen die bestimmten Exobasendichten im Bereich der in der Literatur zu findenden Werte.

Beruhend auf den Ergebnissen dieser Arbeit wird HDAC im Jahr 2010 bei zwei weiteren Titanvorbeiflügen erneut verwendet werden, und somit noch genauere

Daten für die Bestimmung der Exosphärendichte und Temperatur liefern. Strahlungstransportrechnungen für diese Vorbeiflüge wurden ebenfalls in dieser Arbeit durchgeführt.

ABSTRACT

This work focuses on the distribution of atomic hydrogen in the exosphere of Saturn's moon Titan. This work is based on measurements performed by the "Hydrogen Deuterium Absorption Cell" (HDAC) aboard the Cassini spacecraft, that should directly determine the D/H ratio from the UV emission of atomic hydrogen and deuterium at 121.567 and 121.533 nm, respectively.

HDAC measurements were performed on December 26, 2005 during the ninth Titan flyby of the Cassini orbiter. Unfortunately the amount of deuterium in the absorption cell could not be determined. Thus, the purpose, HDAC was designed for could not be achieved. For this reason, HDAC has performed measurements only once. However, the amount of atomic hydrogen in the absorption cell is well known, hence the data using only the hydrogen cell can be used in order to investigate Titan's exosphere.

This work aims at simulating the HDAC measurements performed in order to investigate Titan's exosphere, e.g. to determine the distribution of atomic hydrogen. A model of Titan's exosphere including atomic hydrogen and methane has been developed and the transfer of solar radiation is calculated in order to simulate the HDAC measurements. The radiative transfer is solved using the Monte Carlo method. For the exospheric model, two different atomic hydrogen density distributions were applied, which determine the distribution in the exosphere by different approaches. Density profiles calculated by both models mainly differ in the lower exosphere.

It was found that the HDAC measurements can be fitted using density profiles calculated by both exospheric density distribution models for the radiative transfer calculations. Detailed investigations however showed that the signal measured by HDAC originates at much higher altitudes of about 2000 km above the exobase. Nevertheless the best fitting atomic hydrogen exobase densities of both models differ by a factor of 4. A strong noise pattern was found in the measurements avoiding a more accurate determination of the atomic hydrogen distribution in Titan's exosphere. However, the inferred exobase densities are in the range of literature values.

As a result of this work, HDAC will be used again during two future flybys in 2010, providing more accurate measurements for the determination of densities and temperatures in Titan's exosphere.

CONTENTS

LIST OF FIGURES

LIST OF TABLES

List of Abbreviations used in this work

General abbreviations:
ASI - Agenzia Spaziale Italiana
ESA - European Space Agency
C/A - Closest approach
CEM - Channel Electron Multiplier
CFR - Complete Frequency Redistribution
GCM - General Circulation Model
ISO - Infrared Space Observatory
FOV - Field of view
JPL - Jet Propulsion Laboratory
NASA - National Aeronautics and Space Administration
PAH - Polycyclic Aromatic Hydrocarbon
PFR - Partial Frequency Redistribution
SORCE - Solar Radiation and Climate Experiment
SZA - Solar zenith angle

Abbreviations for instruments aboard the Voyager 1 probe:
IRIS - Infrared Radiometer Interferometer and Spectrometer

Abbreviations for instruments aboard the Huygens probe:
DISR - Descent Imager/Spectral Radiometer
DWE - Doppler Wind Experiment
GCMS - Gas Chromatograph Mass Spectrometer
HASI - Huygens Atmospheric Structure Instrument

Abbreviations for instruments aboard the Cassini orbiter:
CIRS - Composite Infrared Spectrometer
HDAC - Hydrogen Deuterium Absorption Cell
HGA - High Gain Antenna
ISS - Imaging Science Subsystem
LGA - Low Gain Antennas
INMS - Ion Neutral Mass Spectrometer
VIMS - Visual and Infrared Mapping Spectrometer
UVIS - Ultraviolet Imaging Spectrograph

1. INTRODUCTION

Planetary research nowadays not only focuses on the new and exciting subject of extrasolar planets - the planets and moons within the Solar System are still not fully understood and ongoing targets of investigation. Objects in the Solar System have the advantage of allowing space missions to probe atmospheric or even surface conditions in-situ, which will, of course not be possible for extrasolar planets. The Cassini mission for example was started in 1997 and arrived at Saturn in 2004. Henceforth, new insights into Saturn and its moons will be made. The most interesting subject of the mission, however, is Titan, the only moon in the entire Solar System having a dense atmosphere.

From the chemists' point of view, Titan's atmosphere is often believed to have certain parallels with the early Earth atmosphere with a carbon and nitrogen based chemistry, although at a much lower temperature (see e.g. Neish et al. 2009; Raulin 2008; Simakov 2001). The Miller-Urey experiment and several following experiments have shown that with an atmosphere similar to Titan's and with the addition of UV radiation, complex molecules and polymer substances can be generated, which are thought to be the main precursor molecules for life as we now it.

Besides the rocky planets Mercury, Venus, Earth and Mars, Titan may be a very good example of a possible extrasolar terrestrial planet, that could be found in the near future, even representing a glimpse at the evolution of planet Earth.

The first detection of an extrasolar planet around a main sequence star in 1995 (51 Peg b, Mayor and Queloz 1995) gave planetary research an insight into the architecture of other planetary systems, questioning the state-of-the art models of planetary formation. More and more planets have been found over the years, with more than 350 planets so far. As instruments get better and better, the focus of extrasolar planet research now shifts from detecting these planets to investigate them. As in-situ investigations of these planets are not possible, the planetary research is forced to investigate them by their spectral appearance and orbital evolution. Their spectral appearance allows for the determination of the basic atmospheric parameters using ra-

diative transfer methods (see e.g. Segura et al. 2003; Kaltenegger et al. 2007; Ehrenreich et al. 2006).

The mass range for which detection methods are sensitive, is steadily decreasing and the detection of an Earth-mass planet is now in reach: three planets with masses close to that of Earth (0.02, 3.81, 4.13 $M_\oplus$) were detected in 1992 around the pulsar PSR 1257+12 (Wolszczan and Frail, 1992) and recently three planets with 1.9, 5.3 and 5.7 Earth masses have been detected around the star Gliese 581 (Udry et al., 2007). Clearly the discovery of an Earth twin is very unlikely, nevertheless one might find terrestrial exoplanets which feature a comparable atmospheric composition to the planets in our Solar System or even like Titan. Radiative transfer calculations therefore represent a necessary tool to investigate not only exoplanetary atmosphere but also the atmospheres of known planets and moons in our Solar System.

All planetary bodies in the Solar System were initially formed from the subsolar nebula, hence the initial ratio of atomic deuterium (D) to hydrogen (H) was about the same in the entire Solar System (see e.g. Horner et al. 2008). Since atomic hydrogen is lighter than deuterium, it can more easily escape from a given atmosphere and hence deuterium is enriched, of course depending on the escape mechanism. Measurements of the current ratio of deuterium to hydrogen of a given body therefore provide information about the evolution of the atmosphere as well as of the abundances in the Solar System.

The D/H ratio of Titan's atmosphere so far was determined by measuring the relative abundances of CH_3D/CH_4, HD/H_2 and C_2HD/C_2H_2. However the inferred values differ: in total a higher D/H ratio can be inferred from acetylene (C_2HD/C_2H_2) and deuterated hydrogen (HD/H_2) with respect to methane (CH_3D/CH_4). Coustenis et al. (2007) and Coustenis et al. (2008) argue that the enrichment of deuterium occurs during the photolysis of methane, which produces acetylene and molecular hydrogen.

The Hydrogen Deuterium Absorption Cell (HDAC, Esposito et al. 2004) aboard the Cassini orbiter was thus designed to determine the D/H ratio of Titan by directly measuring the hydrogen and deuterium Lyman-α emission of Titan. Unfortunately, due to contamination of the deuterium absorption cell, only the hydrogen Lyman-α emission was detected. However, the data measured by HDAC can be used in order to investigate Titan's atomic hydrogen corona.

The aim of this work is to investigate Titan's exosphere by simulating the

HDAC measurements performed during the ninth Titan flyby of the Cassini orbiter in December 2005. For this purpose first the HDAC data measured during is analyzed. Afterwards a model of Titan's exosphere is developed and the transfer of solar radiation through the exosphere is calculated. Performing a parameter study, the exospheric parameters that best fit the measurements will be determined and thus Titan's exosphere will be investigated in detail. Furthermore calculations will be performed for future Titan flybys, during which HDAC will be used again.

In **Chapter 2** a general overview of Titan is given, including a review of the lower atmospheric properties as well as a detailed description of Titan's exosphere. In this chapter also atmospheric escape mechanisms are also discussed, as well as the D/H ratio in the Solar System and in Titan's atmosphere.

Chapter 3 introduces the general radiative transfer problem and discusses solutions to the radiative transfer equation. An introduction to the Monte Carlo method is given. Additionally sample calculations for a plane-parallel atmosphere are shown.

Chapter 4 describes the Cassini/HDAC instrument in detail and introduces the measurement principle. Calibration measurements are reviewed and the measurements performed during the T_9 Titan flyby of the Cassini mission are presented. This chapter also focuses on the data analysis of the measurements.

Chapter 5 presents two different models for the calculation of the density distribution of atomic hydrogen within the exosphere used for the radiative transfer calculations. The general differences between both models are discussed.

Chapter 6 describes the radiative transfer model used in this work for the calculation of resonance scattering of solar radiation within Titan's exosphere, which calculates the path of single photons through the exosphere and simulates the measurement performed by HDAC during the flyby.

In **Chapter 7** the Monte Carlo calculations are summarized. A parameter study is performed and the statistics of the Monte Carlo output are discussed in order to investigate the response of the emitted radiation to different exospheric parameters.

In **Chapter 8** simplified analytical radiative transfer calculations including only single scattering are performed for the validation of the Monte Carlo radiative transfer model. With this simplified model the parameter variations performed in the previous chapter are repeated. A quantitative and

qualitative comparison to the Monte Carlo calculations is drawn.
Finally in **Chapter 9** the model calculations performed are compared to the data measured by HDAC in order to find the best fitting exospheric parameters. Using these parameters, calculations are performed for the measurement during the two future Titan flybys T_{66} and T_{67} in 2010, during which HDAC is planned to be used again.
The results of this work are summarized in **Chapter 10** followed by an outlook in **Chapter 11** in which possible applications of absorption cells like HDAC as well applications of the exospheric radiative transfer model are discussed.
In the **Appendix A** a glossary can be found in which important phrases used in this work are explained. **Appendix B** introduces the Liouville equation that is used for the calculation of atomic hydrogen densities in the exosphere. **Appendix C** describes the effect of radiation pressure on the distribution of atomic hydrogen in Titan's exosphere. **Appendix D** shows how to create photons equally distributed on a sphere. Finally in **Appendix E** a simple flow chart of the entire Monte Carlo radiative transfer model is presented, including the model part which calculates the distribution of scattering points, as well as the model part which simulates the flyby of HDAC.

2. TITAN

This chapter first gives an overview about Titan's orbital and atmospheric characteristics in section 2.1. In this section also the space missions that have examined Titan are reviewed. In section 2.2 a detailed description of Titan's surface and atmospheric properties is given. Section 2.3 introduces atmospheric escape mechanisms, followed by a description of Titan's exosphere in section 2.4, on which this work focuses. Finally in section 2.5 an introduction on D/H ratios in the Solar System as well as on Titan is given.

2.1 Overview

Saturn's biggest moon Titan is the largest moon after Ganymede in the entire Solar System. It orbits Saturn at an average distance of 20.3 Saturn radii (1,221,870 km) every 15.95 days, and was discovered on March 25, 1655 by Christiaan Huygens. See Table 2.1 for a summary of Titan's basic physical parameters. Like the Moon or many of the other gas giant satellites, Titan's orbital period is identical to its rotational period. Titan is thus tidally locked in synchronous rotation with Saturn. Its orbital eccentricity is 0.0288, and the orbit is inclined at 0.348° relative to the Saturnian equator. The surface temperature and pressure were measured by Fulchignoni et al. (2005) and Harri et al. (2006) being 93.7 K and 1.467 bar (compared to 1.013 bar for Earth), respectively. Titan is thus the only moon in the Solar System having a dense atmosphere. The atmosphere consists mainly of molecular nitrogen (N_2) and methane (CH_4). Titan is covered by a thick organic hydrocarbon haze, appearing orange in the visible (see Figure 2.1). This obscuring haze was particularly frustrating for planetary scientists following the NASA Voyager mission encounters in 1980 and 1981, avoiding any investigations of the lower atmosphere and surface.

Apart from the Earth, Titan is the only body in the Solar System with a nitrogen dominated atmosphere. It hosts an organic chemistry, seasonal and diurnal variations as well as condensation phenomena and dynamical processes in the atmosphere (e.g. Lebonnois et al. 2003; Bird et al. 2005;

Flasar et al. 2005; Atreya et al. 2006; Achterberg et al. 2008).

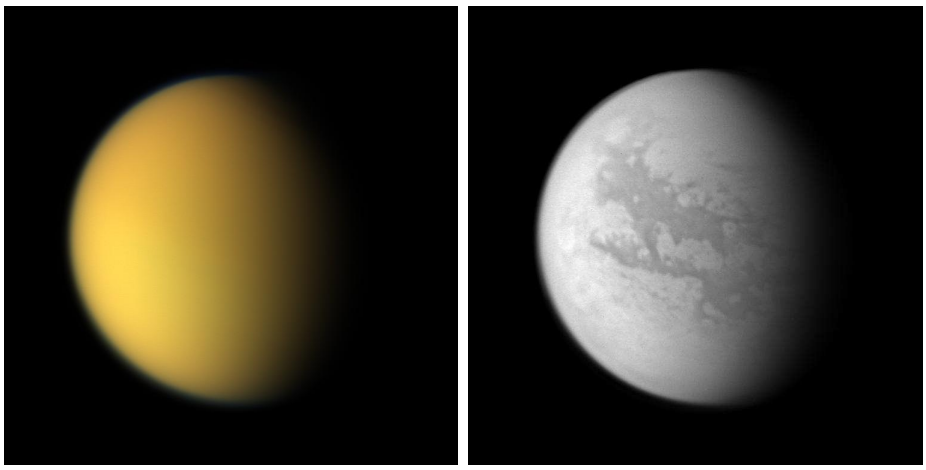

Fig. 2.1: Different views of Titan. The left image shows approximately what Titan would look like to the human eye: a hazy orange globe surrounded by a tenuous, bluish haze. The orange color is due to hydrocarbon particles which make up Titan's atmospheric haze, whereas haze in the upper atmosphere preferentially scatters blue and ultraviolet wavelengths of light. In the right image Titan is shown, as seen from Cassini at 0.9 μm, a near-infrared wavelength that allows Cassini to see through the hazy atmosphere and down to the surface. Image credits: NASA/JPL/Space Science Institute

The presence of a significant atmosphere was first suspected by Josep Comas Solà, who observed distinct limb darkening on Titan in 1903. However, Gerard Kuiper was the first one who proved the existence of an atmosphere in 1944 using spectroscopy. He concluded that methane was the most abundant constituent of Titan's atmosphere due to its appearance in the spectrum. Recent measurements have determined the global mean atmospheric abundances to be 98.4% N_2, 1.6% CH_4 and traces of other gases such as hydrocarbons (Teanby, 2005). Titan features a completely different atmospheric composition to that of Earth: the breakup of methane in the upper atmosphere by the Sun's ultraviolet light and the coupled chemistry between nitrogen and carbon leads to high abundances of nitrogen and carbon compounds (Wilson and Atreya, 2004). Due to the low temperatures in Titan's atmosphere, water ice does not sublimate, so that the atmosphere is nearly free from water vapor (a mole fraction of $8^{+6}_{-4}{\cdot}10^{-9}$ at an altitude of 400 km was found by Coustenis et al. 1998). The low hydrogen abundance is caused by the low surface gravity allowing hydrogen to escape from Titan's atmosphere. This is critical for the photochemistry, since it allows higher hydrocarbons to build up, which would otherwise be recycled back into methane by hydrogen.

Several space missions have examined Titan in the last decades:

- Pioneer 11 was the first satellite, which took close-up images of Titan on September 2, 1979.
- In the 1980s the Voyager missions revealed Titan's complex and diverse atmosphere. The images of Voyager 2, taken in the visible, showed a clear asymmetry between the southern and northern hemispheres (Smith et al., 1982), and a detached layer of haze above 400 km altitude (Rages and Pollack, 1983).
- In 1997, Titan's atmosphere was furthermore investigated by the Infrared Space Observatory (ISO), finding evidence for water vapor in Titan's atmosphere (Coustenis et al., 1998) (see above).
- Since 2004, Titan has been extensively examined by the Cassini-Huygens mission (see e.g. Figure 2.2), consisting of the Cassini spacecraft that is in a bound orbit with Saturn and the Huygens probe. The Huygens probe was released from Cassini on December 26, 2004 entering Titan's atmosphere on January 14, 2005. Note that chapter 4 gives a general overview about the Cassini spacecraft, as well as on the instrument this work focuses on.

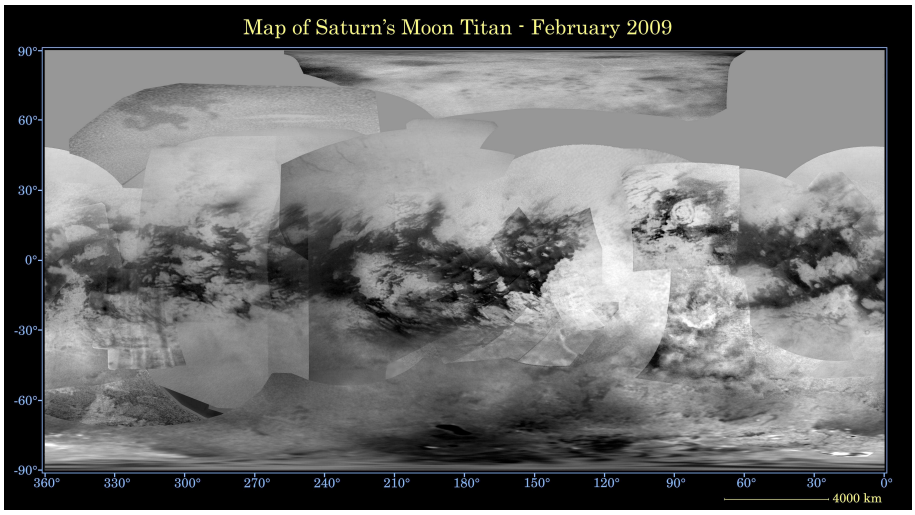

Fig. 2.2: Global digital map of Titan's surface taken in February 2009. This figure is composed of images taken by the Cassini spacecraft's Imaging Science Subsystem (ISS). The images were taken using a filter centered at 0.9 µm. Due to the scattering of light by Titan's dense atmosphere, no topographic shading is visible in these images. Image credits: NASA/JPL/Space Science Institute

Tab. 2.1: Orbital and atmospheric characteristics of Titan. Note that the inclination is given with respect to Saturn's equator. Unless otherwise specified, orbital parameters obtained from JPL HORIZONS solar system data and ephemeris computation service. Solar System Dynamics. NASA, Jet Propulsion Laboratory. `http://ssd.jpl.nasa.gov`

Semi-major axis	1,221,870 km
Eccentricity	0.0288
Orbital period	15.95 days
Inclination	0.34854°
Mean radius	(2,575.5±2) km [a)]
Mass	(1.3452±0.0002)·10^{23} kg [b)]
Mean density	1.8798±0.0044 g cm^{-3} [b)]
Equatorial surface gravity	1.352 m s^{-2}
Albedo	0.22
Surface pressure	1.467 bar [c,d)]
Surface temperature	93.7 K [c,d)]

[a)] Lindal et al. (1983), [b)] Jacobson et al. (2006), [c)] Fulchignoni et al. (2005), [d)] Harri et al. (2006)

2.2 Titan's surface and atmosphere

During its descent, the Descent Imager/Spectral Radiometer (DISR) aboard the Huygens probe revealed the presence of two major geological units (cf. Figure 2.3): (1) bright highlands north of the landing site which consist of hills incised with dark-colored, river-like valleys that are suggestive of erosion by methane rainfall and (2) a dark, flat terrain to the south that is similar to a lake bed (Soderblom et al., 2007; Keller et al., 2008). Huygens landed in the lake bed area but no liquid was detected. However, flow features were visible on km-scales (during descent) and possibly on meter-scales (after landing). Soderblom et al. (2007) proposed that the bright highlands consist of bright tholins covering dark material. According to this theory, the bright tholins in the valleys have been partially washed away by liquids. Keller et al. (2008) however suggested a different scenario, in which the highlands to the North constitute the bright component of Titan's crust, while the lake bed consists of dark, maybe sedimentary material. The land area is eroded by liquid flow, but the dark appearance of the river-like valleys is an illumination effect and consists of the same material as the land area around them. In their scenario

bright patches in the lake area are deposits of land material transported into the lake bed by the rivers.

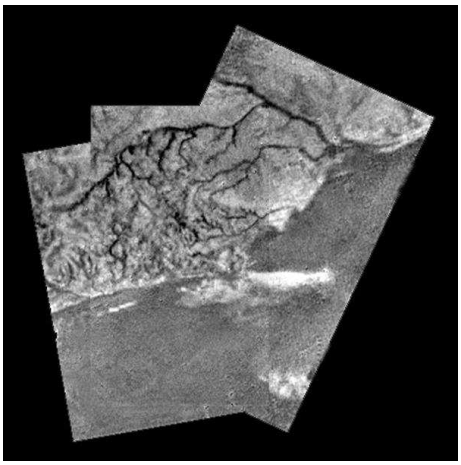

Fig. 2.3: Mosaic of three frames from the Huygens DISR instrument provides details of the high ridge area including the flow down into a major river channel from different sources. Image credits: ESA/NASA/JPL/University of Arizona

The Huygens Probe measured a ground temperature of 93.7 K (Fulchignoni et al., 2005) and a surface pressure of 1.467 bar (Fulchignoni et al., 2005; Harri et al., 2006). Titan's surface is significantly colder than its upper atmosphere due to an inverse greenhouse effect caused by the haze in Titan's atmosphere, reflecting sunlight back into space. Nevertheless, atmospheric methane also leads to a greenhouse effect on Titan's surface. Without it, Titan would be far colder. See Figure 2.4 for a temperature profile as measured by the Huygens Atmospheric Structure Instrument (HASI).

The Gas Chromatograph Mass Spectrometer (GCMS) aboard the Huygens probe measured a mole fraction of methane being almost constant (4.92%) between about 5 km altitude and the landing site (Niemann et al., 2005). In the troposphere, Doppler shifts of the radio signals from the Huygens probe gave direct in-situ determination of the vertical profile of zonal wind at about 10°S latitude between the surface and 140 km altitude (Bird et al., 2005; Folkner et al., 2006). At altitudes above 8 km, the measurements show that the winds are westerly (in the same direction as Titan's rotation) and increase with altitude. However, above 65 km there is a region of strong negative shear, and the winds decrease and nearly vanish at 75 km. At higher levels, they increase strongly with altitude, reaching about 60 $\mathrm{m\,s^{-1}}$ at 100 km altitude (Achterberg et al., 2008). According to results obtained from a general circulation model (GCM), tides and thermal gradients generate winds

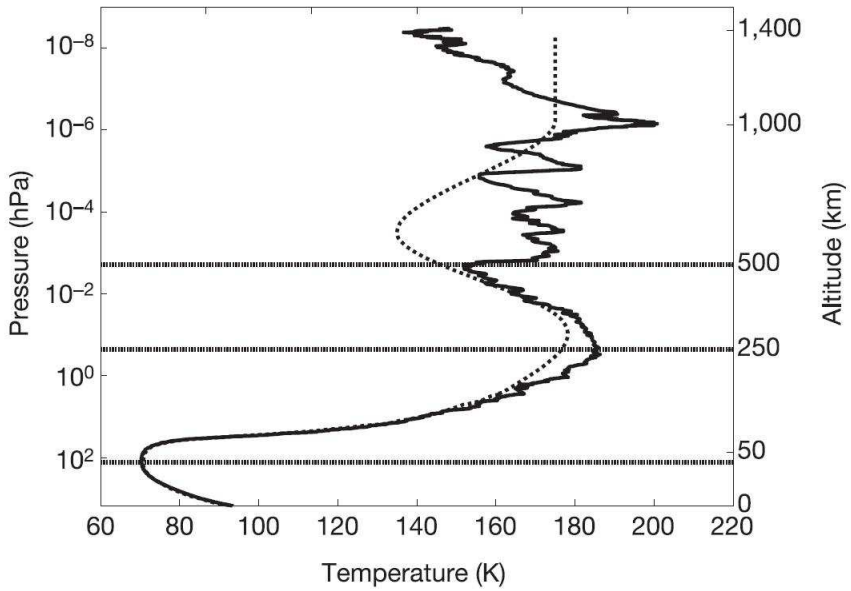

Fig. 2.4: The temperature profile as measured by the Huygens Atmospheric Structure Instrument (HASI) (solid line) is shown compared to the model of Yelle et al. (1997) (dashed line). Figure taken from Fulchignoni et al. (2005).

with a typical velocity 0.3 to 1 m s^{-1} near the surface (Tokano and Neubauer, 2002). Measurements by the Doppler Wind Experiment (DWE) aboard Huygens, as well by the Composite Infrared Spectrometer (CIRS) aboard Cassini have measured the zonal winds reaching about 100 m s^{-1} at altitudes between 200 and 300 km (0.1 to 1 mbar) indicating a strong atmospheric superrotation (Bird et al., 2005; Flasar et al., 2005; Achterberg et al., 2008).

Simulations of global wind patterns based on wind speed data taken by Huygens during its descent have suggested that Titan's atmosphere circulates in a single enormous Hadley cell: warm air rises in Titan's southern hemisphere - which was experiencing summer during Huygens' descent - and sinks in the northern hemisphere, resulting in high-altitude air flow from south to north and low-altitude airflow from north to south. The pole-to-pole wind circulation cell appears to be centered in the stratosphere; simulations by Crespin et al. (2008) suggest it ought to change every twelve years, with a three-year transition period, over the course of Titan's year (which is equal to Saturn's orbital period of 29.657 years).

Like Earth, Titan has a well-defined stratosphere with a tropopause at about 44 km (Fulchignoni et al., 2005) and a stratopause at about 225 km (Flasar

et al., 2005). Achterberg et al. (2008) found from CIRS observations, that the stratopause is nearly 20 K warmer in the northern polar region than at the equator and in the southern hemisphere. They also found that its altitude shifts from about 300 km near the equator to about 400 km poleward of 40°N. Stratospheric abundances have been inferred from measurements of CIRS as well as from the GCMS aboard the Huygens landing probe. In total, no significant longitudinal variations were found in the CIRS data, but sometimes strong meridional variations from the equator to the north pole were reported: C_4H_2, C_3H_4, C_6H_6, HCN and HC_3N showed a significant higher abundances towards the north pole (Coustenis et al., 2007).
The temperature difference between northern and southern hemisphere as well as the meridional variation of abundances are referred to as the "North-South asymmetry". It has been well known since Voyager 2 that Titan's atmosphere exhibits a hemispheric asymmetry depending on the season (Smith et al., 1982). The winter hemisphere which is richer in aerosols appears brighter in the infrared, and darker in the visible, than the summer hemisphere. The winter hemisphere is aerosol-enriched in the lower atmosphere, because the polar night facilitates the condensation of larger and more numerous aerosol particles (Yung, 1987; Rannou et al., 2002). Several mechanisms have been proposed to explain the asymmetry, but dynamics seem to be the most plausible explanation for this asymmetry (Hutzell et al., 1993).
The nominal distance of the Saturnian magnetopause at the subsolar point is approximately 24 Saturn radii. Compression or expansion of Saturn's magnetosphere results from variations in the solar wind; therefore Titan's orbit, at about 20 Saturn radii, can be either inside the magnetosphere of Saturn or outside. Since Titan has no significant intrinsic magnetic field, in the latter case the solar wind interacts with Titan's ionosphere and atmosphere directly (Nagy et al., 2001).

2.2.1 Clouds

Even prior to the discovery of clouds in Titan's atmosphere in the 1990s, these were evoked to explain the continuum observed in infrared spectra of the Infrared Radiometer, Interferometer and Spectrometer (IRIS) aboard Voyager 1 (Courtin, 1982; Samuelson, 1983). Clouds were also hypothesized as one possible interpretation of the scintillation of the Voyager 1 radio-occultation profile (Lindal et al., 1983). From spectra taken in 1993 and 1995, Griffith et al. (1998) observed dramatic changes in Titan's brightness at 1.6 and 2.0 μm, i.e. wavelengths probing down to the troposphere, which

featured a maximum variation of up to 200%. This effect could only be explained by the presence of reflective layers, or clouds, in Titan's atmosphere (Griffith et al., 1998). Since then clouds and other atmospheric phenomena have been reported on Titan by various investigators, e.g. a tenuous ethane cloud (Griffith et al., 2006) or the presence of a tropospheric cloud in the altitude range of 20 to 30 km (Lorenz et al., 2007).
Recently, Cassini images showed a fast evolution of clouds at the south pole and at midlatitudes (Porco et al., 2005; Griffith et al., 2005), in agreement with ground-based observations (Griffith et al., 2000; Bouchez and Brown, 2005). It was observed that convective clouds on Titan seem to have a lifetime of a few hours. If one can assign the observed features to the same cloud, they move at speeds of typically a few meters per second (Porco et al., 2005) which is comparable to cloud speeds on Earth.

2.2.2 Methane chemistry

The origin of methane in Titan's interior is still controversial. Hersant et al. (2008) argue that methane was trapped in the planetesimals formed in the solar nebula and embedded in the feeding zone of Saturn. These planetesimals formed Titan where methane is nowadays trapped within clathrate hydrates, concentrated at the top of a subsurface ocean of liquid water. Atreya et al. (2006) however suggest another formation mechanism such that high MgO-bearing ultramafic silicates might react with H_2O forming H_2, whose reaction with carbon dioxide produces methane in Titan's interior.
The first scenario implies that the D/H ratio in methane would be comparable to that in the planetesimals forming of Titan. The second scenario implies that D/H in Titan would be comparable to that in H_2O in the subsolar nebula. However, D/H in H_2O in Oort cloud comets is observed to be about twice as large as the value in CH_4 in Titan (Hersant et al., 2001). In order to fit Titan's value, isotopic exchange occurring in the solar nebula between H_2O and the protosolar H_2 needs to be considered.
Methane plays an important role in shielding the atmosphere from being gradually reduced to as low as tens of millibar pressure. Without the warming provided by the methane greenhouse and also by the subsequent formation of higher hydrocarbons, Titan's stratosphere and troposphere would become too cold for nitrogen to remain in the gas phase (Atreya et al., 2006). Condensation of large quantities during a fainter young sun period and higher surface albedos would leave behind only a fraction of the current amount of N_2 vapor in the atmosphere.
Methane is photolyzed at approximately 700 km and higher

(Wilson and Atreya, 2004). Throughout the lower stratosphere and upper troposphere a uniform abundance of $1.41 \pm 0.07\%$ was found from GCMS measurements (Niemann et al., 2005) which is in good agreement with CIRS measurements (Flasar et al., 2005). CH_4 can be used to determine the atmospheric temperature structure, using the strong vibrational-rotational ν_4 band of CH_4 near $7.7\,\mu$m and known opacities. Since methane is well mixed in the stratosphere, temperatures in the altitude range from about 130 to 410 km can be derived from limb and nadir measurements. Together with deuterated methane (CH_3D), methane can be used to infer the D/H ratio in Titan's atmosphere, hence yielding a D/H ratio in methane of $1.17^{+0.23}_{-0.28} \cdot 10^{-4}$ (Coustenis et al., 2007). See section 2.5 for a general discussion of the D/H ratio in the Solar System as well as on Titan.

Below 32 km and down to approximately 8 km a gradual increase of the CH_4 mole fraction was measured by GCMS during the descent of the Huygens probe. At 16 km a sudden increase in the gradient was recorded. Below 8 km, down to a level close to the surface it remained constant at $(4.92 \pm 0.25) \cdot 10^{-2}$ (Atreya et al., 2006). They concluded that methane condensation at 16 km resulted in a tenuous cloud or haze that extended to at least 8 km. As the CH_4 cloud persists, the rain-out of methane is expected. However, the amount of rain is expected to be relatively insignificant (Lorenz, 2000; Ingersoll et al., 2005).

The photolysis of methane leads to the production of the short-lived radicals CH_3, CH_2 and CH, which react very rapidly with atmospheric molecules including nitrogen and hydrogen. Stable, heavy and complex hydrocarbons and nitrile species which can condense and form hazes are subsequently produced. The self-reaction of CH_3 radicals forms ethane (C_2H_6) which is a common fate for methane itself, since ethane is very stable. Ethane eventually condenses and precipitates onto the surface. Cassini-Huygens measurements so far, however, do not show any oceanic reservoirs of ethane condensates on the surface as was proposed by Lunine et al. (1983) nor do they indicate significant condensation in the troposphere. Atreya et al. (2006) therefore suggested that the final products of methane photodissociation are ethane and hazes in comparable amounts, with the contribution from ethane condensation being far smaller than previously predicted. Hunten (2006) argues that ethane might condense onto smog particles instead of liquid droplets, forming kilometer-thick deposits on the surface.

Yung et al. (1984); Lara et al. (1996); Lebonnois et al. (2001) and Wilson and Atreya (2004) found the photochemical lifetime of CH_4 to be

in the range of about 10 to 100 million years, which is small compared to Titan's age. The hydrogen-poor interior of Titan prevents considerable recycling of the hydrocarbon products from the methane chemistry back into methane. Hence, a strong methane source is needed to replenish methane in the atmosphere. Tobie et al. (2006) suggested that it could have been episodically outgassed from Titan's interior. Three major episodes of outgassing have been suggested, occurring during, (1) the internal differentiation (silicate core formation); (2) the onset of the convection in the silicate core; and (3) during the late subsequent cooling and crystallization of the outer layer.

2.2.3 Hydrogen budget

Atomic hydrogen is mainly produced by the photolytic destruction of methane in the homosphere (with the homopause altitude being at about 1,240 km, de La Haye et al. 2007b) at altitudes of approximately 700 km and above, (Lebonnois et al., 2003; Wilson and Atreya, 2004) subsequently transported downward to the mesosphere by diffusion, where H-removal proceeds quickly. One of the main pathways for producing H and H_2 is the dissociation of CH_4 by the following reactions (Mordaunt et al., 1993):

- $CH_4 + h\nu \rightarrow CH_3 + H$.
- $CH_4 + h\nu \rightarrow {}^1CH_2 + H_2$.
- $CH_4 + h\nu \rightarrow CH + H + H_2$.

Similar reactions involving the photo-dissociation of higher hydrocarbons and nitriles such as C_2H_6, C_2H_4, C_2H_2, C_3H_8, C_4H_2 and HCN also leads to production of atomic and molecular hydrogen. The production of hydrogen due to photodissociation, however, is limited to altitudes corresponding to high UV influx.
In the altitude range of 300 to 500 km (in the mesosphere), the conversion of H to H_2 occurs via the reaction $H + CH_2 \rightarrow H_2 + CH$. At lower altitudes of about 100 to 300 km (mid to upper stratosphere) atomic hydrogen is produced mainly via the photodissociation of acetylene (C_2H_2) and diacetylene (C_4H_2). For acetylene (C_2H_2), the photodissociation rate remains significant down to the tropopause producing substantial amounts of H in this region. This is due to the combined effect of major amounts of C_2H_2 and a large dissociation cross section of C_2H_2 at wavelengths below 0.2 μm. The destruction is independent of the UV screening by other hydrocarbons, because only C_2H_2 has a significant absorption cross section between 0.16 μm and 0.2 μm, e.g.

the photodissociation of CH_4 is limited to wavelengths shorter than 0.16 μm. In the mid to upper stratosphere, H is in steady state: production occurs due to dissociation of acetylene and destruction through the reaction given above.

2.2.4 Haze production and the role of atomic hydrogen

Atomic hydrogen is plays a key role in the producing organic haze layers in Titan's atmosphere, which have been revealed by the Voyager and Cassini spacecrafts (Smith et al., 1981; Porco et al., 2005). Haze is considered to be produced by polymerization of unsaturated gas species and consists of polycyclic aromatic compounds (i.e. containing benzene rings or similar rings of atoms), aliphatic polymers (i.e. which do not contain rings) and nitriles. Under the temperature and pressure conditions of Titan's stratosphere, these hydrocarbons and nitriles can condense and precipitate.
Polymers of polyacetylenes, polyynes (e.g. diacetylene C_4H_2) and nitriles form hazes in the upper atmosphere (>500 km), whereas polycyclic aromatic hydrocarbon (PAH) polymers condense to form hazes in the middle and lower stratosphere (<200 km) (Atreya et al., 2006; Wilson and Atreya, 2003). Some hydrocarbons survive as hazes suspended in the atmosphere until they approach the tropopause cold trap where the majority condense. At large concentrations of atomic hydrogen, however, the unsaturated gas species in Titan's atmosphere react to form saturated gas species, and the production efficiency of organic haze would be reduced.

2.3 Atmospheric escape

2.3.1 Escape mechanisms

There are several different processes that can lead to the escape of a planetary atmosphere. In some cases escape can be a very important process for the development of a planet. For example, Mars has probably lost much of their water due to atmospheric escape since Mars has a low gravity.

Thermal escape

The Jeans escape is a thermal escape mechanism of particles from the upper atmosphere, where the mean free path is comparable to the scale height. This atmospheric layer is usually called the exosphere with the exobase being the layer, where the mean free path equals the scale height (see also section 2.4). Below the exobase, the particle velocities obey the Maxwell-Boltzmann

distribution of velocities v

$$f(v) = 4\pi \left(\frac{m}{2\pi k_B T}\right)^{3/2} v^2 \exp\left(-\frac{mv^2}{2k_B T}\right), \tag{2.1}$$

with m being the mass of the particle, k_B the Boltzmann constant and T the temperature. The temperature of any physical system is the result of the motions of the molecules and atoms, which make up the system. These particles have a range of different velocities, and the velocity of any single particle constantly changes due to collisions with other particles. However, the fraction of a large number of particles within a particular velocity range is nearly constant if the system is at or near equilibrium. The Maxwell-Boltzmann distribution of velocities specifies this fraction, for any velocity range, as a function of the temperature of the system.
Although equation 2.1 gives the distribution of speeds or in other words the fraction of particles having a particular speed, one is often more interested in quantities such as the average speed of the particles rather than the actual distribution. Different averages can be defined:

- The most probable speed, v_p, is the speed most likely to be possessed by any particle in the system and corresponds to the maximum value of $f(v)$. In case of equation 2.1 it is given by

$$v_p = \sqrt{\frac{2k_B T}{m}} \tag{2.2}$$

- The mean speed $\bar{v}$ is the mathematical average of the speed distribution $f(v)$:

$$\bar{v} = \sqrt{\frac{8k_B T}{\pi m}} = \frac{2}{\sqrt{\pi}} v_p \tag{2.3}$$

- The root mean square speed, v_{rms} is the square root of the average squared speed $\bar{v^2}$:

$$v_{\mathrm{rms}} = \sqrt{\bar{v^2}} = \sqrt{\frac{3k_B T}{m}} = \sqrt{\frac{3}{2}} v_p \tag{2.4}$$

The escape efficiency depends on the escape parameter $\lambda(r)$, which is the ratio of gravitational potential energy to kinetic energy at the critical level (the exobase):

$$\lambda_j(r) = \frac{GMm_j/r}{1/2mv_p^2} = \frac{2}{\eta}\frac{GMm_j}{rk_B T_c} = \frac{v_{\mathrm{esc}}}{v_p}, \tag{2.5}$$

with G being the gravitational constant, M the mass of the body (here: Titan), m_j the mass of the escaping particle of species j, r the distance to the

center of the body, k_B the Boltzmann constant, η the degrees of freedom and T_c the temperature at the critical level (the exobase), v_{esc} the escape velocity and v_p the most probable Maxwellian velocity (Chamberlain, 1963). At the exobase the critical escape parameter is then $\lambda_j(r_c) =: \lambda_{j,c}$. The Jeans escape hence describes the escape of individual particles from the high velocity tail of the Maxwell-Boltzmann distribution of velocities from the exobase.

The Jeans escape rate can then be obtained by integrating the Maxwell-Boltzmann distribution of velocities over the radial flux of particles, giving

$$\Phi_J = \frac{1}{2\sqrt{\pi}} n_c v_p (1+\lambda)\exp(-\lambda). \tag{2.6}$$

When the escape parameter λ_j is lower than the critical value $\lambda_{j,c}$, hydrodynamic escape occurs. Hydrodynamic escape is an important process in the formation and evolution of planetary atmospheres (Bauer, 1992). An extremely rapid flow of atomic hydrogen from a primitive atmosphere will carry away heavy gases in what is known as "atmospheric blow-off".

Non-thermal escape mechanisms

Besides thermal escape, which represents a lower boundary for atmospheric escape processes, there exist also non-thermal escape mechanisms, which in general involve ions or electrons (Chamberlain and Hunten, 1987) achieved via:

- Excess energy during dissociation and recombination of molecules.
- Ion-neutral reactions, in which chemical energy is converted into kinetic energy.
- Impact dissociation, where the energy comes from an incident electron or photon.
- Charge exchange with fast H^+ ions from the magnetosphere, where any excess energy is largely retained.
- Sputtering, where a fast atom or ion collides with another atom.
- Ion escape: H^+ ions can be accelerated out through open magnetic field lines in the polar regions.
- Pick-up from solar winds, which is the dominant process in the atmosphere of Mars.
- Electric fields, which accelerate ions.

2.3.2 Escape from Titan's atmosphere

Due to their small mass, atomic and molecular hydrogen are strongly affected by vertical diffusion processes within Titan's atmosphere. Turbulent mixing transports atomic hydrogen from the regions of production towards the surface and towards the exosphere, while buoyancy provided by the atmosphere allows hydrogen to rise and finally escape to space, only weakly opposed by Titan's small gravity. Atomic hydrogen has a large scale height in the exosphere and shows a significant atmospheric loss via Jeans escape. Cui et al. (2008) found a molecular hydrogen escape flux from INMS measurements, which is about three times higher than the Jeans escape flux for H_2 from Titan. Molecular hydrogen was long thought to escape from Titan mainly due to dissociative recombination (e.g. Chamberlain and Hunten 1987). However, Cui et al. (2008) found that non-thermal escape mechanisms are not required to interpret the loss of H_2 from Titan. The enhanced escape rate (relative to the Jeans value) was found using an orthogonal series expansion in a 13-moment approximation defining a non-Maxwellian velocity distribution function that includes the effects of both thermal conduction and viscosity. The effect of collisions between H_2 and N_2 below 1,600 km was found to be significant. The 13-moment model interprets the enhanced escape as a result of the accumulation of H_2 molecules on the high-energy portion of the velocity distribution function, primarily associated with the conductive heat flux.

The critical value of the escape parameter for atomic hydrogen is $\lambda_{c,H} = 1.5$; below this value hydrodynamic escape occurs. An escape parameter $\lambda_{c,H} > 10$ for atomic hydrogen results in negligibly small escape rates; values of $\lambda_{c,H}$ =4–8 indicate that a few percent of the atoms reach the escape velocity. With an exobase temperature of $T_c = 153\,\mathrm{K}$ (averaged value from INMS measurements de La Haye et al. 2007b) and an exobase radius of 4,000 km (as measured from Titan's center), one obtains for atomic hydrogen $\lambda_{c,H} = 1.77$, which is slightly above the limit at which hydrodynamic escape occurs. The critical temperature is reached at 181 K.
With an escape parameter of $\lambda_{c,H} = 1.77$ one obtains a Jeans escape flux of $\Phi_J = 1.67 \cdot 10^9 \mathrm{cm}^{-2}\mathrm{s}^{-1}$ with an atomic hydrogen density of $n_c = 8 \cdot 10^4\,\mathrm{cm}^{-3}$ at the exobase, as inferred from de La Haye et al. (2007b). Integrated over the whole Titan sphere this yields an escape flux of $Q_H = 3.49 \cdot 10^{27}\,\mathrm{s}^{-1}$ at the exobase. The Jeans escape velocity $v_J = \Phi_J / n_c$ for atomic hydrogen is then $v_{J,H} = 0.21\,\mathrm{km\ s}^{-1}$.

The photo-ionization lifetime of atomic hydrogen at Saturn's distance is about $(1-2)\cdot 10^9$ s (Smyth, 1981). The charge-exchange of hydrogen atoms with either the solar wind or planetary-magnetospheric protons is however dominating: When the magnetopause of Saturn is compressed within the orbit of Titan, the hydrogen lifetime along the unprotected orbit will be determined by the solar wind plasma, giving a lifetime of about $(3.3-5.0)\cdot 10^7$ s (Wolfe et al., 1980). If, however, the orbit of Titan lies within the magnetosphere, the hydrogen lifetime is determined by the co-rotating plasma giving a lifetime of about $(4.4-7.1)\cdot 10^7$ s (Smyth, 1981). The characteristic timescale for a hydrogen atom thermally emitted from Titan's exosphere is however much shorter: Using a Monte Carlo model which simulates the trajectories of particles released from the exobase, one finds a characteristic timescale of $2\cdot 10^4$ s for hydrogen atoms until they reach an altitude of 30,000 km above the exobase (see chapter 5.4). Thus, for atomic hydrogen thermal escape is the dominant escape mechanism acting in Titan's atmosphere.

Titan is under usual solar wind conditions half of its orbital period in Saturn's magnetosphere. Due to the lack of an own significant intrinsic magnetic field, Lammer et al. (1998) found that sputtering by magnetospheric ions (protons and N^+ ions) becomes important during this time, heating the thermosphere by an amount of about 30 K . They conclude that Titan's exospheric temperature may then reach or even exceed the critical temperature, at which hydrodynamic escape becomes important. However, Michael and Johnson (2005) also investigated the energy deposition of pickup ions and found, contrary to Lammer et al. (1998), a much lower increase in the exospheric temperature of only about 4 to 7 K caused by energy deposition of N^+.

2.4 Titan's exosphere

The main focus of this work is the investigation of Titan's exosphere. The exosphere represents the transition region from the gravitationally bound atmosphere to free interplantary space. Within the exosphere, the mean free path of an atmospheric particle is greater than the scale height of the atmosphere, hence collisions between particles become negligible. In reality, the transition between the atmosphere and the exosphere however spreads over a wide altitude region.

The exobase of Titan, where the mean free path equals the atmospheric scale height, is positioned at around 1,500 km: de La Haye et al. (2007b) have determined the exobase altitude of Titan during three flybys of Cassini (T_A,

T_B, T_5) to be at 1,442±7 km (T_A flyby in October 2004 near dusk terminator), 1,409±14 km (T_B flyby in October 2004 near dusk terminator) and 1,401±7 km (T_5 flyby in April 2005 on the night side). The main neutral components of the exosphere are N_2, CH_4 and H_2 (Toublanc et al., 1995; Cui et al., 2009), which has been confirmed recently by the Cassini Ion Neutral Mass Spectrometer (INMS) measurements, as reviewed below. See table 2.2 at the end of this section for a summary of exospheric parameters.

2.4.1 Exospheric temperatures

Exospheric temperatures have been inferred most recently from several observations by Cassini. Note that the term "temperature" is only valid at the exobase, where particle velocities obey the Maxwell-Boltzmann distribution. Above the exobase this assumption can no longer be maintained. Nevertheless one can assume to a first order approximation that within a certain altitude range above the exobase the velocity distribution is close to the Maxwellian, hence a temperature can be defined. In most exospheric models the exospheric temperature is assumed to be constant within a so-called exobase layer of a certain thickness given by the mean free path at the exobase.

The major energy sources for Titan's upper atmosphere are solar radiation and Saturn's magnetospheric ions and electrons. Solar UV and EUV radiation is absorbed in Titan's upper atmosphere with the most important contribution to the heating coming via absorption of Lyman-α radiation by methane (Lellouch et al., 1990). This occurs at an altitude of about 700–800 km where a large fraction of the heat can be removed from the atmosphere by infrared cooling (Lellouch et al., 1990). However, the exospheric temperature is primarily a function of the N_2 heating at EUV wavelengths (150 – 350 Å), whereas plasma heating is less important (Michael and Johnson, 2005).

Lellouch et al. (1990) showed that solar heating of molecular nitrogen is more important than CH_4 and C_2H_2 in the exosphere of Titan by up to about a factor of four.

The estimated exobase temperature during both Voyager encounters was initially thought to be about 180 K (Smith et al., 1982; Lindal et al., 1983). However, Vervack et al. (2004) reanalyzed the Voyager 1 data and found that the exospheric temperature of Titan is about 20 to 40 K less than those estimates, consistent with recent Cassini observations. Temperature close to the exobase have been obtained by the INMS instrument (de La Haye

et al., 2007b) as a result of a multi-parameter fit of a diffusion model, which was simultaneously performed on the N_2 and CH_4 density data recorded between closest approach (T_A: 1,174.0 km, T_B: 1,197.6 km, T_5: 1,025.2 km) and 1,500 km during these three flybys. The best fitting temperatures below 1,500 km have been determined to be 152.8 ± 4.6 K (T_A), 149.0 ± 9.2 K (T_B) and 157.4 ± 4.9 K (T_5), assuming a negligibly small methane escape flux. The error bars represent the horizontal variation traveled by the spacecraft during the flybys. The T_B error bars are assumed to be twice those of T_A, since only the egress data is available (see also table 2.2).
Above 1,500 km however, depending on the molecule fitted, exospheric temperatures in the range of 149 to 205 K have been found to fit the N_2 data, whereas for CH_4 temperatures in the range of 149 to 223 K are necessary to fit the T_A, T_B, and T_5 data.

2.4.2 Exospheric densities

Simultaneous to the fitting of exospheric temperatures, as described above, de La Haye et al. (2007b) have also determined the neutral densities of Titan's main exospheric constituents from INMS measurements during the flybys: the molecular nitrogen density at 1,400 km was found to be $(4.85 \pm 0.21) \cdot 10^7$ cm^{-3} during the T_A flyby , $(3.42 \pm 0.42) \cdot 10^7$ cm^{-3} during the T_B flyby and $(2.83 \pm 0.13) \cdot 10^7$ cm^{-3} during the T_5 flyby . The methane densities determined were: $(3.82 \pm 0.37) \cdot 10^6$ cm^{-3} (T_A), $(2.77 \pm 0.74) \cdot 10^6$ cm^{-3} (T_B) and $(3.16 \pm 0.46) \cdot 10^6$ cm^{-3} (T_5). Cui et al. (2008) found an H_2 density of $(4.34 \pm 0.02) \cdot 10^5$ cm^{-3} - see also table 2.2.
The density of atomic hydrogen could not be measured directly by the INMS instrument. This is because the INMS chamber walls have a certain probability to adsorb molecules entering the instrument orifice, which may further undergo complicated wall chemistry processes before being released with a time delay (Vuitton et al., 2008). Atomic hydrogen is very reactive, hence counts in this channel are not reliable (J. Cui, priv. com.).
Nevertheless, the distribution can be calculated by photochemical models or determined indirectly from measurements of the Lyman-α emission. Therefore up to now only very few values for the atomic hydrogen exobase density have been published, most of them are results from photochemical models. The values published range from $4.2 \cdot 10^3\,cm^{-3}$ up to $8 \cdot 10^4\,cm^{-3}$:

- Lyman-α observations of Voyager by Broadfoot et al. (1981) indicated an exobase atomic hydrogen density of $4 \cdot 10^4$ cm^{-3}.
- Yung et al. (1984) calculate a value of $4.2 \cdot 10^3$ cm^{-3} at the exobase

from their photochemical model.

- Toublanc et al. (1995) use an updated photochemical model and infer an exobase H density of $8 \cdot 10^3$ cm^{-3}.

- Garnier et al. (2007) in turn use an updated version of the Toublanc 1995 model to obtain a density of $4.6 \cdot 10^4$ cm^{-3}.

- de La Haye et al. (2007a) have inferred the exobase density from modeling fast neutrals in the exosphere with a hot to thermal neutral ratio of $5 \cdot 10^{-5}$ for atomic hydrogen. A hot H exobase density of 4 cm^{-3} is given, from which a hydrogen density of $8 \cdot 10^4$ cm^{-3} can be derived, which is higher than the densities published before. The hot H exobase density has been derived from photochemical modeling, whereas the hot-to-thermal neutral ratio has been inferred using a method based on the Liouville theorem, as described in de La Haye et al. (2007b).

- Most recently, Krasnopolsky (2009) found an exobase density of about $7 \cdot 10^4$ cm^{-3} (obtained from their Fig. 10) from photochemical modeling.

Up to now, there are no measurements of the distribution of atomic hydrogen within the exosphere of Titan. Most authors choose the model of Chamberlain (1963) to represent this. Using Liouville's equation (which is equivalent to Boltzmann's equation without collisions) the density distribution can be calculated throughout the exosphere, since Liouville's theorem states that the density in phase space remains constant along a dynamical trajectory. In order to calculate the density distribution, partition functions of different particle trajectories are considered. The Chamberlain model has been applied to the Earth's exosphere, yielding densities comparable to satellite measurements (Rairden et al., 1986).

Tab. 2.2: Parameters of Titan's exosphere.
Note that exospheric temperatures above 1,500 km are given depending on the molecule that was fitted by the authors. The temperature range takes into account all three flybys considered by the authors (see text for details).

Quantity	Value
Exobase altitude	1,442±7 km (T_A) [a)] 1,409±14 km (T_B) [a)] 1,401±7 km (T_5) [a)]
Temperature below 1,500 km	152.8 ± 4.6 K (T_A) [a)] 149.0 ± 9.2 K (T_B) [a)] 157.4 ± 4.9 K (T_5) [a)]
Temperature above 1,500 km	149–205 K (N_2) [a)] 149–223 K (CH_4) [a)]
N_2 density [$\cdot 10^7$]	(4.85 ± 0.21) cm^{-3} (T_A) [a)] (3.42 ± 0.42) cm^{-3} (T_B) [a)] (2.83 ± 0.13) cm^{-3} (T_5) [a)]
CH_4 density [$\cdot 10^6$]	(3.82 ± 0.37) cm^{-3} (T_A) [a)] (2.77 ± 0.74) cm^{-3} (T_B) [a)] (3.16 ± 0.46) cm^{-3} (T_5) [a)]
H_2 density [$\cdot 10^5$]	(4.34 ± 0.02) cm^{-3} [b)]
H density [$\cdot 10^4$]	0.42 cm^{-3} [c)] 0.8 cm^{-3} [d)] 4 cm^{-3} [e)] 4.6 cm^{-3} [f)] 7 cm^{-3} [g)] 8 cm^{-3} [h)]

[a)]de La Haye et al. (2007b), [b)]Cui et al. (2008), [c)]Yung et al. (1984), [d)]Toublanc et al. (1995), [e)]Broadfoot et al. (1981), [f)]Garnier et al. (2007), [g)]Krasnopolsky (2009), [h)]de La Haye et al. (2007a)

2.5 D/H ratio

2.5.1 Overview

Isotopic abundance ratios in the bodies of the Solar System yield information on fractionation effects that occurred in space and time. Enrichment or depletion in isotopic compositions are caused by chemical and physical processes involved in the formation and evolution of the Solar System. Knowing the distribution of isotopic ratios allows one to trace the history of the Solar System.

The D/H ratio provides important information for the determination of the origin and evolution of any body surrounded by an atmosphere in the Solar System. Its value gives direct information about the atmospheric evolution. When forming the atmosphere, the ratio is assumed to be the same throughout the entire Solar System. Due to atmospheric escape processes, the lighter hydrogen atoms could escape the atmosphere, while enrichment with the heavier deuterium atoms took place.

There are basically two ways to determine the D/H ratio: In situ measurements can be accomplished by mass spectroscopy. Another approach is to spectroscopically observe the ratio of hydrogen and deuterium bearing molecules, like H_2/HD, CH_4/CH_3D,H_2O/HDO, and so forth. The problem here is, that molecular ratios differ from species to species, hence the measurement of the atomic ratio is more desirable.

Deuterium is a relic of the primordial nucleosynthesis that occurred shortly after the Big Bang. It is generally believed that since the Big Bang, deuterium has been only destroyed and not created in nuclear reactions occurring inside stars. Deuterium is destroyed in stars in the second step of the proton-proton chain (${}^2_1\mathrm{H}+{}^1_1\mathrm{H} \rightarrow {}^3_2\mathrm{He} + \gamma$). This process, called "astration", depletes the universe of deuterium as it cycles its way through star formation, astration, and interstellar injection. The current value of the D/H ratio of the Interstellar Medium (ISM) was determined to be $1.5{\cdot}10^{-5}$ (Moos et al., 2002).

Measurements of the D/H ratio in the Solar System reveal two distinct reservoirs of deuterium (see Table 2.3 and Figure 2.5). The first reservoir is deuterium enriched relative to the second one and includes the Earth, Mars, Uranus, Neptune, Titan, and cometary material. The second reservoir consists of Jupiter, Saturn, and the Sun.

The general explanation for the differences in D/H between these two reservoirs lies in their formation history. A general review can be found in Horner et al. (2008). The protosolar nebula mainly consisted of hydrogen gas (D/H of $2.5 \cdot 10^{-5}$ Robert et al. 2000), helium and less abundant organic particle

clusters (grains) with a higher D/H ratio of $\sim 2 \cdot 10^{-4}$ (Geiss and Reeves, 1981). The deuterium enrichment of the grains occurs due to ion-molecule reactions powered by UV radiation from nearby stars (see e.g. Brown and Millar 1989). Thus, two distinct deuterium reservoirs existed already in the protosolar nebula.

During the formation of the Solar System, the protosolar nebula formed the Sun. In the outer cooler parts of the protoplanetary disc dust grains grew by mutual collisions, forming the cores of the planets and other solid bodies. After the "protosun" had reached the hydrogen burning stage, a period of strong solar winds cleared the inner nebula from light gases out to the so-called "snow line" at about 4 AU. The planetesimals outgassed deuterium (generally in the form of deuterated methane) in a process that preserved the deuterium enrichment in the atmospheres (Owen, 1994), inheriting the enriched D/H ratio of grains.

Further out beyond the snow line, the heavy cores of Jupiter and Saturn captured gas from the solar nebula and adopted the corresponding D/H ratio: Because Jupiter and Saturn have a low ratio of core mass to total mass of around 0.03 to 0.06 for Jupiter and 0.11 to 0.22 for Saturn (Owen, 1994), they are believed to be primarily built from the main reservoir of gas in the protosolar nebula. Hence they show depleted D/H ratios of about $2 \cdot 10^{-5}$.

Uranus, Neptune, and Pluto took much longer to accrete in the lower density regions of the protoplanetary disk. By this time the solar nebula had been nearly swept away far into to outer regions of the Solar System. Thus, these planets show D/H rations inbetween the enriched and protosolar value.

Tab. 2.3: Overview of Solar System D/H ratios

Object	D/H ratio	Reference
Local Interstellar Medium	$1.52^{+0.18}_{-0.18} \cdot 10^{-5}$	Moos et al. (2002)
Protosolar nebula / Sun	$2.5^{+0.5}_{-0.5} \cdot 10^{-5}$	Robert et al. (2000)
Venus	$1.7^{+0.3}_{-0.3} \cdot 10^{-2}$	de Bergh et al. (1991)
Earth	$1.41^{+0.3}_{-0.3} \cdot 10^{-4}$	Lécuyer et al. (1998)
Mars	$9^{+4}_{-4} \cdot 10^{-4}$	Owen et al. (1988)
Jupiter	$2.25^{+0.35}_{-0.35} \cdot 10^{-5}$	Lellouch et al. (2001)
Saturn	$1.7^{+0.75}_{-0.45} \cdot 10^{-5}$	Lellouch et al. (2001)
Uranus	$5.5^{+3.5}_{-1.5} \cdot 10^{-5}$	Feuchtgruber et al. (1999)
Neptune	$6.5^{+2.5}_{-1.5} \cdot 10^{-5}$	Feuchtgruber et al. (1999)
Titan	$1.63^{+0.27}_{-0.27} \cdot 10^{-4}$	Coustenis et al. (2008)
Hyakutake	$3.0 \cdot 10^{-4}$	Bertaux et al. (1998)
Halley	$3.16^{+0.34}_{-0.34} \cdot 10^{-4}$	Eberhardt et al. (1995)
Hale Bopp	$3.0^{+0.04}_{-0.04} \cdot 10^{-4}$	Meier et al. (1997)

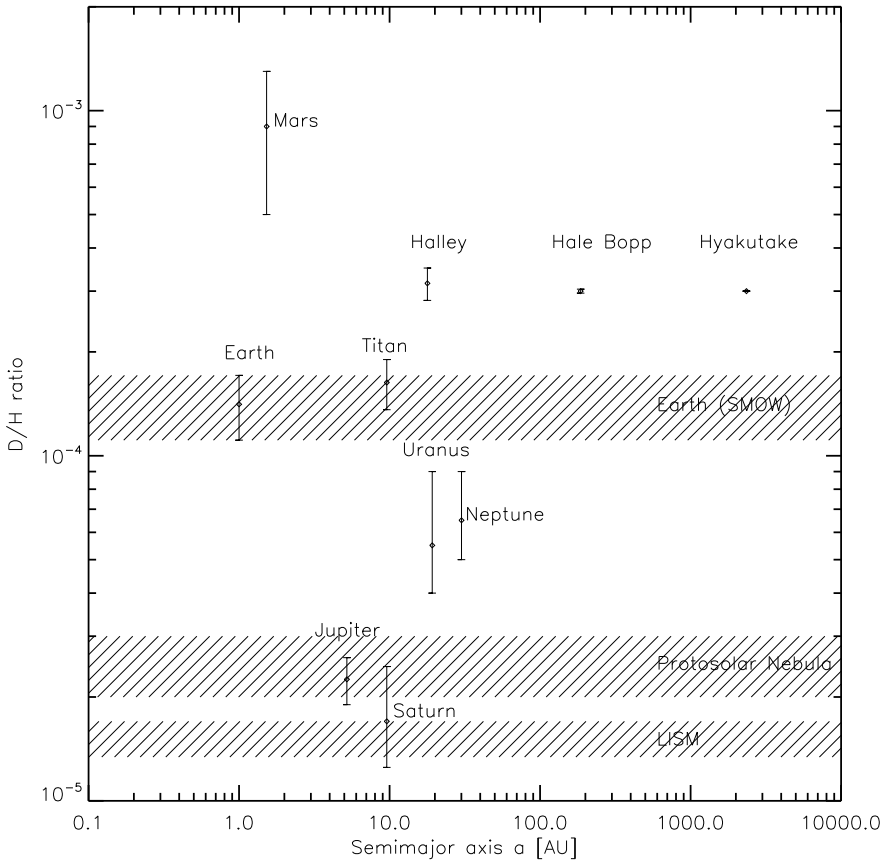

Fig. 2.5: D/H ratios for different objects in the Solar System

2.5.2 D/H ratio on Titan

Most of the measurements performed on Titan provided the ratio of CH_3D to CH_4 (see table 2.4). First measurements were performed using Voyager IRIS data and later data from the ISO satellite. Both Voyager and ISO values as well as data from ground-based observations are compatible within their error bars. Later, during the Cassini mission, the GCMS mass spectrometer measured a higher value of $2.3^{+0.5}_{-0.5} \cdot 10^{-4}$ (Niemann et al., 2005). Bézard et al. (2007) obtained a D/H ratio of $1.32^{+0.15}_{-0.11} \cdot 10^{-4}$ from the CH_3D band and taking additionally into account the $^{13}CH_3D$ isotope using CIRS infrared spectra. Most recently, Coustenis et al. (2008) suggested a D/H ratio of $(2.09 \pm 0.45) \cdot 10^{-4}$ from nadir observations of C_2HD using CIRS. In limb geometry they found a ratio of $(1.63 \pm 0.27) \cdot 10^{-4}$.

In total one observes a higher D/H ratio in acetylene (C_2HD/C_2H_2) and molecular hydrogen (DH/H_2) with respect to D/H in methane (CH_3D/CH_4). The photodissociation products of methane in the upper atmosphere are H_2 (HD) and C_2H_2 (C_2HD). Subsequent photolysis may then enrich molecular hydrogen and acetylene with deuterium, compared to methane. This is because, when either CH_3D or C_2HD is photolyzed, there is a preference for H atoms being removed over D atoms due to their mass difference. Therefore a higher D/H ratio is expected for C_2HD and HD than for the parent molecule CH_3D (Coustenis et al., 2007, 2008). Coustenis et al. (2007) argue that the enhancement in the GCMS measurement of Niemann et al. (2005) can also be due to the fragmentation of methane into H_2 and other components within the GCMS by electron impact ionization. This would produce a source additional to the atmospheric hydrogen produced by the photolysis of methane.

All measurements of the D/H ratio in methane indicate substantially higher values than the protosolar value, but less than the value for water in the Earth's ocean. There is no general agreement as to the cause of the enhancement (see for instance Lunine and Tittemore 1993). Mousis et al. (2002) argue that methane was trapped in icy grains at low temperatures in the solar nebula and incorporated into the planetesimals which finally formed Titan. In other words, the D/H ratio in methane is representative of the value acquired in the solar nebula in the formation region of Saturn. Deuterium in methane would have then isotopically exchanged with molecular hydrogen in the gas phase at the time entrapped in solids condensed in Saturn's formation zone (Mousis et al., 2002).

On the other hand, Titan could have been accreted based on solids condensed in an initially hot and dense Saturnian subnebula. In this picture, the methane incorporated in Titan would result from CO and CO_2 gas-phase conversions and would represent an almost solar D/H ratio at the time of its trapping in solids ultimately accreted by the satellite. Pinto et al. (1986) and Lunine et al. (1999) argued that the observed D/H enhancement could be the result of photochemical enrichment of deuterium. The D/H ratio acquired by the atmospheric methane of Titan would be progressively enriched with time via photolysis, until it reaches the value observed today.

Tab. 2.4: Overview of Titan D/H ratios

Value	Method	Instrument	Reference
$1.5^{+1.4}_{-0.5} \cdot 10^{-4}$	CH_3D/CH_4	IRIS	Coustenis et al. (1989)
$0.78^{+0.23}_{-0.23} \cdot 10^{-4}$	CH_3D/CH_4	Ground based	Orton (1992)
$0.87^{+0.32}_{-0.19} \cdot 10^{-4}$	CH_3D/CH_4	ISO	Coustenis et al. (2003)
$1.25^{+0.25}_{-0.25} \cdot 10^{-4}$	CH_3D/CH_4	Ground based	Penteado et al. (2005)
$2.3^{+0.5}_{-0.5} \cdot 10^{-4}$	HD/H_2	GCMS	Niemann et al. (2005)
$1.17^{+0.23}_{-0.28} \cdot 10^{-4}$	CH_3D/CH_4	CIRS	Coustenis et al. (2007)
$1.32^{+0.15}_{-0.11} \cdot 10^{-4}$	CH_3D/CH_4	CIRS	Bézard et al. (2007)
$2.09^{+0.45}_{-0.45} \cdot 10^{-4}$	C_2HD/C_2H_2	CIRS (nadir obs.)	Coustenis et al. (2008)
$1.63^{+0.27}_{-0.27} \cdot 10^{-4}$	C_2HD/C_2H_2	CIRS (limb obs.)	Coustenis et al. (2008)

3. RADIATIVE TRANSFER

In general, radiative transfer is the physical phenomenon of energy transfer in the form of electromagnetic radiation. The propagation of radiation through a medium is affected by absorption, emission, and scattering processes. The equation of radiative transfer describes these interactions mathematically. Equations of radiative transfer have application in a wide variety of subjects including optics, astrophysics, atmospheric science, and remote sensing. Analytical solutions to the radiative transfer equation exist for simple cases but for more realistic problems with complex multiple scattering effects numerical methods are absolutely required.

3.1 Basic definitions

A detailed introduction into the basic quantities in the theory of radiative transfer can be found in e.g. Chandrasekhar (1960) and Mihalas (1978). The basic definitions of these works are reviewed here.

- The spectral photon density $n_{\mathrm{ph},\nu}(t, \mathbf{x}, \hat{\mathbf{k}})\, \mathrm{d}V\, \mathrm{d}^2\hat{k}\, \mathrm{d}\nu$ represents the number of photons within a small space volume element $\mathrm{d}V$ around the position vector $\mathbf{x}$ at time t with energy

$$E_{\mathrm{ph}} = h\nu \tag{3.1}$$

  and momentum

$$\mathbf{p}_{\mathrm{ph}} = \frac{h\nu}{c}\hat{\mathbf{k}} \tag{3.2}$$

  having a frequency in the range $(\nu, \nu + \mathrm{d}\nu)$ and a directional unit vector $\hat{\mathbf{k}}$ pointing into the solid angle $\mathrm{d}^2\hat{k}$ around $\hat{\mathbf{k}}$.

  The vector $\hat{\mathbf{k}}$ also denotes the direction of the selected photon velocity $\mathbf{c} = c\hat{\mathbf{k}}$, with c being the speed of light.

- The spectral photon flux $\mathbf{j}_{\mathrm{ph},\nu}(t, \mathbf{x}, \hat{\mathbf{k}})$ can be derived by multiplication of $n_{\mathrm{ph},\nu}$ with the photon speed c in direction $\hat{\mathbf{k}}$:

$$\mathbf{j}_{\mathrm{ph},\nu}(t, \mathbf{x}, \hat{\mathbf{k}}) = n_{\mathrm{ph},\nu}(t, \mathbf{x}, \hat{\mathbf{k}})\, \mathbf{c} = n_{\mathrm{ph},\nu}(t, \mathbf{x}, \hat{\mathbf{k}})\, c\, \hat{\mathbf{k}}. \tag{3.3}$$

- The spectral energy flux $\mathbf{j}_{\mathrm{rad},\nu}(t,\mathbf{x},\hat{\mathbf{k}})$ can be immediately found from the photon flux by multiplication with the energy of a photon $h\nu$:

$$\mathbf{j}_{\mathrm{rad},\nu}(t,\mathbf{x},\hat{\mathbf{k}}) = \mathbf{j}_{\mathrm{ph},\nu}(t,\mathbf{x},\hat{\mathbf{k}})\, h\,\nu = c\, n_{\mathrm{ph},\nu}(t,\mathbf{x},\hat{\mathbf{k}})\,\hat{\mathbf{k}}\, h\,\nu. \tag{3.4}$$

- The right hand side of equation 3.4 is called the spectral intensity $I_\nu(t,\mathbf{x},\hat{\mathbf{k}})$:

$$I_\nu(t,\mathbf{x},\hat{\mathbf{k}}) = c\, n_{\mathrm{ph},\nu}(t,\mathbf{x},\hat{\mathbf{k}})\, h\,\nu. \tag{3.5}$$

  $I_\nu(t,\mathbf{x},\hat{\mathbf{k}})$ is the fundamental quantity, which describes a radiation field. By definition, $I_\nu(t,\mathbf{x},\hat{\mathbf{k}})$ describes the propagation of energy within the frequency interval $(\nu,\nu+\mathrm{d}\nu)$ through a unit surface element oriented normal to $\hat{\mathbf{k}}$. $I_\nu(t,\mathbf{x},\hat{\mathbf{k}})$ is also defined per solid angle $\mathrm{d}^2\hat{k}$, such that it does not depend on the distance to a considered object.

- The spectral mean intensity $J_\nu(t,\mathbf{x})$ can be obtained from the spectral intensity $I_\nu(t,\mathbf{x},\hat{\mathbf{k}})$:

$$J_\nu(t,\mathbf{x}) = \frac{1}{4\pi}\int_\Omega I_\nu(t,\mathbf{x},\hat{\mathbf{k}})\,\mathrm{d}^2\hat{k}. \tag{3.6}$$

- The spectral radiation flux $\mathbf{F}_\nu(t,\mathbf{x})$ results from integrating the directional energy flux $\mathbf{j}_{\mathrm{rad},\nu}(t,\mathbf{x},\hat{\mathbf{k}})$ over all directions:

$$\mathbf{F}_\nu = \int_\Omega \mathbf{j}_{\mathrm{rad},\nu}\,\mathrm{d}^2\hat{k} = \int_\Omega I_\nu(t,\mathbf{x},\hat{\mathbf{k}})\,\hat{\mathbf{k}}\,\mathrm{d}^2\hat{k}. \tag{3.7}$$

  $\mathbf{F}_\nu(t,\mathbf{x})$ has a dimension of [J m$^{-2}\cdot$ s $\cdot$ Hz]. For an isotropic radiation field, where I_ν is independent of $\hat{\mathbf{k}}$, $\mathbf{F}_\nu(t,\mathbf{x})$=0 holds.

3.2 Radiative transfer equation

The radiative transfer equation describes the temporal and spatial evolution of the specific intensity $I_\nu(t,\mathbf{x},\hat{\mathbf{k}})$, when radiation passes through matter:

$$\begin{aligned}\frac{1}{c}\frac{\partial I_\nu(t,\mathbf{x},\hat{\mathbf{k}})}{\partial t} + \hat{k}_i\frac{\partial I_\nu(t,\mathbf{x},\hat{\mathbf{k}})}{\partial x_i} = &- [\kappa_\nu(t,\mathbf{x}) + \bar{s}_\nu(t,\mathbf{x})]\, I_\nu(t,\mathbf{x},\hat{\mathbf{k}}) \\ &+ \eta_\nu^{\mathrm{ind}}(t,\mathbf{x})\, I_\nu(\hat{\mathbf{k}}) + \eta_\nu^{\mathrm{sp}}(t,\mathbf{x}) \\ &+ \int_\Omega s_\nu(t,\mathbf{x},\hat{\mathbf{k}}'\to\hat{\mathbf{k}})\, I_\nu(t,\mathbf{x},\hat{\mathbf{k}}')\,\mathrm{d}^2\hat{k}',\end{aligned} \tag{3.8}$$

where x_i (i=1,2,3) denotes the Cartesian coordinates and the vector $\hat{\mathbf{k}}$ the photon propagation direction.
The transport coefficients $\chi_\nu, \kappa_\nu, \eta_\nu, s_\nu$ describe the interaction of photons with the medium as summarized below:

- The loss of radiation along its trajectory of propagation is expressed by the absorption coefficient κ_ν, being the isotropic monochromatic absorption coefficient at frequency ν, whereas $\hat{\kappa}_\nu = \kappa_\nu - \eta_\nu^{\mathrm{ind}}$ is the net absorption coefficient.

- The differential scattering coefficient s_ν can be separated into an angle-independent part $\bar{s}_\nu$ and an angle dependent part ω_ν,

$$s_\nu(t, \mathbf{x}, \hat{\mathbf{k}}' \to \mathbf{k}) = \bar{s}_\nu \, \omega_\nu(\hat{\mathbf{k}}' \to \hat{\mathbf{k}}), \tag{3.9}$$

  where the scattering function $\omega_\nu(t, \mathbf{x}, \hat{\mathbf{k}}' \to \hat{\mathbf{k}})$ is normalized:

$$\int_\Omega \omega_\nu(\hat{\mathbf{k}}' \to \hat{\mathbf{k}}) \, \mathrm{d}^2\hat{k}' = 1, \tag{3.10}$$

  and the total scattering coefficient $\bar{s}_\nu$ is defined by

$$\bar{s}_\nu(\mathbf{x}, t) = \int_\Omega s_\nu(t, \mathbf{x}, \hat{\mathbf{k}}' \to \hat{\mathbf{k}}) \, \mathrm{d}^2\hat{k}'. \tag{3.11}$$

  In the case of isotropic scattering $\omega_\nu = 1/(4\pi)$.

- The spectral emission coefficient is denoted by η_ν. It consists of the spontaneous emission coefficient η_ν^{sp} and the induced emission coefficient η_ν^{ind}

$$\eta_\nu = \eta_\nu^{\mathrm{sp}}(t, \mathbf{x}) + \eta_\nu^{\mathrm{ind}}(t, \mathbf{x}) \, I_\nu(t, \mathbf{x}, \hat{\mathbf{k}}). \tag{3.12}$$

- It is convenient to combine the total scattering coefficient $\bar{s}_\nu$ and the absorption coefficient κ_ν into the extinction coefficient χ_ν, which describes the loss of radiation along the path of propagation due to absorption and scattering of photons from direction $\hat{k}$ into the new direction $\hat{k}'$

$$\chi_\nu = \kappa_\nu + \bar{s}_\nu. \tag{3.13}$$

  The net extinction coefficient can be defined as $\hat{\chi}_\nu = \chi_\nu - \eta_\nu^{\mathrm{ind}}$.

The calculation of the radiative transfer in the thin layers of the exosphere considered in this work (see chapter 6) provides some simplifications:

- Induced emission is considered to be negligible, since collisions are rare in the exosphere. Furthermore, the spontaneous emission of radiation from hydrogen atoms can be neglected at the low temperatures of the exosphere .

- The scattering medium considered in this work is atomic hydrogen (see chapter 6). Hence, isotropic scattering can be assumed, thus $\omega_\nu = 1/(4\pi)$.

- In the radiative transfer problem considered here, the typical time required for the radiation to travel a distance s is $t_{\rm ph} = s/c$, whereas the characteristic time required for a significant change of the transport coefficients due to hydrodynamical, thermodynamical and chemical evolution is t_χ. Since in the thin layer of the exosphere the distance s for a photon after it interacts with the exospheric medium is very large (in the order of 10^4 km), the radiative transfer problem can be treated in the stationary limit.

With the simplifications mentioned above, one obtains a simplified, time-independent radiative transfer equation:

$$\hat{k}_i \frac{\partial I_\nu(x, \hat{\mathbf{k}})}{\partial x_i} = -\chi_\nu(\mathbf{x})\, I_\nu(\mathbf{x}, \hat{\mathbf{k}}) + \bar{s}_\nu(\mathbf{x}) \frac{1}{4\pi} \int_\Omega I_\nu(\mathbf{x}, \hat{\mathbf{k}}')\, \mathrm{d}^2\hat{k}'. \tag{3.14}$$

By introducing the source function

$$S_\nu = \frac{\bar{s}_\nu}{\chi_\nu} \frac{1}{4\pi} \int_\Omega I_\nu(\mathbf{x}, \hat{\mathbf{k}}') \mathrm{d}^2\hat{k}', \tag{3.15}$$

One can express equation 3.14 as

$$\hat{k}_i \frac{\partial I_\nu(\mathbf{x}, \hat{\mathbf{k}})}{\partial x_i} = \chi_\nu(\mathbf{x}) \left[S_\nu(\mathbf{x}) - I_\nu(\mathbf{x}, \hat{\mathbf{k}}) \right]. \tag{3.16}$$

When describing the photon propagation along a ray of light, one might introduce $\mathbf{s} = s\,\hat{\mathbf{k}}$, with $s = \hat{\mathbf{k}}{\cdot}\mathbf{x}$ denoting the considered coordinate (position) in the ray of light propagating in direction $\hat{\mathbf{k}}$. One can therefore rewrite equation 3.14:

$$\frac{\partial I_\nu(s, \hat{\mathbf{k}})}{\partial s} = \chi_\nu(s) \left[S_\nu(s) - I_\nu(s, \hat{\mathbf{k}}) \right]. \tag{3.17}$$

3.3 Solution of the radiative transfer equation

Solutions to the equation of radiative transfer form an enormous body of work (e.g. Mihalas 1978). The differences however, are essentially due to the various forms for the emission and absorption coefficients. If scattering is ignored, then a general solution in terms of the emission and absorption coefficients can be obtained.
If one considers a very small area element in the radiation field, there will be radiative energy flowing through that area element. The flow can be

completely characterized by the amount of energy flowing per unit time per unit solid angle, the direction of the flow, and the wavelength interval being considered. The intensity differential along a length ds is given by:

$$\frac{\mathrm{d}I_\nu}{\mathrm{d}s} = -\chi_\nu I_\nu. \tag{3.18}$$

The solution to this equation is also known as "Lambert-Beer's law":

$$I_\nu(s) = I_\nu(s_0)\exp(-\tau_\nu(s_0, s)), \tag{3.19}$$

where $\tau_\nu(s_0, s)$ is the optical depth of the atmosphere between s_0 and s:

$$\tau_\nu(s_0, s) \equiv \int_{s_0}^{s} \chi(s')\mathrm{d}s' = \int_{s_0}^{s} \kappa(s') + \bar{s}_\nu(s')\mathrm{d}s'. \tag{3.20}$$

3.4 Quantities used in this work

This work considers the scattering of ultraviolet solar radiation on hydrogen atoms in Titan's exosphere in detail. In particular, this work focuses on the scattering of solar radiation at the Lyman-α wavelength (λ_0=121.56 nm). At this wavelength, hydrogen atoms resonantly scatter the radiation, i.e. the scattering of a photon by a hydrogen atom in which the atom first absorbs the photon by undergoing a transition from the ground state to the first excited level, and subsequently re-emits the photon by the exact inverse transition. Additionally, the absorption by methane molecules in the exosphere is considered. When a Lyman-α photon interacts with methane, methane is dissociated, and the photon is lost.
For a medium, in which scattering and absorption occurs, the total optical depth along a path s can be expressed as

$$\tau(s) = (\sigma_a n_a(s) + \sigma_s n_s(s)) \cdot s, \tag{3.21}$$

with σ_s being the scattering cross section and n_s the number density of scattering particles, whereas σ_a and n_a are absorption cross section and number density of the absorbing particles, respectively.
The cross section σ is used to quantify the probability of a certain particle-particle interaction, e.g., scattering, absorption, etc. (Note that electro magnetic radiation is described in this context as consisting of particles, i.e. photons) and has the dimensions of an area [m^2].
For Lyman-α radiation at UV wavelengths, the methane photodissociation cross section is independent of the temperature and the wavelength. The cross section is obtained from Vatsa and Volpp (2001): $\sigma_{\mathrm{CH_4}} = 2.0 \cdot 10^{-17}$

cm^2.

The wavelength dependent resonance scattering cross section of atomic hydrogen is given by

$$\sigma_{\mathrm{H}}(\lambda) = \frac{f_{Ly\alpha}\mu_0 e^2 \lambda_0^2}{4\sqrt{\pi} m_e \Delta\lambda_D} \exp\left[-\left(\frac{\lambda - \lambda_0}{\Delta\lambda_D}\right)^2\right], \tag{3.22}$$

with e, m_e being the charge and mass of the electron, $f_{Ly\alpha}$ the oscillator strength of Lyman-α ($f_{Ly\alpha} = 0.4163$), μ_0 the permeability of free space and $\Delta\lambda_D$ the Doppler width:

$$\Delta\lambda_D = \frac{\lambda_0}{c} v_p = \frac{\lambda_0}{c}\sqrt{\frac{2k_B T}{m_{\mathrm{H}}}}, \tag{3.23}$$

with k_B being the Boltzmann constant, m_{H} the mass of a hydrogen atom, T the exospheric temperature and c the speed of light. Note here, that v_p is the thermal velocity of atomic hydrogen (see section 2.3). Equation 3.22 assumes that the scattering is isotropic in the atom's frame of reference. This assumption is almost correct, if the incident radiation is completely unpolarized; it is not expected to lead to any large error in the calculation, because multiple scattering has a strong depolarizing effect on the radiation. Setting $v_p = \sqrt{2k_B T/m_{\mathrm{H}}}$ is strictly speaking only valid, if the particle velocities obey the Maxwell-Boltzmann distribution of velocities, which is only valid close to the exobase. Above the exobase, the particles have a radial velocity component, hence the most probable velocity can no longer be obtained from the Maxwell-Boltzmann distribution. However, as a first order approximation one can assume a Maxwellian distribution of velocities and obtain for an exospheric temperature of $T = 150\,\mathrm{K}$ a Doppler width of $\Delta\lambda_D = 6.38 \cdot 10^{-13}\,\mathrm{m}$, hence the scattering cross section at Lyman-α is $\sigma = 4.815 \cdot 10^{-17}\,\mathrm{m}^2$ (see also Figure 3.1).

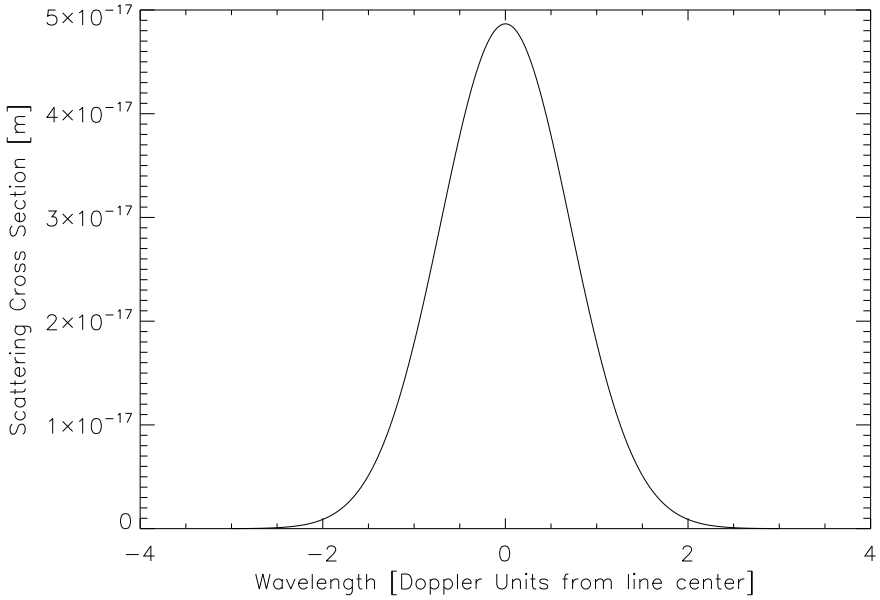

Fig. 3.1: Atomic hydrogen resonance scattering cross section as a function of wavelength. The wavelength is expressed in units of Doppler width. The cross section is shown for a temperature of 150 K

3.5 The Monte Carlo method

The Monte Carlo method does not yield closed solutions of a problem, but solves it by computing a chain of stochastic single events. In the present problem the path of a photon through the exosphere of Titan is simulated by means of automatically generated random numbers, evenly distributed in the interval (0,1), which determine the current values of the physical variables. A general introduction to the Monte Carlo method can be found in e.g. Cashwell and Everett (1959).

One firstly introduces the basic physics of the problem in the program code in a probabilistic fashion. A system of coordinates and boundaries are defined and then photons are released from the source. These photons are traced as they diffuse through the prescribed medium following the probabilistic interaction laws, which are sampled by the selection on numbers from a random sequence. The photons are followed until they escape from the medium or are absorbed by the medium.

When a photon is emitted from the source and sent into a direction $\hat{\mathbf{k}}$, it will travel a distance l before it is either absorbed or scattered into a new direction. However, the distance traveled and the scattering direction can not be uniformly chosen from all space or all angles, since there are proba-

bility distribution functions associated with these quantities. Therefore, the optical depth and scattering angle must be sampled, such that they obey the probability density distribution function $P(x)$.

At this point the **fundamental principle** of the Monte Carlo method is introduced (Cashwell and Everett 1959 for details):
If $E_1, ..., E_n$ are n independent events with probabilities $p_1, ..., p_n$ and $p_1 + ... + p_n = 1$, the fundamental principle is, that a random variable r, with

$$p_1 + ... + p_{i-1} \leq r < p_1 + ... + p_i \tag{3.24}$$

determines E_i.

When arbitrarily assigning a variable x in the interval $0 \leq x < n$ to the events $E_1, ..., E_n$ with $i - 1 \leq x < i$ representing the event E_i, then one can construct a probability density function p(x) by the definition

$$p(x) \equiv p_i \qquad i \leq x < i \qquad i = 1, ..., n$$

Thus, $p(x)$ will be a step function. One can now define a probability density distribution function

$$P(x) = \int_0^x p(\xi)\mathrm{d}\xi. \tag{3.25}$$

Note that $p(\xi)$ is normalized:

$$\int_0^x p(\xi)\mathrm{d}\xi = 1. \tag{3.26}$$

Then, the equation

$$r = P(x) = \int_0^x p(\xi)\mathrm{d}\xi \tag{3.27}$$

determines x uniquely as a function of r, in such a way, that if r is uniformly distributed on the interval $0 \leq r < 1$, then the variable x falls with frequency p_i in the interval $i - 1 \leq x < i$, thereby determining the event E_i.

3.6 Example: Radiative transfer in a plane-parallel atmosphere

The probability that a photon travels a certain path through a homogenous medium without interaction is $\exp(-\tau)$. The probability of an interaction

inside the medium is hence $P(\tau) = 1-\exp(-\tau)$. By applying the fundamental principle, one can sample the optical depth to the first interaction from

$$r = P(\tau) = 1 - \exp(-\tau), \tag{3.28}$$

with r being a random number equally distributed in [0,1].
Since also $1 - r$ is equally distributed on $0 \leq r \leq 1$, one finds

$$\tau = \ln(1 - r). \tag{3.29}$$

Having sampled a random optical depth in this way, the physical distance l traveled by the photon can be calculated from:

$$\tau = \int_0^l n\,\sigma\,\mathrm{d}l. \tag{3.30}$$

In general, l can not be found analytically from equation 3.30, so one must use numerical techniques, which can be computationally intensive and time consuming. Nevertheless, one finds l analytically, when the quantity $n \cdot \sigma$ is only changing slowly with $\mathrm{d}l$ - this allows the generation of large numbers of photons in a fraction of the time required to solve equation 3.30 numerically. Applying the Monte Carlo method, equation 3.30 can be solved by tracing a statistically meaningful number of photons through the medium.

Furthermore, when considering a plane-parallel atmosphere homogenously filled with an absorbing medium, starting a large number of photons and following them through the medium, one is able to sample the transmission and vice-versa the optical depth of the atmosphere. For each photon a random mean free path can be calculated according to

$$l_0 = -\frac{1}{n \cdot \sigma} \ln(r_i), \tag{3.31}$$

with r_i being a random number equally distributed in (0,1). For every photon started in this way, the random mean free path is compared to the height l of the atmospheric layer. If l_0 is lower than l, this particular photon will be absorbed inside the medium.
When now starting a large number of photons and counting the number of photons flying through the medium without any interaction, one can sample the transmission of the medium $\mathcal{T} = \exp(-\tau)$.
As an example, the optical depth of the medium is assumed to be $\tau = 1$. Then, the transmission of the medium is hence $\mathcal{T} = 0.36787945$. However, if the optical depth is not known, then using a low number of photons means

that the statistics is not sufficient in order to sample the transmission: Using 10 photons for the calculations, e.g. only 4 photons are transmitted through the medium, hence yielding a transmission of 0.4. Increasing the number of photons also increases the accuracy of the output: with a number of $1 \cdot 10^4$ photons, an average transmission of 0.36930 is obtained. When using $1 \cdot 10^6$ photons, a transmission of 0.36791610 can be obtained, which still differs slightly from the direct calculation due to rounding errors.

4. THE CASSINI/HDAC MEASUREMENTS

This chapter first gives a short overview about the Cassini mission. Afterwards the the HDAC instrument is described in detail, including the measurement principle and the calibration of the instrument. Furthermore this chapter describes the measurements performed by HDAC during the T_9 encounter in 2005 as well as the data reduction.

4.1 The Cassini mission

The Cassini-Huygens mission is a joint venture mission of the European Space Agency (ESA), National Aeronautics and Space Administration (NASA) and the Italian Space Agency (ASI - Agenzia Spaziale Italiana). The Cassini orbiter was developed and constructed at the Jet Propulsion Laboratory (JPL), while the Huygens probe was supplied by the ESA. ASI provided the high-performance antenna for the radio link between Huygens and Cassini. The main scientific objectives for the Cassini-Huygens mission are studying Saturn's rings and its atmosphere, its satellites' surfaces, the geological history of each object in the Saturnian system and Titan's atmosphere and surface in more detail.

Cassini-Huygens is the second largest interplanetary spacecraft ever launched with 27 scientific instruments on board. The spacecraft consists of the orbiter itself and the attached Huygens probe which was released to enter Titan's atmosphere (see Figure 4.1). The spacecraft has a height of 6.8 m. Its maximum diameter, determined by the High Gain Antenna (HGA) is 4 m, not including the deployed magnetometer boom and antennas. The total weight after separation from the launch vehicle is estimated to be 5,630 kg.
Cassini is three axes stabilized through reaction and momentum wheels and small hydrazine thrusters. Large trajectory maneuvers are accomplished by two main engines, minor corrections are realized by the use of smaller thrusters. Reference star sensors, Sun sensors and gyroscopes allow precise attitude determination. Three radioisotope thermoelectric generators provide power for engineering and scientific electronic devices. The orbiter

communicates with the Earth via the High Gain Antenna (HGA) and two low gain antennas (LGA).

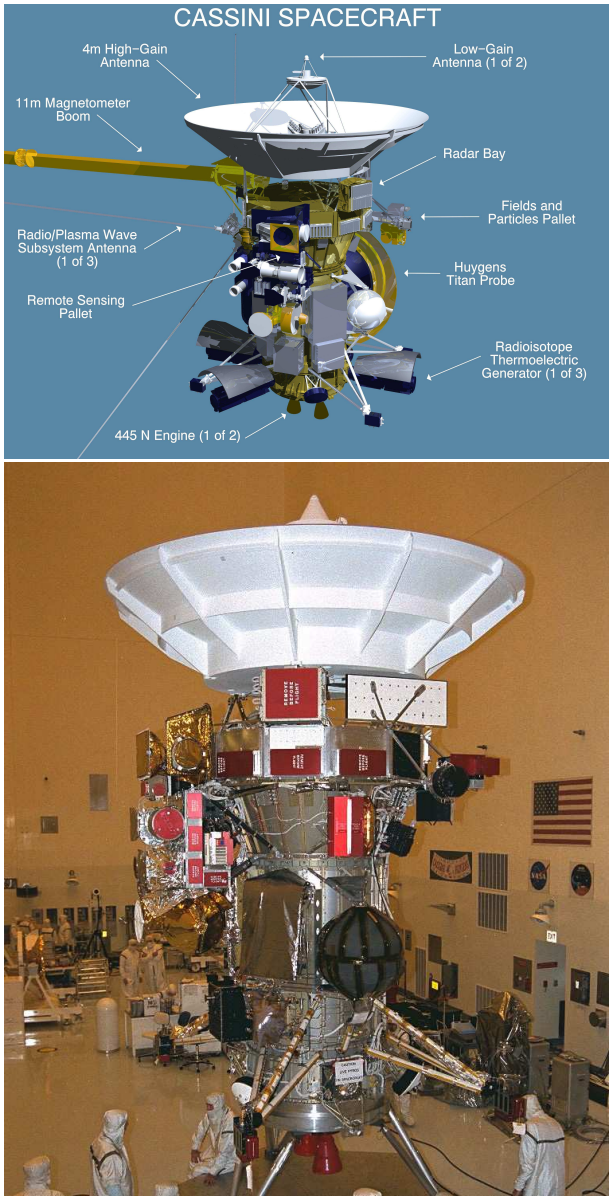

Fig. 4.1: The Cassini spacecraft. The UVIS instrument is part of the "Remote Sensing Pallet", as indicated in the upper figure. In the lower image, the Huygens probe has not been attached at the time of the photograph. Image credits: NASA/JPL

The Cassini-Huygens spacecraft was launched on October 15, 1997 from the Cape Canaveral Air Force Station. It arrived at Saturn on July 2, 2004 after several swing-by maneuvers at Venus, Earth and Jupiter. The Cassini orbiter was scheduled to orbit Saturn and its moons four years until June 2008. In July 2008, a two-year mission extension for the Cassini mission begun, called the "Cassini Equinox Mission". During the Equinox mission, the Cassini spacecraft will continue its tour through the Saturnian system and will perform several close targeted flybys as well as many distant flybys of Saturn's moons. This includes 26 Titan flybys, 7 Enceladus flybys, and one flyby each of the icy moons Dione, Rhea and Helene.

The Huygens probe was released from Cassini on December 26, 2004 entering Titan's atmosphere on January 14, 2005. It collected large amounts of scientific and image data during its 27 minute descent through the atmosphere, and 60 more minutes collecting data at the surface, sending it to Earth via the Cassini orbiter.

4.2 Description of the HDAC instrument

The Hydrogen Deuterium Absorption Cell (HDAC) is part of the Ultraviolet Imaging Spectrograph (UVIS) aboard the Cassini orbiter. Figure 4.1 shows UVIS as part of the "Remote Sensing Pallet". The HDAC instrument was designed to determine the D/H ratio of Titan's and Saturn's atmospheres. HDAC measures the relative abundance of atomic deuterium and hydrogen from their Lyman-α emission at 121.533 nm and 121.567 nm, respectively. A general description of UVIS and HDAC can be found in Esposito et al. (2004).

HDAC consists of a baffle for suppressing scattered light, three absorption cells and a Channel Electron Multiplier, which will be hereafter referred to as the "photometer" (see Figure 4.2). One HDAC absorption cell consists of a long tube, 8.5 cm in length and with a diameter of 2.5 cm, separated by Magnesium fluoride (MgF_2) windows. MgF_2 has a transmission range between 115 nm and 7,500 nm (Heath and Sacher, 1966). A single 2.5 cm diameter MgF_2 lens attached to the front of the instrument focuses the incoming light onto the detector, yielding a circular field of view (FOV) of 3° in diameter ($6.85{\cdot}10^{-4}$ steradians).
The absorption cells are filled with molecular hydrogen, oxygen and deuterium, respectively. Oxygen acts as a broad band filter from 115 nm to 180 nm, except for a transmissive window in the Lyman-α region (Maki,

1993). Unfortunately, the oxygen cell had to be vented prior to flight, hence HDAC is now sensitive to a very broad wavelength range from 115 nm to 240 nm.

The hydrogen and deuterium cells (hereafter referred to as "H cell" and "D cell") are heated via a hot tungsten filament to dissociate the molecules into atoms. The atoms resonantly absorb the hydrogen and deuterium Lyman-α radiation passing through the cells, which leads to a decreasing count rate in the photodetector. Thus, the cells act as adjustable filters: by switching the filaments on and off and measuring the differences in signal strength, the instrument can measure in this ways the intensity of the incoming Lyman-α radiation for atomic hydrogen and deuterium. Since the atomic density in the cells depends on the filament temperature, a set of different absorption "filters" can be attained.

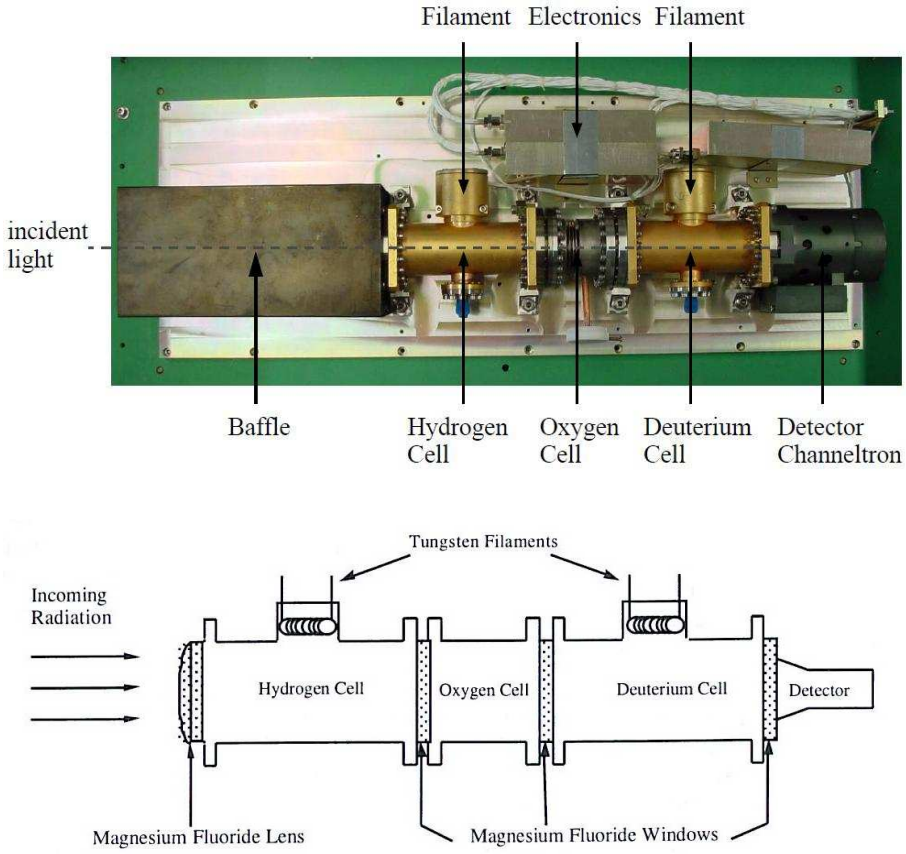

Fig. 4.2: Detailed overview of the HDAC instrument (Esposito et al., 2004).

4.3 Measurement principle

The absorption cells are operated at a temperature of $T_{HDAC} = 300\,\mathrm{K}$. When no power is applied to the filaments, the absorption cells contain only

molecules, and the cells are transparent with respect to incoming Lyman-α radiation. When power is applied to the filament in the cell, the molecules dissociate into atoms, which weaken the incoming Lyman-α radiation by absorption. The wavelength-dependent transmission

$$\mathcal{T}(\lambda) = \exp\left[-n\sigma(\lambda, T_{\mathrm{HDAC}})L\right] = \exp\left[-\tau(\lambda)\right] \tag{4.1}$$

of the cells is a function of the length of the cell ($L = 8.5\,\mathrm{cm}$), the wavelength and temperature dependent resonance scattering cross section $\sigma(\lambda, T_{\mathrm{HDAC}})$, and the atomic number density n, which in turn depends on the filament power.
The wavelength dependent resonance scattering cross section of atomic hydrogen is given by

$$\sigma(\lambda, T_{\mathrm{HDAC}}) = \sigma_0(T_{\mathrm{HDAC}}) \exp\left(\frac{\lambda - \lambda_0}{\Delta\lambda}\right), \tag{4.2}$$

with σ_0 being the cross section at the line center ($\lambda_0 = 121.567\,\mathrm{nm}$) and $\Delta\lambda$ the Doppler width. At a cell temperature of $T_{\mathrm{HDAC}} = 300\,\mathrm{K}$, the cross section for atomic hydrogen at the line center is $\sigma_0 = 3.4 \cdot 10^{-13}\,\mathrm{cm}^2$. See chapter 3.8 for a detailed derivation of the optical depth and the resonance scattering cross section.

HDAC is sensitive to radiation over a wide spectral range, hence the signal measured is directly proportional to the integrated intensity of the incoming radiation over this range. The total signal can be expressed as

$$I = \int_0^\infty S(\lambda) H(\lambda) \mathcal{T}(\lambda) \mathrm{d}\lambda, \tag{4.3}$$

where I is the measured signal by the photodetector, $H(\lambda)$ is the intensity of the radiation, $S(\lambda)$ is the sensitivity of the whole instrument (including the sensitivity of the detector and the transmission of the MgF_2 windows), and $\mathcal{T}(\lambda)$ is the transmission of the filter provided by the absorption cells. The ratio of the modulated intensity I to the unmodulated intensity I_0 (assuming no background) is given by the factor

$$R = \frac{I}{I_0} = \frac{\int_0^\infty S(\lambda) H(\lambda) \mathcal{T}(\lambda) \mathrm{d}\lambda}{\int_0^\infty S(\lambda) H(\lambda) \mathrm{d}\lambda}. \tag{4.4}$$

Because the background level is unknown, it can be eliminated from the measurement by taking the difference of modulated and unmodulated signals,

giving an effective filter

$$I_0 - I = \int_0^\infty S(\lambda)H(\lambda)[1 - \mathcal{T}(\lambda)]\mathrm{d}\lambda. \tag{4.5}$$

Due to the movement of the spacecraft with respect to Titan (resulting in a Doppler shift of the measured Lyman-α lines), HDAC is able to measure the line shape of the Lyman-α line: during ingress, the relative speed of the approaching spacecraft with respect to Titan is negative, hence the emitted Lyman-α radiation is shifted with respect to the HDAC absorption, allowing HDAC to absorb radiation redwards of the emitted radiation. Close to the closest approach the Doppler shift is zero, hence HDAC absorbs radiation exactly at the line center and during egress the blueward side of the Lyman-α radiation emitted by Titan is absorbed.

4.4 HDAC Calibration

Pre- and inflight cell calibrations have been summarized in Maki (1993), Warlich (1997) and Regehly (2003). Here the important points of these works are reviewed.

4.4.1 Sensitivity

The sensitivity $S_{\mathrm{Ly}\alpha}$ of the instrument is the count rate per input flux:

$$S_{\mathrm{Ly}\alpha} = \frac{10^6}{4\pi} \cdot \mathrm{QE} \cdot \Omega \cdot \mathcal{T}_\mathrm{W}^3 \cdot \mathcal{T}_\mathrm{L}, \tag{4.6}$$

where $S_{\mathrm{Ly}\alpha}$ is in units of counts per second and Rayleigh ($\mathrm{cts\,s^{-1}\,R^{-1}}$), QE is the quantum efficiency of the CEM detector in units of counts per photon ($\mathrm{cts\,ph^{-1}}$), Ω is the solid angle of the FOV of HDAC in units of steradians, $\mathcal{T}_\mathrm{W}^3 \cdot \mathcal{T}_\mathrm{L}$ is the transmission of the three MgF_2 windows and the single lens. $S_{\mathrm{Ly}\alpha}$ was calibrated using measurements of the local interstellar medium (LISM) and comparing them with a model, being $S_{\mathrm{Ly}\alpha} = 29 \pm 3\,\mathrm{cts\,s^{-1}\,R^{-1}}$ (R. Reulke, priv. com.) during the time of the flyby considered in this work, with a detector quantum efficiency of $\mathrm{QE} = 0.78\,\mathrm{cts\,ph^{-1}}$. In general, the sensitivity of an instrument decreases with time, with the highest sensitivity at the beginning of the mission and then slowly decreasing to a stable value. See Figure 4.3 for the sensitivity change during 2005 (R. Reulke, priv. com.). The sensitivity of HDAC over the FOV is shown in Figure 4.4. Note that recent measurements of the HDAC sensitivity indicate a value of

$S_{\mathrm{Ly}\alpha} = 14\,\mathrm{cts\,s^{-1}\,R^{-1}}$ for the year 2009 (R. Reulke, priv. com.).

The photodetector is able to detect radiation within two pre-defined integration times of 0.125 s and 4 s. From the calibration measurements, the CEM integration time was chosen to be 0.125 s to avoid so-called rollover events. Rollover events mainly occur because the detector accuracy is limited to 16 bit, hence the maximum number of counts is 65,536. If an overflow is detected, then its value is reset, leading to a spike in intensity. Mainly rollover events appear when observing with an integration time of 4 s.

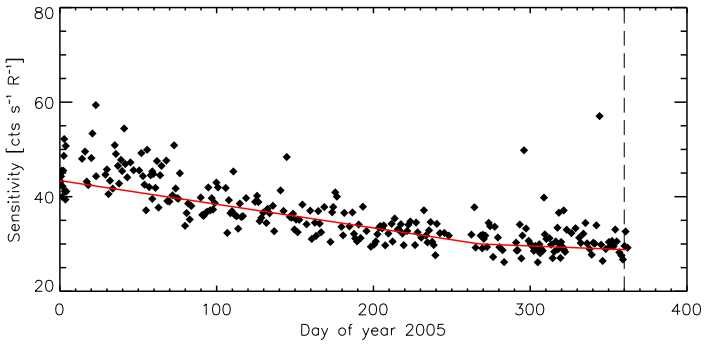

Fig. 4.3: HDAC sensitivity change during 2005. The sensitivity has been fitted by a linear fit (solid red line). During the T_9 flyby (vertical long-dotted line) the instrument sensitivity was $29 \pm 3\,cts\,s^{-1}\,R^{-1}$. Data provided by R. Reulke (priv. com.).

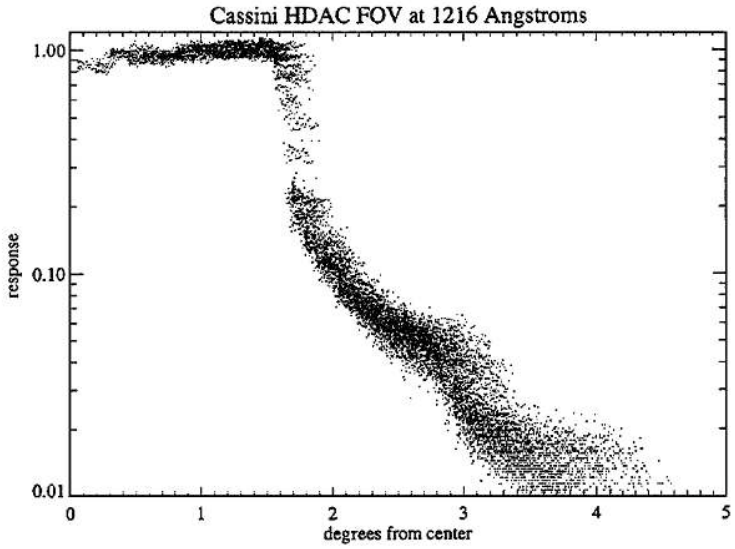

Fig. 4.4: Off-axis response of HDAC's circular FOV. Image obtained from Esposito et al. (2004).

4.4.2 Cell optical depths

During the preflight calibrations, the optical depths of both absorption cells were measured as displayed in table 4.1, showing a significant contamination of the deuterium cell with hydrogen: τ_{HD} is the atomic deuterium optical depth in the H cell and τ_{DH} the atomic hydrogen optical depth in the deuterium cell. The H cell, however, was not contaminated by deuterium.

Prior to the T_9 flyby considered in this work, HDAC was again calibrated by measuring the local interstellar medium as well as performing photometry on bright stars. The measured modulation, as inferred from LISM (local interstellar medium) and Jupiter measurements, was much lower than expected with optical depths as shown in table 4.2. The D cell showed a strong signal excess. Moreover, it was not possible to infer the deuterium optical depth because the objects observed exhibited themselves a very faint D-Lyman-α line due to very low D/H ratios. Nevertheless the atomic hydrogen optical depth in both cells could be determined.

Tab. 4.1: Preflight calibration of optical depth versus filament power step in the H and D cell, respectively.

Filament voltage step	H cell		D cell	
	τ_{H}	τ_{HD}	τ_{D}	τ_{DH}
0	0.0	0.0	0.0	0.0
1	0.0796	0.0	0.3	0.02
2	0.668	0.0	1.5	0.16
3	1.062	0.0	2.8	0.25
4	1.533	0.0	4.5	0.37
5	3.193	0.0	6.2	0.87
6	3.855	0.0	7.5	1.06
7	4.555	0.0	10.0	1.28

Tab. 4.2: Inflight calibration of the optical depth versus filament step in the H and D cell. It was not possible to determine the deuterium optical depth in the deuterium cells (indicated by "-").

Filament voltage step	H cell		D cell	
	τ_H	τ_{HD}	τ_D	τ_{DH}
0	0.0	0.0	-	0.0
1	0.0024	0.0	-	0.0336
2	0.0468	0.0	-	0.0
3	0.085	0.0	-	0.01639
4	0.1073	0.0	-	0.1118
5	0.4081	0.0	-	0.2401
6	0.6553	0.0	-	0.2241
7	0.8655	0.0	-	0.2239

4.5 Titan T_9 flyby

HDAC measurements have so far only performed once due to the above mentioned problems. Therefore this work focuses on measurements performed during the T_9 flyby on December 26, 2005. This work provides for the first time a data analysis of the T_9 flyby measurements.

4.5.1 Overview

The T_9 encounter lasted from 17:53:34 h (UTC, timestep 0 in Figure 4.5) until 19:59:33 h (UTC, timestep 840), reaching its closest approach at 18:59:25 h (timestep 439). Note that one timestep corresponds to a time span of 9 s, starting at the beginning of the observations (see next section for details). HDAC measurement started at a distance of 25,468.9 km to Titan's center, decreasing to a lowest distance of 12,985.0 km (closest approach) and then again increasing to 23,855.9 km at the end of the encounter (see Figure 4.5, top panel).

At the beginning of the encounter, the spacecraft had a relative speed of -4.70 $km\,s^{-1}$ with respect to Titan becoming zero at timestep 402. At the end of the encounter, the relative speed of the departing spacecraft with respect to Titan was 4.94 $km\,s^{-1}$ relative to Titan. Note that the relative speed became zero at timestep 402 and not during the closest approach. The corresponding Doppler shift of the emitted Lyman-α radiation with respect to the absorption of HDAC is shown in the center panel of Figure 4.5.

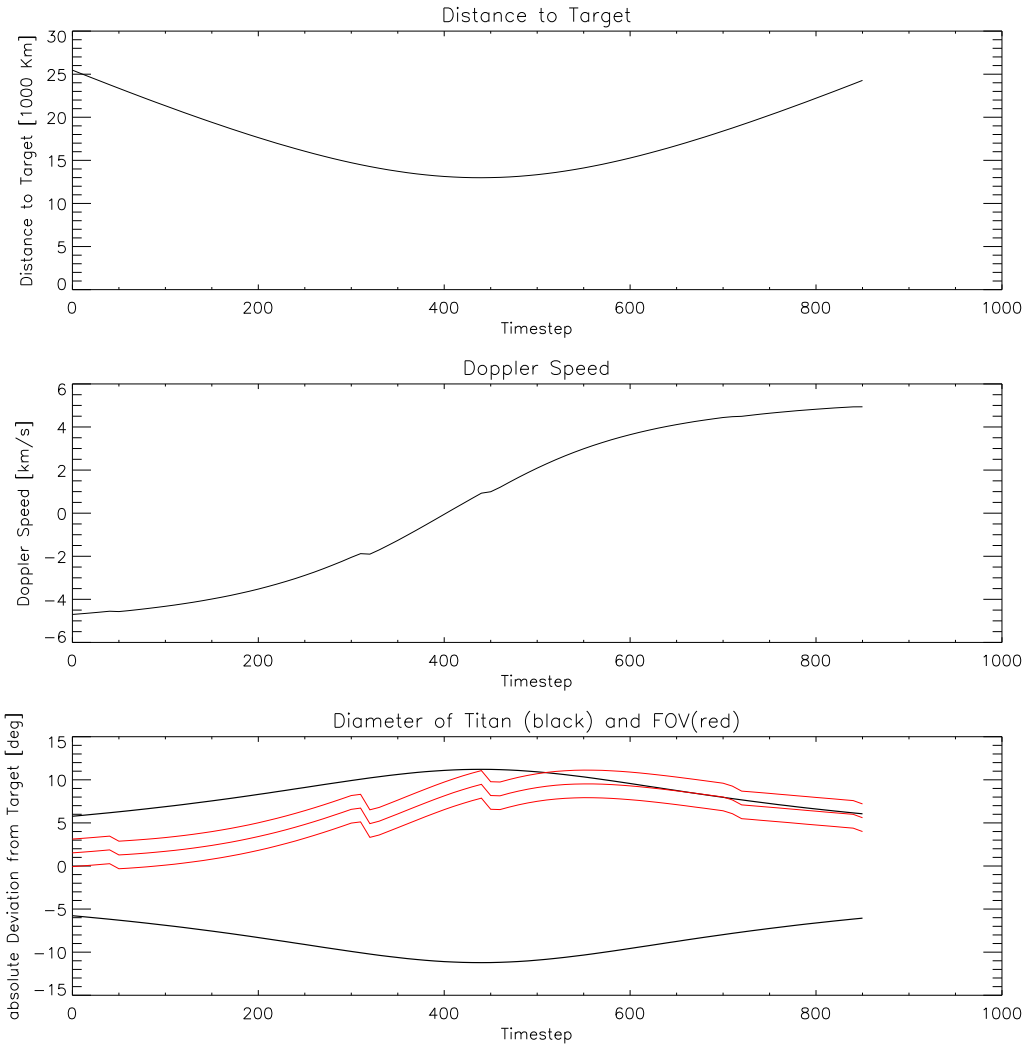

Fig. 4.5: Parameters during the T_9 encounter of Cassini with Titan:
Uppermost plot showing the distance to Titan, the second plot showing the Doppler speed, and the third plot the diameter of Titan's disc and the FOV projected onto Titan's disc (red lines). One time step corresponds to 9 s integration time, starting at 17:53:34 h UTC.
The four drops at timesteps 50, 320, 440 and 720 in the Doppler speed and in the FOV data indicate an adjustment of the Cassini orbiter in order to track Titan. The fourth drop is only visible in the FOV data.

The angular diameter of Titan changed between 8 to 12° (black lines in lowermost plot of Figure 4.5). The HDAC observations started near the sub-solar point, moving over Titan's disc to the terminator (central red line in lowermost plot of Figure 4.5). The latitude at closest approach was 0° (equator).

Approximately 1.4 hours after the beginning of the observations, the Visual and Infrared Mapping Spectrometer (VIMS) performed observations of Ti-

tan's surface (parallel to the HDAC observations) with several slow scans across Titan's visible hemisphere to obtain spectral images (timestep 560), with a limb scan of Titan at the end of the encounter. This is visible in the lowermost plot of Figure 4.5 after timestep 500.
The solar zenith angle (SZA), i.e. the angle between the viewing direction and the solar direction changed from 20° at the beginning of the encounter to 130° at the end (see Figure 4.6). Close to closest encounter, the viewing direction was perpendicular to the solar direction.

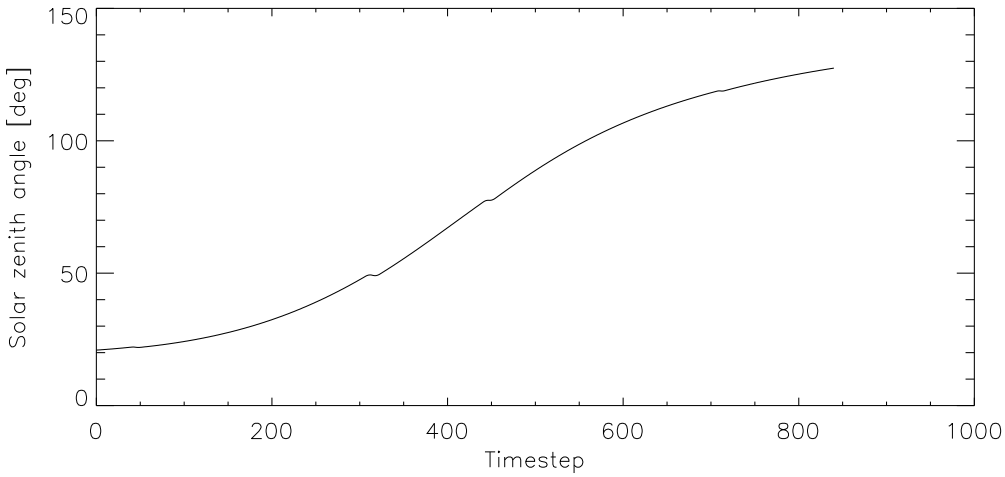

Fig. 4.6: Change of solar zenith angle during the flyby. The solar zenith angle is the angle between the viewing direction of HDAC and the solar direction.

4.5.2 Measurements

Prior to the T_9 flyby, HDAC was calibrated on the LISM as well as on Jupiter. The optical depths determined during these "inflight" calibrations were lower than in preflight calibrations (see section 4.4). The deuterium and hydrogen absorption cells of HDAC were therefore operated using a sequence of filament steps, defined by the maximum voltage level (voltage step "7") and cells off (voltage step "0") during the flyby.
One sequence was made of 16 voltage steps, where during the first step both cells were switched off. Afterwards the H cell was switched on for the rest of the sequence and the D cell was switched on every second step, hence the whole voltage sequence pattern is [0777777777777777] for the H cell and [0707070707070707] for the D cell. At a filament step of "7" the atomic hydrogen optical depth in the H cell is τ_{HH}=0.865 and τ_{HD}=0.224 in the D cell, whereas the deuterium optical depth in the D cell could not be determined (see table 4.2).

During the flyby, 53 sequences were performed, with a total detector integration time of 9 s per step. The count rate was measured using 72 single integrations for each step, with a duration of 0.125 s (72·0.125 s=9 s).

Figure 4.7 shows the measured signal during the T_9 flyby. Black diamonds represent measurements in photometer mode (both cells switched off), whereas red diamonds show the measurement performed with only the H cell switched on, and blue diamonds are measurements where both cells are switched on. The intensity drops in the measurement arise from FOV changes (at timesteps 50, 320, 440, and 720).

The measurements performed in photometer mode provide a measured intensity of $1.61 \cdot 10^4\,\mathrm{cts\,s^{-1}}$ at the beginning of the observations (timestep 0), decreasing to $1.41 \cdot 10^4\,\mathrm{cts\,s^{-1}}$ 50 minutes after the beginning of the observations (timestep 400). The closest approach altitude was reached at timestep 439, where a change in the pointing direction causes the signal to decrease to its lowest value of $1.32 \cdot 10^4\,\mathrm{cts\,s^{-1}}$. The signal was then increasing rapidly, even exceeding the signal at the beginning of the encounter: The maximum count rate of HDAC was measured at timestep 700, with a value of $1.92\,\mathrm{cts\,s^{-1}}$. During the limb scans, Titan no longer filled the FOV of the instrument. Although looking at the night side of Titan, Saturn was in the field of view during the limb scans, causing the count rate to exceed the value at the beginning of the observations.

When the H cell was switched on, the signal decreased to $1.58 \cdot 10^4\,\mathrm{cts\,s^{-1}}$ at the beginning of the encounter, compared to $1.61 \cdot 10^4\,\mathrm{cts\,s^{-1}}$ in photometer mode (both cells off). The Doppler shift was very large, which would suggest that absorption by the H cell at Lyman-α wavelengths should be small. Since the instrument looked at the sunlit side of Titan one might interpret this absorption, as that the H cell has either already absorbed a small part of the H Lyman-α emission line or the background was very high due to the missing broad band filter provided by the oxygen cell.

At timestep 402, when the Doppler speed was zero (cf. Figure 4.5), the signal decreased to $1.31 \cdot 10^4\,\mathrm{cts\,s^{-1}}$ - compared to $1.41 \cdot 10^4\,\mathrm{cts\,s^{-1}}$ in photometer mode this is a signal decrease of 7.1%.

When both cells were switched on, the above mentioned effect is also visible: At the start of the encounter, the count rate was $1.57 \cdot 10^4\,\mathrm{cts\,s^{-1}}$. Note that both measurements have a comparable countrate, although the transmission at the line center decreased by 21% when both cells were switched on. The absorption in the wings is nevertheless comparable. The count rate then de-

creased to a minimum value of $1.24 \cdot 10^4\,\mathrm{cts\,s^{-1}}$. Compared to the photometer measurement, this means a decrease of 12.1% and a decrease of 5% compared to the H cell measurements.

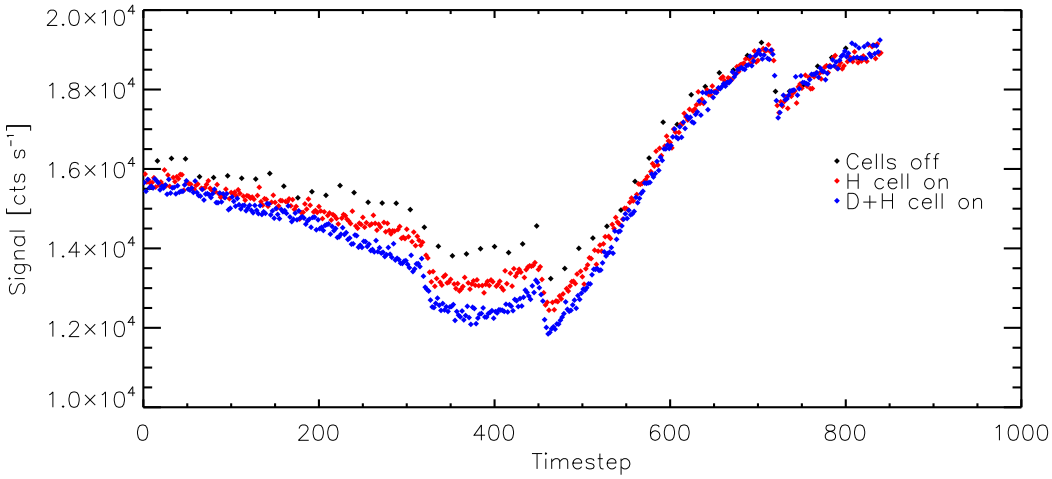

Fig. 4.7: HDAC measurements during the T_9 encounter with Titan. One timestep corresponds to 9 s of observations, starting at 17:53:34h UTC. Black diamonds are measurements performed in photometer mode (both cells switched off), whereas red and blue diamonds are measurements with only the H cell switched on and both cells switched on, respectively. Clearly visible is the undersampling of photometer measurements (every 16th step), when compared to measurements where one or both cells are switched on.

4.5.3 Difference signal and background removal

Background signals need to be removed in order to investigate the radiation emitted from Titan. The background signal is an additional signal which can be excluded by taking the difference between measurements performed in photometer mode and when the cells are switched on (I_0 and I, respectively, as given by the equations in section 4.3).

Background sources are the radiation from the LISM, the solar radiation and especially at the end of the encounter Saturn, which was in the FOV. The main reason for background signals is the missing oxygen cell, allowing the detection of radiation by the photodetector in a broad wavelength range from 115 nm to 240 nm. Below 115 nm radiation is blocked by the MgF_2 windows. The sensitivity of the instrument above 140 nm is of main importance, since beyond this wavelength the UV output of the sun begins to increase rapidly with increasing wavelength: Data from the **So**lar **R**adiation and **C**limate **E**xperiment (SORCE, Pankratz et al. 2005) show the solar spectrum in the wavelength range, HDAC is sensitive for (see Figure 4.8).

Undersampling is a significant problem when determining the difference signal directly: Only few measurements in photometer mode where performed among a large set of measurements where either the H cell or both cells were switched on. This causes the differential signal to result in spikes, especially during FOV changes. Figure 4.9 shows the differential signal $I_0 - I$ after applying a spline fit to the data, in order to adjust the different number of data points. Clearly visible is a frequent noise pattern, whose origin is so far unknown (R. Reulke, priv. com.). In order to avoid the spikes caused by undersampling, the average of measurements one step before and after each measurement in photometer mode is taken to calculate the difference signal. This decreases the number of data points to 52 points throughout the observation, which are still noisy but without spikes caused by undersampling (see Figure 4.10).

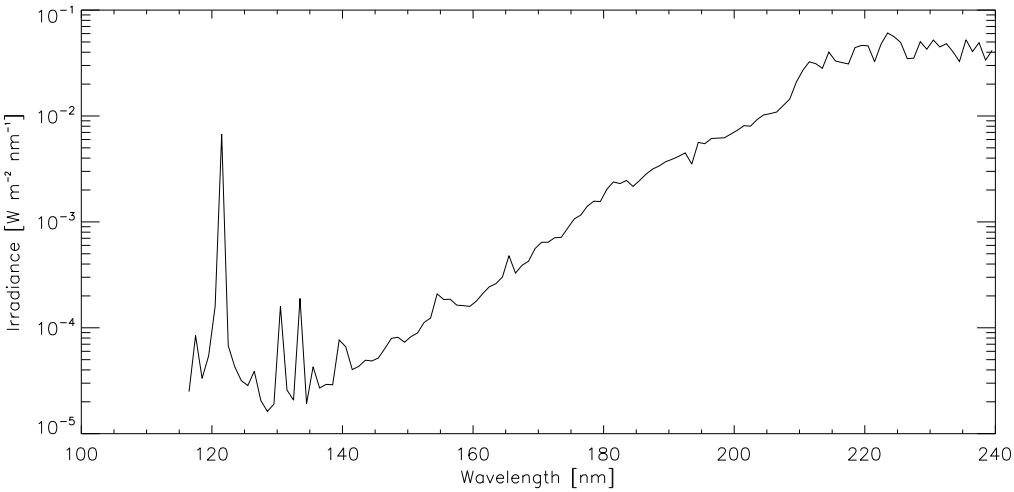

Fig. 4.8: Solar spectrum in the wavelength range, HDAC is sensitive for. Note that the irradiance is measured for a solar distance of 1 AU.
Data obtained from SORCE (`http://lasp.colorado.edu/sorce`*).*

The difference signal in Figure 4.10 gives a direct measurement of the Lyman-α radiation emitted from Titan. At the beginning of the encounter, when Cassini was approaching Titan, the negative Doppler speed allowed HDAC to absorb radiation in the line wings of the emitted Lyman-α line (redwards of the line center): Clearly visible is a signal exceed in both data sets of about $500\,\mathrm{cts\,s^{-1}}$ at the beginning of the observations. As the instrument was pointing towards the sunlit hemisphere of Titan and since any background sources have been excluded by taking the difference signal, HDAC thus has already absorbed Lyman-α radiation scattered in Titan's exosphere.
As the Cassini orbiter passes Titan, the Doppler speed increases and the HDAC absorption shifts to the line center of the emitted Lyman-α line. At

timestep 402 the Doppler speed was zero, allowing HDAC to absorb radiation exactly in the line center. The difference signal is about 800 cts s^{-1} when only the H cell was switched on, and about 1,700 cts s^{-1} when both cells were switched on. However, at this time HDAC already pointed to the terminator region. The closest approach altitude was reached at timestep 439. At the end of the encounter, HDAC was looking on the night side of Titan and performed limb scans. As the spacecraft departs from Titan, the Doppler speed is increasing furthermore, hence HDAC was absorbing again radiation in the line wings (now bluewards of the emitted line). Still visible is a small signal exceed of about 10 cts s^{-1} at the end of the encounter.

The HDAC measurement thus provides information not only about the Lyman-α line strength across Titan's disc but also on the line shape. For future flybys it would be therefore desirable to observe Titan under different observing conditions in order to determine e.g. the line center Lyman-α line strength of the day side of Titan, which could be achieved when the closest approach coordinates are located above the sunlit hemisphere of Titan.

The following chapters of this work will focus on the simulation of the HDAC measurement during the T_9 flyby. Due to the unknown amount of deuterium in the absorption cell, this work takes only into account the measurements performed in photometer mode and using the H cell. The signal when both absorption cells were operated is not considered. In chapter 9 the difference signal of the measurements will be compared to radiative transfer model calculations and thus the exospheric parameters will be determined.

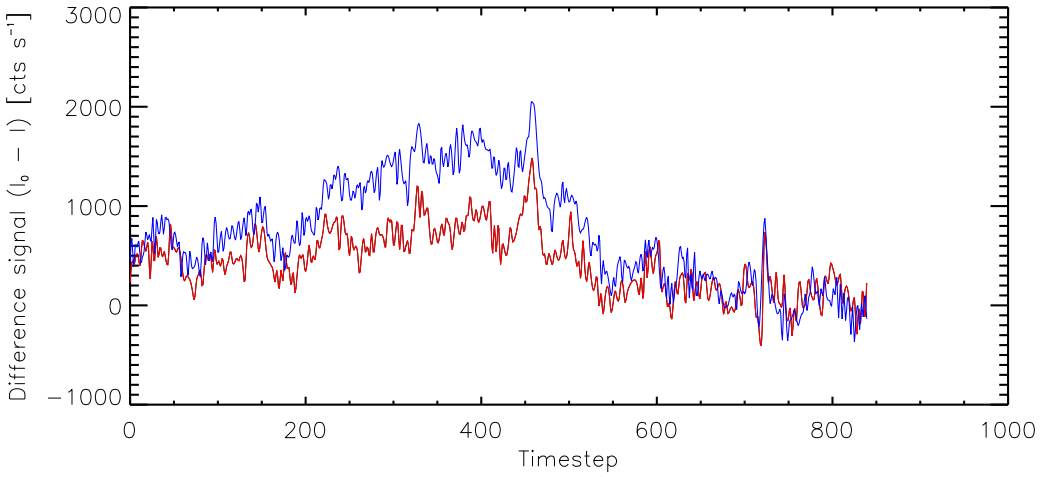

Fig. 4.9: Difference signals between measurements performed in photometer mode (I_0) and cell on measurements (I). The red line shows the difference signal using the H cell measurements, whereas the blue line shows the difference signal using the measurements where both cells were switched on. A spline fit has been applied to all data sets in order to adjust for the different number of data points. The signal is very noisy and shows strong peaks caused by undersampling.

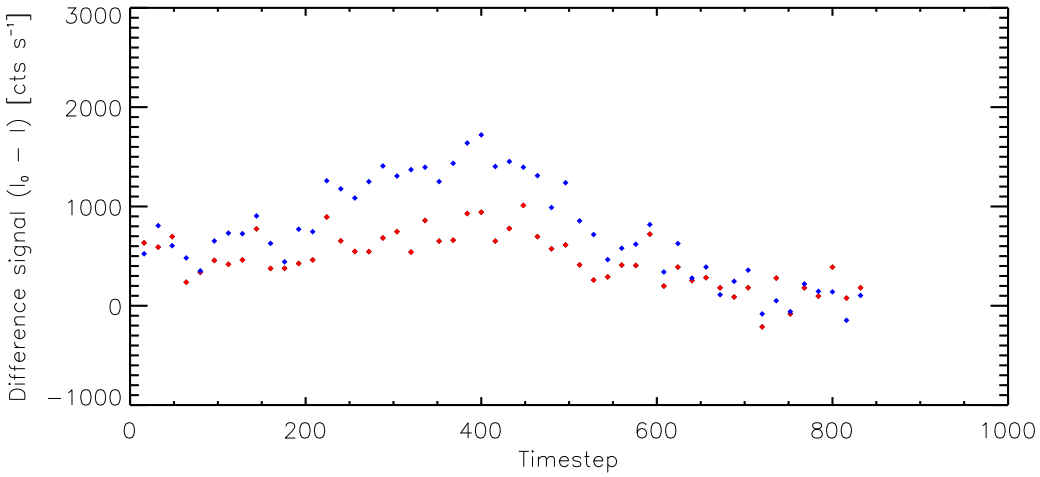

Fig. 4.10: Difference signals between measurements in photometer mode (I_0) and cell on measurements (I) after reprocessing, as described in the text. The red diamonds show the difference signal using only the H cell measurements, whereas the blue diamonds show the difference signal using both cells.

5. EXOSPHERIC DENSITY DISTRIBUTION MODELS

Direct measurements of densities in the atmosphere of Titan are limited to altitudes below 2,000 km. Especially in the upper atmosphere only the heavier species can be measured, like nitrogen and methane. Lighter species, such as molecular and atomic hydrogen, are inferred from appropriate fitting of the distributions of the heavier species and by photochemical models. Hence, there exist no direct measurement of the atomic hydrogen distribution in the atmosphere of Titan. Upper atmospheric atomic hydrogen density distributions inferred from photochemical models are limited to altitudes below about 1,500 km (see review of articles in section 2.4.2). The investigation of the radiative transfer in Titan's exosphere therefore requires the development of an exospheric density distribution model, so as to evaluate the altitude density profile. Above the exobase, where the hydrogen atoms no longer follow a Maxwellian distribution of velocities (since collisions are negligible), two different exospheric models are applied, briefly described in the following sections.

5.1 Chamberlain model

As a first approach an exospheric model by Chamberlain (1963) (furthermore referred to as the "Chamberlain model") is applied to Titan's exosphere, which has been developed for Earth's atmosphere and verified by Lyman-α observations from the DE1 satellite (Rairden et al., 1986).

The Chamberlain model takes into account neutral particles whose orbits are controlled only by gravity. It assumes spherical symmetry and requires the altitude and temperature of the exobase. The spatial and momentum distribution above this critical level is governed by Liouville's equation (see chapter B in the Appendix for an introduction into the Liouville theorem).

The Liouville theorem states that the density in phase space remains constant along a dynamical trajectory. Any particle in the exosphere naturally falls into one of four categories, based on orbital characteristics, i.e., ballistic, bound, escaping, and incoming hyperbolic particles (see Figure 5.1). At any given point in the exosphere, each of the above types occupies an isolated

region in the phase space.
Ballistic and escaping particles intersect the exobase, with velocities either smaller or greater than the escape velocity. These two categories represent particles which are directly injected from the thermosphere. On the other hand, particles in bound (satellite) orbits have perigees above the exobase, and therefore have a purely exospheric origin. The existence of bound orbits depends on the balance of the rare collisions that do occur within the exosphere with the rare destructive processes, such as photo-ionization. Because in any collision-less model there is no mechanism to establish a steady-state population of bound particles, this category is excluded from the density calculations. Incoming particles on hyperbolic orbits are also excluded since they obviously require an external origin.

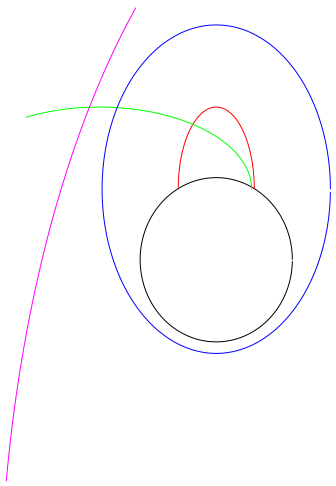

Fig. 5.1: Particle orbits populating the exosphere. The black circle represents Titan's exobase. The red line indicates the trajectory of a ballistic particle, the green line an escaping particle, the blue line a bound orbit and the violet line a hyperbolic orbit.

Assuming a Maxwellian distribution of velocities $f(v)$ at the exobase and applying Liouville's theorem, implies that the velocity distribution function above the exobase is also Maxwellian, truncated to include only regions in the momentum space occupied by either ballistic or escaping particles with trajectories intersecting the exobase. Particle densities can be directly calculated by integrating over the appropriate regions of the momentum space at any height yielding the distribution of density throughout the exosphere:

$$N(r) = n_c \exp^{-(\lambda_c - \lambda(r))} \zeta(\lambda(r)), \tag{5.1}$$

where n_c is the density at the critical level r_c (i.e. the exobase). λ is the

potential energy in units of $k_B T$:

$$\lambda(r) \equiv \frac{GMm}{k_B T_c r}, \tag{5.2}$$

where M is the mass of Titan, m is the particle's mass and T_c the temperature at the exobase, whereas λ_c is the energy at the exobase level r_c.
The right hand side of equation 5.1 represents the hydrostatic equation multiplied by ζ, a partition function, which describes the orbits of the particles released at the exobase, with $\zeta = \zeta_{\rm bal} + \zeta_{\rm esc}$ (see below). At the exobase the partition function is unity. Above the exobase the density departs from the barometric law only as orbits in certain directions and energy ranges become depleted.

The partition function for ballistic orbits is given by

$$\zeta_{\rm bal} = \frac{2}{\pi^{1/2}} \left[\gamma\left(\frac{3}{2}, \lambda\right) - \frac{\left(\lambda_c^2 - \lambda^2\right)^{1/2}}{\lambda_c} \mathrm{e}^{-\Psi_1} \cdot \gamma\left(\frac{3}{2}, \lambda - \Psi_1\right) \right], \tag{5.3}$$

where

$$\Psi_1 = \frac{\lambda^2}{\lambda + \lambda_c} \tag{5.4}$$

and γ is the incomplete gamma function function:

$$\gamma(\alpha, x) = \int_0^x y^{\alpha-1} \mathrm{e}^{-y} \mathrm{d}y. \tag{5.5}$$

Escaping orbits are parameterized as:

$$\zeta_{\rm esc} = \frac{1}{\pi^{1/2}} \left\{ \Gamma\left(\frac{3}{2}\right) - \gamma\left(\frac{3}{2}, \lambda\right) - \frac{\left(\lambda_c^2 - \lambda^2\right)^{1/2}}{\lambda_c} \mathrm{e}^{-\Psi_1} \left[\Gamma\left(\frac{3}{2}\right) - \gamma\left(\frac{3}{2}, \lambda - \Psi_1\right) \right] \right\}, \tag{5.6}$$

where $\Gamma(\alpha) = \gamma(\alpha, \infty)$ is the complete gamma function. See Chamberlain (1963) for a detailed derivation of the partition functions used above.
The principle of the Chamberlain formalism does not take into account the particles coming into the atmosphere from infinity. These constitute the fourth possible type of population, which must be as important as the escaping population to maintain a hydrostatic equilibrium. Disregarding the population of entering particles from the infinity, Garnier et al. (2007) found a discontinuity of about 20% for the H density at the exobase: below the exobase hydrostatic equilibrium is maintained, with Maxwellian distributions of velocities, and above without the population of entering particles from the infinity.

5.2 Particle model

As another approach, a dynamic particle model from Wurz and Lammer (2003) is applied (furthermore referred to as the "Particle model"), which has been applied to Mercury's exosphere in order to derive the atomic hydrogen exobase density using measurements performed by Mariner 10, as well as on Mars's exosphere using the ASPERA-3 instrument aboard Mars Express (Galli et al., 2006). Using the Monte Carlo method and assuming angular and velocity distributions at the exobase in three dimensions (as prescribed by the release process), it follows the individual trajectories of particles released from the exobase through the exosphere until the particles cross the exobase layer again or cross the upper model boundary.
In this work, only thermal particle release is considered, hence particles are released from the exobase from a Maxwellian distribution of velocities. Other escape mechanisms, like photo-ionization and charge exchange were found to be insignificant compared to thermal escape (cf. section 2.3.2). A particle falling back to the exobase level is considered lost. In the model no assumptions are made for the exosphere itself, for example barometric scaling or non-barometric scaling; everything follows from the trajectory calculations. Trajectory modifications due to radiation pressure are not considered in the model (see chapter C in the Appendix).
McDonough and Brice (1973) first proposed the possibility that particles escaping from Titan may be captured by Saturn's strong gravitational field and form into a toroidal cloud near Titan's orbit (see also Smyth 1981; Hilton and Hunten 1988). Molecules with trajectories reaching above the Hill sphere (roughly at 20 Titan radii) are able to escape from the satellite, since these particles would be progressively perturbed by Saturn's gravity and eventually end up orbiting either the planet or the satellite. The exospheric model extends to only 12 Titan radii, hence this effect is also not taken into account.

In order to determine the velocities of the exospheric particles, the velocity distribution at the exobase is created using Gaussian deviates. A set of three Gaussian deviates is needed to determine the components of a velocity vector for the thermal particle release at the exobase. The Gaussian deviates, denoted G_i, are calculated by using the relation given in Zelen and Severo (1965) and Hodges (1973):

$$G_i = [-2\ln(p_i)]^{1/2}\cos(2\pi q_i), \tag{5.7}$$

where p_i and q_i are uniform deviates between 0 and 1. The variance of each Gaussian deviate is σ_i^2=1 (for i = 1, 2, 3). The initial velocity vector, $\mathbf{v}_0$ =

(v_x, v_y, v_z), at the start of the particle trajectory is

$$\mathbf{v_0} = \left(\frac{m}{k_B T_c}\right)^{1/2} \mathbf{G} + \mathbf{r} \times \mathbf{\Omega} \tag{5.8}$$

with particle mass m, the Boltzmann constant k_B, T_c the exobase temperature, r the release location on the exobase, and Ω the rotational velocity of Titan.
The particles released from Titan's exobase are moving mainly on ballistic trajectories. The elevation angle α_j can be calculated from the particle velocity $\mathbf{v}_j$ and the vertical velocity component v_{zj} (with j=0,...,n), and n the number of altitude steps considered in the simulation):

$$\alpha_j = \arcsin\left(\frac{v_{zj}}{(\mathbf{v}_j \cdot \mathbf{v}_j)^{1/2}}\right) \tag{5.9}$$

where $v_{z,j}$ is the velocity component in z-direction, pointing away from the planetary surface and α_0 is the ejection angle.
The flight time t_j for a particle traveling an altitude step of Δz can be calculated assuming straight paths for one altitude step:

$$t_j = \frac{v_j \sin(\alpha_j)}{g(r)} - \sqrt{\left[\frac{v_j \sin(\alpha_j)}{g(r)}\right]^2 - \left(\frac{2\Delta z}{g(r)}\right)} \tag{5.10}$$

where g is Titan's gravitational acceleration as a function of planetocentric distance r. After knowing the flight time for an altitude step the new $v_{z,j+1}$,$\mathbf{v}_{j+1}$, and α_{j+1} corresponding to the new altitude z_{j+1} is calculated.

The density profile of species k can be finally calculated via the height dependent density

$$n_k(r) = \tilde{n}\left(\frac{R_{Exo}}{r}\right)^2 \sum_j t_j \tag{5.11}$$

where the sum extends over all particles j that cross the layer located at height $r = R_M + k\Delta z$ The scaling factor $\tilde{n}$ is established either by prescribing a column density or an exobase density that has to reproduced by $n_k(r)$
.

5.3 Application to this work

In the radiative transfer model described in the following chapter two particle species are considered: atomic hydrogen is treated as the resonance scattering species of Lyman-α radiation, whereas methane is treated as an absorber

absorbing Lyman-α photons (being photo-dissociated). At the lower model boundary (780 km) it is assumed that the whole solar Lyman-α radiation has been absorbed by methane.
For the distribution of atomic hydrogen in the upper atmosphere from 780 km up to the exobase (which is in the exospheric model located at 1,500 km) model data obtained from Yung et al. (1984) is used. The distribution of atomic hydrogen above this level up to the upper model boundary is calculated by the afore mentioned models.
The methane profile used in the radiative transfer model is taken from INMS data from de La Haye et al. (2008) in the altitude range from 780 km to 2,000 km. The distribution of the methane number density up to the upper model boundary at an altitude of 30,000 km has been extrapolated (see Figure 5.2).

5.4 Density distribution calculations

Note that the Chamberlain model density profile has been calculated in the context of this work, whereas the density distribution of the Particle model has been provided by the authors of the model.

Using the Particle model, a statistically meaningful quantity of hydrogen atoms and methane molecules are released from the exobase with an ejection angle randomly equally chosen within $(0,\pi)$. Below the exobase the particle velocities obeys the Maxwell-Boltzmann-distribution of velocities, hence there will be no preferred direction. Above the exobase, the distribution of velocities is asymmetric since in the exosphere collisions become negligible.

Comparison with calculations performed using the Chamberlain model with a fixed exobase temperature of $T = 150\,\mathrm{K}$ and an exobase density of $n_\mathrm{H} = 1 \cdot 10^4\,\mathrm{cm}^{-3}$ (as shown in figure 5.2) yields higher densities in the upper exosphere for the Chamberlain model; the density decreases much faster using the Particle model. At the exobase the Chamberlain model shows a strong change of the density gradient: below the exobase the density decreases strongly with increasing altitude and above the decrease it is much slower. This is also observed when using the Particle model, however, the transition is much smoother. The different density gradients below and above the exobase occur since below the exobase hydrostatic equilibrium is maintained, whereas above particle are flowing away from Titan.
Using the Particle model, the timescales for hydrogen atoms released at the

exobase can be determined until they reach an exobase altitude of 30,000 km, being about $t_{\mathrm{Th}} = 2{\cdot}10^4$ s (see Figure 5.3). Thus, the characteristic time scale for thermal escape is much lower than that for non-thermal escape mechanisms, like photo-ionization ($t_{\mathrm{Ion}} = (1-2)\cdot 10^9$ s, Smyth 1981) or charge exchange ($t_{\mathrm{CE}} \approx 3\cdot 10^7$ s; Wolfe et al. 1980; Smyth 1981). Omitting these processes in the calculations is hence justified.

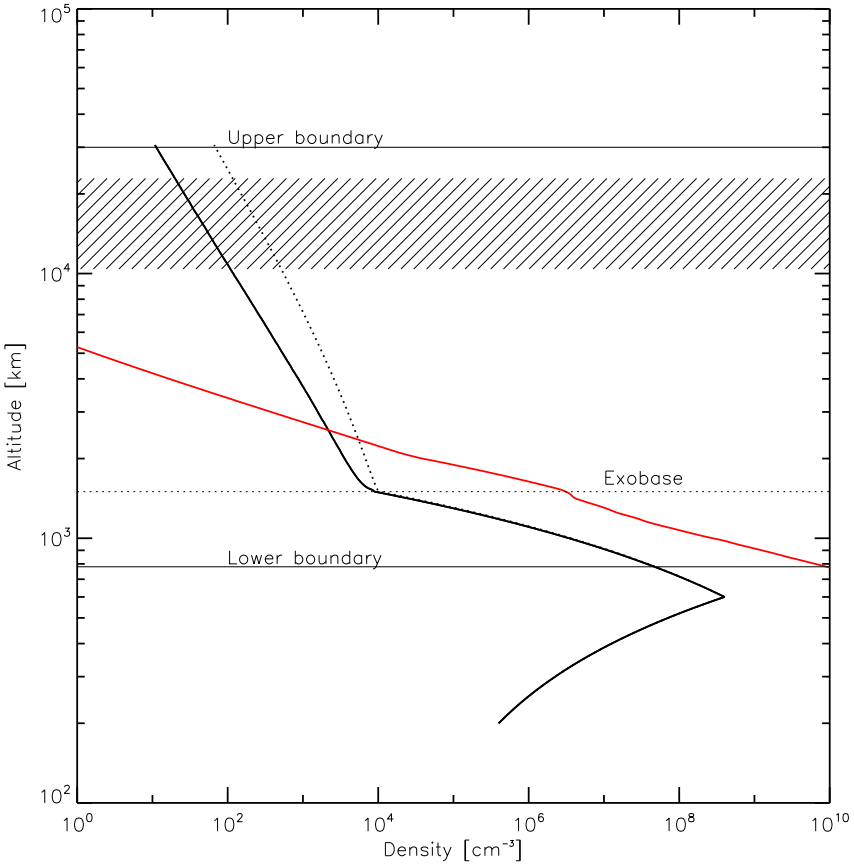

Fig. 5.2: Density profiles used in this work. The plot is showing the density distribution of atomic hydrogen, calculated by the Particle model (solid black line) and compared to the Chamberlain model (dotted black line). The atomic hydrogen exobase density chosen for both models was $n_H = 1\cdot 10^4\, cm^{-3}$, whereas the exobase temperature chosen was $T_c = 150\, K$. Additionally the methane density distribution is shown (red line). The shaded area indicates the altitude range of HDAC during the T_9 flyby.

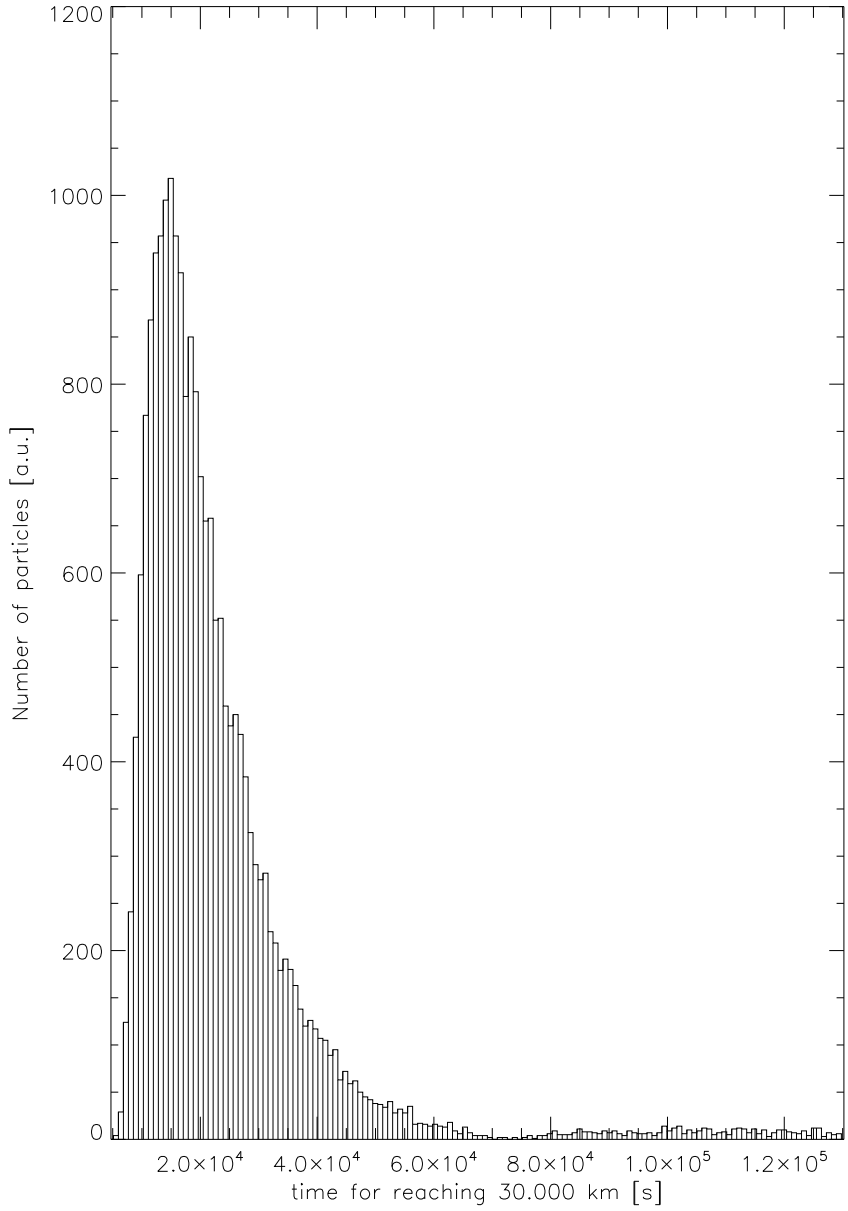

Fig. 5.3: Time scales for H atoms released from the exobase to reach an exospheric altitude of 30,000 km. Image credit: A. Schaufelberger (priv. com.).

6. RADIATIVE TRANSFER MODEL DESCRIPTION

In this chapter a detailed description of the radiative transfer model to calculate the transfer of Lyman-α radiation within Titan's exosphere is given. The description also includes the simulation of the measurement performed by HDAC. Since HDAC is moving with time during the encounter, the radiative transfer calculations are split into two parts. The first part considers the transfer of radiation within the exosphere, and the second part then takes into account the amount of radiation scattered into the instrument at certain spacecraft positions during the encounter. The second part is hereafter referred to as the "Data Sampling model". However in this work the entire radiative transfer model (including both parts) will be referred to as the "Monte Carlo radiative transfer model".

For the radiative transfer calculations performed here, the Monte Carlo method is used (as introduced in chapter 3) in order to easily solve the radiative transfer for multiple scattering. Especially in the lower exosphere, where the density is high compared to the outer regions, photons might be multiply scattered.

As this work focuses on the simulating of measurements performed by the HDAC instrument (described in chapter 4), the radiative transfer of solar Lyman-α radiation under changing observing angles must be taken into account. Using the first part of the Monte Carlo radiative transfer model, the scattering and absorption positions within the model exosphere are determined. Afterwards the Data Sampling model is applied to the output of the radiative transfer calculations in order to investigate the quantity of radiation scattered into the instrument during the flyby. See Appendix E for flow charts of the radiative transfer model part which calculates the distribution of scattering points (Figure E.1), as well as for the Data Sampling model, which simulates the flyby of HDAC (Figure E.2).

A certain number of Lyman-α photons is traced from the point of emission (or at the beginning from the source) to the point of absorption (or the point, where the photon leaves the model without any interaction). Random numbers are applied in determining the position and the wavelength of photons

started at the upper model boundary, the scattering angle, the path lengths between interactions and in the angle-dependent emission wavelength generation after scattering.

6.1 General assumptions

In the exospheric model atomic hydrogen acts as the scattering medium and methane as the absorber medium. The scattering medium is assumed to consist of only two-level atoms. Furthermore it is assumed that the particle velocities obey the Maxwell-Boltzmann distribution of speeds.
Note that the assumption of a Maxwellian distribution of velocities is per definition not valid in the thin layers of the exosphere. E.g. Thomas (1963) have investigated the effect on the absorption cross section and found from detailed modeling of Öpik and Singer (1961) that there will be a deficiency of low-velocity components along the radial direction and a deficiency of high-velocity components along the tangential direction. The absorption cross section, therefore, is anisotropic: a uniform beam of radiation in the radial direction is absorbed (relative to the Doppler absorption) less in the center of the line than in the wings. On the other hand, a similar beam in a perpendicular direction is absorbed less in the wings than in the center of the line, again relative to the Doppler width.
Nevertheless one can assume in a first order approximation that in a certain range above the exobase the velocity distribution is close to being Maxwellian, hence a "single exospheric temperature" may be defined, as is used e.g. for the calculation of Doppler widths (equation 3.23). The assumption of a Maxwellian distribution of velocities throughout the exosphere furthermore allows a simple treatment of the scattering process, as will be shown below. See the next section 6.1.1 for a detailed discussion of this assumption.

The scattering is assumed to be isotropic. This assumption holds for atomic hydrogen as long as it is not treated relativistic. Polarization of the scattered radiation is ignored. Photons are lost either by escape through the upper or lower model boundaries or via absorption by methane molecules. The Sun is treated as the only source of photons, which are released from the sunlit hemisphere of Titan at the upper model boundary. Other photon sources, like the interstellar medium and Saturn are excluded.

The x-axis is defined as the axis connecting Titan's center and the Sun's position via the subsolar point on Titan's exobase. The y- and z-axis is

chosen to be perpendicular, spanning a right handed coordinate system. The orientation of both the y- and z-axis is chosen arbitrarily and is not aligned with e.g. the spin axis of Titan. See figure 6.1 for the coordinate system used in this work.

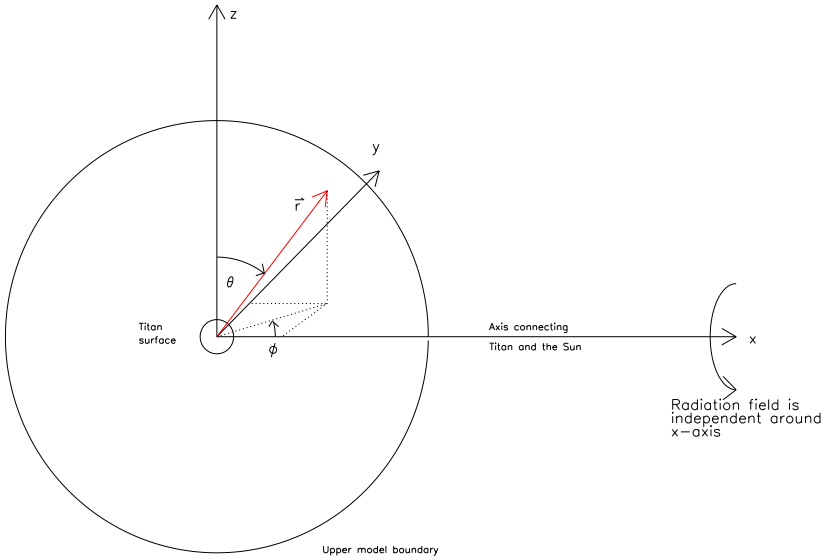

Fig. 6.1: Coordinate system used in this work: Titan is centered at x=y=z=0. The x-axis is pointing towards the sun and the y and z axes are chosen to be perpendicular, spanning a right handed coordinate system

The rotation of Titan is not considered within the radiative transfer model. The rotational velocity of Titan is given by

$$\Omega = \omega \cdot r_{\mathrm{Exo}} = 18.58\,\mathrm{m\,s^{-1}} \tag{6.1}$$

with $\omega = 4.56 \cdot 10^{-6}\,\mathrm{rad\,s^{-1}}$ and $r_{\mathrm{Exo}} = 4,075\,\mathrm{km}$ being Titan's rotation rate and exobase altitude, respectively. The most probable velocity at the exobase using a temperature of 150 K is v_{p}=1573.56 $\mathrm{m\,s^{-1}}$, hence much larger compared to the rotational velocity.

Photons coming from the Sun are assumed due to its large distance to enter the model in a parallel beam, being perpendicular to the y-z-plane. Hence the transfer of photons in the model exosphere is axially symmetric along the x-axis. At the end of the calculation this symmetry is used to mirror the scattering coordinates on the (a) x-y-plane, (b) x-z-plane and (c) x-y- and x-z-plane subsequently. All other quantities describing the scattering position remain unchanged.
In the radiative transfer model using the Monte Carlo method, single photons leaving the source in a given direction represent a large set of N actual

particles. Since a number fraction of N_i photons will be absorbed on the way to the detector within the model, the photon parameter $W = N_i/N$, called its weight, is introduced which is initially unity at the source. Within the Monte Carlo radiative transfer model the weight of the photons does not change, since the scattering process is calculated randomly. In order to check the statistical significance for a given amount of photons that are considered in the calculations, section 7.1 investigates the response of the signal with different amounts of photons.

In the Data Sampling model described in section 6.3, the "splitting" technique (Hammersley and Handscomb, 1964) is applied in order to force photons to be scattered into the direction of the detector. In order to compensate this forced direction, the weight of the photon need to be corrected so as not to change the physics of event. In the problem considered in this work, the detector (HDAC) is moving with time, hence the "splitting" technique cannot be applied within the Monte Carlo calculations described here. However, the technique is applied afterwards to the whole Monte Carlo output for every spacecraft position during the flyby within the Data Sampling model described in section 6.3.

6.1.1 Discussion

At this point one might thus argue about the assumption of an isothermal exosphere with particles obeying the Maxwell-Boltzmann distribution of speeds.
Particles are released from the exobase with a Maxwellian distribution of velocities. Depending on the release angle and the velocity of a single particle, it will either fall back to the exobase (if its velocity is lower than the escape velocity of Titan) or it will escape from Titan. In the case of a ballistic orbit, the particle velocity will first decrease, being zero at the apex of its trajectory and then increase. For an escaping particle, the velocity will decrease with altitude due to the gravitational deceleration.
Considering the average velocity distribution at a given height for a huge amount of particles released in different directions with different velocities, ballistic orbits will dominate the velocity distribution in the lower exosphere. With increasing altitude, ballistic orbits become depleted. Also the low velocity component of the distribution becomes depleted. Furthermore, the maximum of the distribution will shift to lower velocities. At high altitudes above the exobase only high velocity particles on nearly radial trajectories can be found, with the maximum of the velocity distribution shifted to lower

velocities furthermore.

Since the particles do not collide with each other, the exosphere is not in thermodynamic equilibrium. Strictly, no temperature can be defined because the velocity distribution is asymmetric: tangential velocities become depleted with increasing altitude, and only radial velocities can be found. However, one can identify the velocities of the particles with a kinetic temperature, which is now dependent on the direction.

For the radiative transfer calculations, the photon travel direction with respect to the travel direction of hydrogen atoms needs to be taken into account. For a photon traveling exactly in the direction of Titan's center, the velocity component of the hydrogen atoms is maximal. Thus, the Doppler shift and hence the optical depth can be simply calculated by using the radial velocity component. In the case of the photon being scattered, the velocity component in the scattering direction needs to be taken into account and the Doppler shift of the wavelength of the emitted photon can be determined.

For a photon tangentially flying through Titan's exosphere, the velocity component with respect to the travel direction of the photon has to be taken into account for each layer the photon crosses. If the tangential height is located at high altitudes in the exosphere, only hydrogen atoms can be found on escaping orbits. Thus, the velocity component in the photon travel direction is nearly zero since this direction is perpendicular to the escape direction of the hydrogen atoms. Hence the scattering cross section is small and the photon will only be scattered when its wavelength is close to the Lyman-α wavelength. However at lower altitudes, where ballistic orbits need to be taken into account, a non-zero velocity component in the photon's travel direction might be found.

Since the distribution of velocities in the tangential as well as in the radial direction at any height is not available for this work, radiative transfer is performed assuming that the exosphere is in thermodynamic equilibrium, hence a single temperature can be defined.

The scattering cross section is directly proportional to the velocity (or proportional to the square-root of the temperature, cf. equation 3.23). Since with increasing altitude the particle velocities decrease, this would result in a decreasing scattering cross section and the optical depth of the upper exosphere would decrease and fewer photons would be scattered in the outer layers of the exosphere. However, the amount of scattering in the outer layers is very low. Also the temperature has only a minor effect on the Lyman-α emission, as will be shown later in chapter 7. Even at much higher temper-

atures the resulting emission is affected only weakly, with the main effect visible in the line wings.
The assumption of a Maxwellian distribution of velocities and the assumption of a temperature isoprofile is thus probably justified for the context of this work, allowing for an easy treatment of the non-coherent scattering process as will be shown in section 6.2.4. However, for future measurements of HDAC with a much lower noise level, this effect needs to be treated carefully. This is however beyond the scope of this present work.

6.1.2 Model boundary conditions

In the radiative transfer model methane is treated as an absorber. The lower model boundary represents the altitude, at which methane is effectively photolyzed by Lyman-α radiation (see section 2.2.3) and hence absorbs the whole Lyman-α radiation penetrating Titan's upper atmosphere. See also Figure 6 in Krasnopolsky (2009) for an overview of solar UV absorption with height in Titan's atmosphere. The upper model boundary is chosen to be well above the altitude of the Cassini spacecraft during the T_9 flyby measurements, hence at an altitude of 30,000 km (the distance to Titan's center is 32,575 km).
The effect of radiation pressure on the hydrogen atoms is not taken into account, since radiation pressure becomes important only above 314,709 km or 122.21 R_{Titan} (see chapter C in the Appendix) which is far outside the model boundaries of this work.

6.2 Calculation procedure

Following Avery and House (1968), the basic steps in the computation, which will be described in detail below are as follows:

1. Select the direction, in which the photon is released from the source or from the scattering atom.

2. Select the wavelength, at which the photon is released or scattered.

3. Determine the distance, that the photon travels before it undergoes a subsequent interaction.

4. Store all required parameters and repeat the process until the photon escapes or is absorbed.

Note that in the following text all random numbers are denoted r_i and r_j throughout this work. They are independently chosen from a distribution equally distributed in (0,1). The random number generator is taken from Park and Miller (1988). To remove low-order serial correlations, a *Bays-Durham shuffle* is added (see Section 7.1 of Press et al. 1992).

6.2.1 Source photon generation

Initial position

The incident solar radiation is assumed to enter the model atmosphere in a parallel beam at the upper model boundary at $x > 0$ (sunlit hemisphere). Photons created uniformly distributed on a sphere with coordinates $(x, y, z) \in \mathcal{M}$, with $\mathcal{M} \in \mathbf{x}, |\mathbf{x}| = R$, and R being the upper model boundary radius, would result in an enhanced creation at the poles of the sphere. In order to solve this, the cartesian coordinates need to be transformed into spherical coordinates. Instead of choosing three uniformly distributed random variables $A_i \in (0,1), B_i \in (0,1), C_i \in (0,1)$ in cartesian coordinates (x, y, z), one is looking for the distribution in spherical coordinates (R, ϕ, θ), where $\phi \in (-\pi, \pi)$, and $\theta \in (0, \pi)$. The transformation reads:

$$\begin{aligned} x_0 &= R\cos\phi\sin\theta \\ y_0 &= R\sin\phi\sin\theta \\ z_0 &= R\cos\theta, \end{aligned} \tag{6.2}$$

with R being the upper model boundary radius and $\mathbf{x}_0$ representing the initial position of the photons started in the radiative transfer model.
The standard spherical coordinates are given by

$$\phi = \pi(r_i - 1/2) \tag{6.3}$$

$$\theta = \arccos(1 - 2r_j). \tag{6.4}$$

A detailed derivation can be found in Cashwell and Everett (1959) or in the Appendix D. Note that here ϕ is chosen contrary to Cashwell and Everett (1959) ($\phi = \pi(2r_i - 1)$), since in this work, the photons are released only on the sunlit hemisphere of Titan. Using the transformation given above, the initial coordinates (x_0, y_0, z_0) are equally distributed on the sunlit upper model boundary.

Initial direction

The incident direction is chosen to point towards the anti-sunward direction:

$$\begin{aligned} k_{x,i} &= -1 \\ k_{y,i} &= 0 \qquad (6.5) \\ k_{z,i} &= 0. \end{aligned}$$

(6.6)

Initial wavelength

The solar Lyman-α profile has a width of about 1 Å and a central depression. Only this central depression is considered in this work, since the scattering cross section rapidly decreases away from the center (see eq. 3.22 and figure 3.1). The wavelength λ of the incident photons is chosen from a rectangular source distribution centered at 1215.67 Å since the profile is approximately constant close to the line center. The H cell of HDAC absorbs Lyman-α radiation from 1215.6509 Å at the beginning of the observations (Doppler velocity of -4.7 km/s) to 1215.6900 Å at the end (Doppler velocity of 4.94 km/s). Hence, HDAC scans over the Lyman-α radiation from Titan with a total width of 0.0391 Å, or 4.333 units of Doppler width (with a cell temperature of 300 K, $\Delta\lambda_D = 9.024 \cdot 10^{-13}$ m, see equation 3.23). The width of the distribution function is hence chosen to be five times the Doppler width at the respective temperature (this amounts to a width of 0.0451 Å). The photons are created with a random wavelength lying within this range:

$$\lambda = \lambda_0 + 5 \cdot \Delta\lambda_D(300\mathrm{K}) \cdot (r_i - 0.5) \qquad (6.7)$$

6.2.2 Tracing procedure

Knowing the direction of a photon from its starting point $\mathbf{x}_\mathrm{S}$ (either the point of insertion or the last scattering point), a given photon suffers an interaction (either scattering or absorption) after traveling a random optical distance

$$l_r(\lambda) = -l_0(\lambda)\ln(r_i), \qquad (6.8)$$

where $l_0(\lambda)$ is the wavelength dependent local mean free photon path,

$$l_0(\lambda) = \frac{1}{n(r) \cdot \sigma(\lambda)}, \qquad (6.9)$$

with $n(r)$ being the radius dependent number density and σ the cross section of the medium (Cashwell and Everett, 1959; Avery and House, 1968; House and Avery, 1969; Hansen and Travis, 1974).

In the spherical model of this work, the photons cross different density layers

along their path, hence l_r is calculated for each layer the particular photon crosses on its way from the last scattering point/inital point on its path. The path is a sequence of distances L_i (i=1,...,n) towards the next layer on the path, with $L_1 = \mathbf{x}_1 - \mathbf{x}_0$ and $L_\mathrm{n} = \mathbf{x}_\mathrm{n} - \mathbf{x}_{n-1}$ ($\mathbf{x}_0 = (x_0, y_0, z_0)$ and $\mathbf{x}_\mathrm{n} = (x_n, y_n, z_n)$: model boundary). The total distance from the injection point to the model boundary at the end is $L = \sum_i L_i$. The density within a layer is assumed to be homogeneous. The total mean free path is given by

$$l_0(\lambda) = \frac{1}{n_\mathrm{H}(r) \cdot \sigma_\mathrm{H}(\lambda) + n_{\mathrm{CH_4}}(r) \cdot \sigma_{\mathrm{CH_4}}}, \tag{6.10}$$

with $n_\mathrm{H}(r)$ and $n_{\mathrm{CH_4}}(r)$ being the atomic hydrogen and methane number density at a radius r of the current layer the photon crosses on its path, $\sigma_\mathrm{H}(\lambda)$ being the wavelength-dependent resonant scattering cross section of atomic hydrogen and $\sigma_{\mathrm{CH_4}}$ the wavelength and temperature independent photodissociation cross section of methane (see section 3.4). For every layer crossed, l_r is then compared to the distance L_i between two consecutive grid points along the path.

The following cases are considered:

- If $l_r(\lambda) < L_i$ is fulfilled for a certain layer i, the distance d from the last scattering point or insertion point to the current scattering point is calculated, and the exact position in the exosphere is determined from

$$\begin{aligned} x' &= x_0 + k_x \cdot d \\ y' &= y_0 + k_y \cdot d, \\ z' &= z_0 + k_z \cdot d \end{aligned} \tag{6.11}$$

  It is necessary to determine the nature of the interaction, since the photon may be either scattered by an hydrogen atom or destroyed by absorption of a methane molecule. The photon's destiny is determined by the scattering albedo ϖ which is the probability that the photon is scattered.

$$\varpi = \frac{n_\mathrm{H}(r)\sigma_\mathrm{H}(\lambda)}{n_\mathrm{H}(r)\sigma_\mathrm{H}(\lambda) + n_{\mathrm{CH_4}}(r)\sigma_{\mathrm{CH_4}}}. \tag{6.12}$$

  A random number $r_i \in (0, 1)$ is chosen and compared to ϖ. If $r_i < \varpi$, the photon is scattered. Otherwise, it is absorbed and a new photon is released from the source.

- If $l_r > L_i$ applies for all layers crossed, the photon is assumed to leave the exosphere without being scattered or absorbed. Hence, the photon is no longer considered in the calculations and a new photon is released from the source.

6.2.3 New scattering direction

The new direction of the photon after scattering is assumed to be isotropic, hence can be calculated by

$$\begin{aligned} k'_x &= \cos\tilde{\phi}\sin\theta \\ k'_y &= \sin\tilde{\phi}\sin\theta, \\ k'_z &= \cos\theta \end{aligned} \tag{6.13}$$

with the spherical coordinates being $\theta = \arccos(2r_i - 1)$ and $\tilde{\phi} = \pi(2r_j - 1)$. Note here, that $\tilde{\phi}$ has been chosen different to ϕ in equation 6.3.
The scattering angle α is determined by the scalar product between the photon's incoming direction $\mathbf{k}$ and the scattering direction $\mathbf{k}'$:

$$\alpha = \arccos\left(\mathbf{k} \cdot \mathbf{k}'\right) \tag{6.14}$$

The scattering phase angle γ is given by

$$\gamma = \pi - \alpha. \tag{6.15}$$

$\gamma = 0°$ is equivalent to forward scattering and $\gamma = 180°$ to backward scattering.

6.2.4 Generation of emission wavelength

In order to determine the wavelength of the scattered photon, it is very important to choose an appropriate redistribution function. In the rest frame of the atom, in the case of coherent scattering, there is no wavelength shift before and after the scattering. This case applies for atmospheres with low densities, where collisions are negligible. When the excited atom undergoes collisions with other atoms, the emitted photon will have a different energy than the incident photon. This case is called non-coherent or complete frequency redistribution (CFR).
In the external frame, however, the wavelength of the scattered photons is redistributed due to the Doppler effect, even if the scattering process is coherent in the rest frame of the atom. The wavelength of the scattered photon is hence independent of the wavelength prior to the scattering and it will be furthermore referred to as partial frequency redistribution (PFR), which has been extensively used by Lee (1977); Meier and Lee (1978) and Lee and Meier (1980) after it was introduced by Avery and House (1968), who have investigated the scattering process for the case of CFR and PFR in detail.

In the case of the low densities in Titan's exosphere considered here, collisions of excited atoms can be neglected and hence coherence in the atom's rest frame be assumed. For the exospheric temperatures considered here, the Doppler broadening needs to be taken into account. Therefore, the angle-dependent PFR function from Hummer (1962) (case II in his paper) is used. It was at first derived by Henyey (1940) and presented in a recast form by Hummer (1962). Assuming a Maxwellian distribution of velocities, the redistribution function is a distribution of wavelength as a function of incident wavelength and scattering phase angle γ:

$$R_{\mathrm{II}}(d, d', \gamma) = \frac{g(\gamma)}{\sqrt{\pi}\sin\gamma} \exp\left[-\left(\frac{d-d'}{2}\csc\frac{\gamma}{2}\right)^2\right] \times \psi\left(\alpha\sec\frac{\gamma}{2}, \frac{d+d'}{2}\sec\frac{\gamma}{2}\right) \tag{6.16}$$

where d' and d are the initial and final wavelengths relative to the line center in units of Doppler width, $g(\gamma)$ is the scattering phase function, γ the aforementioned scattering phase angle and ψ is the Voigt function:

$$\psi(\alpha, \nu) = \frac{a}{\pi}\int_{-\infty}^{+\infty} \frac{\exp(-y^2)\mathrm{dy}}{(\nu-y)^2+\alpha^2} \tag{6.17}$$

α is the natural linewidth of the line in Doppler units. Since isotropic scattering is assumed, $g(\gamma) = 1/(4\pi)$ applies.

The natural linewidth $\Delta\lambda_{\mathrm{nat}}$ is calculated using Heisenberg's uncertainty relation $\Delta E \Delta t = \frac{\hbar}{2}$. Here, Δt is the lifetime of an hydrogen atom in the second level, $\Delta t = 2 \cdot 10^{-9}$s. Using $\Delta\nu_{\mathrm{nat}} = \Delta E/h$, in units of wavelength one obtains a natural linewidth of $\Delta\lambda_{\mathrm{nat}} = 1.961 \cdot 10^{-15}\,\mathrm{m}$. Hence, $\alpha = \Delta\lambda_{\mathrm{nat}}/\Delta\lambda_D = 0.003$ at $T = 150\,\mathrm{K}$.

Figure 6.2 shows for different incident wavelengths d' the distribution $R_{\mathrm{II}}(d, d', \gamma)$ of emitted wavelengths d at certain scattering phase angles γ. In the case of forward scattering (γ=0) the resulting distribution is a δ-function, i.e. there will be no wavelength shift and the scattering is coherent. Increasing the scattering phase angle, the distribution gets broader and the maximum of the distribution shifts towards the line center. At a scattering phase angle of $\gamma = 90°$, independent of the incident wavelength d', the distribution is centered at $d = 0$, i.e. most photons will be emitted in the line center. At higher scattering phase angles the distribution is furthermore shifted.

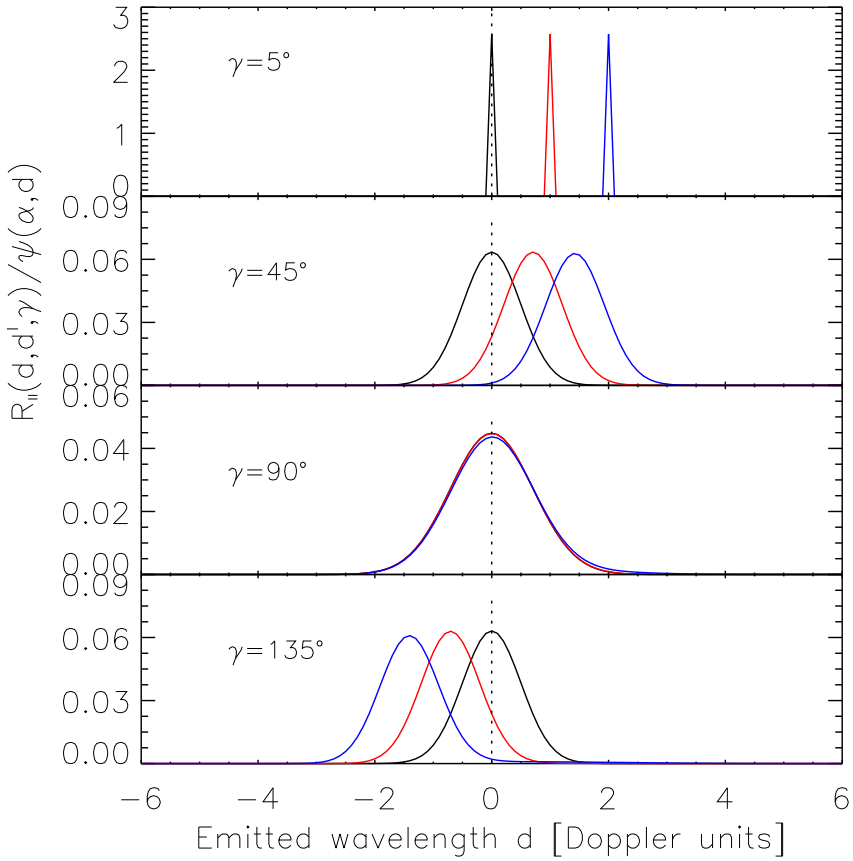

Fig. 6.2: The redistribution function R_{II} as a function of scattering phase angle γ and scaled input wavelength d'. The division by the Voigt function gives equal areas under the curves. The black line illustrates the wavelength distribution using an incident wavelength in Doppler units being zero, the red line is $d' = 1$ and the blue line is $d' = 2$.

For the calculation of emitted wavelengths, first a random wavelength in Doppler units d is calculated, being uniformly distributed in the wavelength range considered in this work. Then, $R_{\mathrm{II}}(d, d', \gamma)$ is calculated and compared with a second random number y_r uniformly chosen in (0,max(R_{II})), where max(R_{II}) denotes the maximum of the function. If $y_R < R_{\mathrm{II}}$ the emitted wavelength of the photon is set to $\lambda_{\mathrm{out}} = d \cdot \Delta\lambda + \lambda_0$. Otherwise a new set of values for d and y_r is generated.

6.2.5 *Subsequent path of the photon*

Using the new direction and wavelength of the emitted photon, the probability for the photon to be scattered or absorbed on this new path is calculated. The photon is followed until it leaves the model boundaries or is absorbed. Each photon is hence treated in a single way on its travel through the atmo-

sphere until it is absorbed or leaves the atmosphere.

6.2.6 Storage of the relevant parameters

After each scattering, the relevant parameters describing the photon are stored into an array: For each scattering point the position $\mathbf{x_S}$, the wavelength λ prior to and after the scattering, the direction of the photon prior to and after scattering ($\mathbf{k}$ and $\mathbf{k}'$), the number of scattering events N_{scat} a particular photon has suffered yet, as well as the weight W' of the scattered photon is stored. If the particular photon is being absorbed or leaves the model boundaries at the end of its way, the whole array is written to a summary file and the next photon is initiated.

6.3 Data Sampling model

6.3.1 Overview

During the flyby of Cassini the altitude and position of the orbiter changed rapidly, scanning over the whole Titan disc. In order to calculate the Lyman-α emission intensity measured by HDAC during the flyby, every scattering point within the instruments' FOV is assumed to emit a photon towards the detector. This assumption is based on the "splitting" technique described by Hammersley and Handscomb (1964): After each scattering event, the photon having weight W traveling into the new random direction $\hat{\mathbf{k}}'$ (as described by equation 6.11) is split into two, one of which travels into the direction of the detector $\hat{\mathbf{k}}'_{\mathbf{D}}$ with weight W_D, the other into the direction $\hat{\mathbf{k}}'$ with weight W'. Then the weight W of the photon before the scattering can be split: $W = W' + W_D$, where W_D is given by $W_D = W \cdot \mathcal{P}_D$ where $\mathcal{P}_D$ is the probability that the photon will be scattered to the detector. The other photon flying into direction $\mathbf{k}'$ hence continues its flight with a reduced weight of $W' = W - W_D$. This technique is applied to every scattering position in the FOV of the instrument during the flyby. Because a single photon leaving the source in a given direction represent a large set of N actual particles and the scattering point is chosen randomly, the weight W of each photon scattered in the Monte Carlo model is unity. However, using the splitting technique and forcing photons to be scattered into the detector requires to adjust the photon weights appropriately.

6.3.2 Calculation procedure

The calculation procedure is as follows:

1. Select the scattering points, that are in the FOV at a certain spacecraft position
2. Calculate the probability, that photons from this scattering point reach the detector
3. Determine the cell transmission pattern for photons propagating through the absorption cells
4. Calculate the photon detection probability
5. Consider the subsequent path of a given photon

Position of scattering point

Whether or not a scattering point is positioned within the FOV of HDAC at a certain spacecraft position is controlled by calculating the angle β between the viewing direction of HDAC $\hat{\mathbf{k}}_{\mathrm{LOS}}$ and the unit vector connecting the spacecraft and the scattering point, $\hat{\mathbf{k}}_{\mathrm{sp}}$:

$$\beta = \arccos(\hat{\mathbf{k}}_{\mathrm{LOS}} \cdot \hat{\mathbf{k}}_{\mathrm{sp}}) \tag{6.18}$$

From the instrument description in chapter 4, a FOV diameter of 3° is obtained. Hence, if $\beta \leq 1.5°$ applies, the scattering point is within the FOV.

Transmission to the detector

Here the "splitting method" is applied:
The photon i (having weight W_i) is assumed to be scattered into the direction of the detector $\hat{\mathbf{k}}'_{\mathbf{D,i}}$. By doing this, a new wavelength for the photon needs to be calculated, depending on the new scattering angle $\alpha_{D,i} = \arccos(\hat{\mathbf{k}}_{\mathbf{i}} \cdot \hat{\mathbf{k}}'_{\mathbf{D,i}})$, with $\hat{\mathbf{k}}_{\mathbf{i}}$ being the photon travel direction before the scattering event and $\hat{\mathbf{k}}'_{\mathbf{D,i}}$ the direction from the scattering point towards the detector. The new wavelength λ is obtained by again using the redistribution function (equation 6.16). Using the new wavelength, the optical depth between scattering point and detector $\tau_{D,i}$ can be determined and the transmission $\mathcal{T}_i(\lambda)$ can be calculated:

$$\mathcal{T}_i(\lambda) = \exp(-\tau_{D,i}(\lambda)), \tag{6.19}$$

with $\tau_{D,i}$ being the optical depth for photon i between the point of scattering and the detector, including both scattering and absorption. Photons with an

optical depth of $\tau_D > 100$ are ignored, in order to exclude photons coming from scattering points lying behind Titan, as seen from the detector.
Furthermore the solid angle probability of the photon to enter the detector needs to be considered

$$P_{\Omega,i} = \frac{\omega_i}{4\pi}, \tag{6.20}$$

with the solid angle

$$\omega_i = \frac{A_{\mathrm{HDAC}}}{r^2_{\mathrm{HDAC},i}}, \tag{6.21}$$

under which the photon enters the detector, where A_{HDAC} is the area of the MgF_2 lens in front of HDAC and $r_{\mathrm{HDAC},i}$ is the distance from the scattering point to the detector.

Finally one obtains the probability $p_{D,i}$ that a photon coming from a certain scattering point within the FOV will be entering the detector:

$$p_{D,i}(\lambda_i) = P_{\Omega,i} \cdot \mathcal{T}_i(\lambda) \cdot S_{\mathrm{FOV}}, \tag{6.22}$$

with S_{FOV} being the FOV sensitivity of HDAC.

Instrument absorption pattern

Now the HDAC instrument needs to be taken into account: The photon propagates through three absorption cells, where the empty oxygen cell does not need to be taken into account. The optical depth within the hydrogen cell at the maximum filament step was determined using LISM measurements: $\tau_{\mathrm{HDAC,H}} = 0.8655$ (Regehly, 2003). Note that only the measurements are considered, where the H cell was switched on.
The spacecraft was moving with respect to Titan hence the emission line is Doppler-shifted with respect to the Lyman-α line center. The cell transmission function $\mathcal{T}_{\mathrm{HDAC}}(\lambda)$ is calculated using the cell parameters and the Doppler speed:

$$\mathcal{T}_{\mathrm{HDAC}}(\lambda) = \exp\left[-\tau_{\mathrm{HDAC,H}} \cdot \exp\left(\frac{(\lambda + z) - \lambda_0}{\Delta\lambda_{\mathrm{HDAC}}}\right)\right], \tag{6.23}$$

where z is the doppler shift $z = \lambda_0/c \cdot v_D$ with v_D being the Doppler speed and $\Delta\lambda_{\mathrm{HDAC}}$ being the doppler width:

$$\Delta\lambda_{\mathrm{HDAC}} = \frac{\lambda_0}{c}\sqrt{\frac{2k_B T_{\mathrm{HDAC}}}{m_{\mathrm{H}}}}, \tag{6.24}$$

with T_{HDAC} being the cell temperature ($T_{\mathrm{HDAC}} = 300\,\mathrm{K}$).

Photon detection probability

Finally, the detection probability $\mathcal{P}_{D,i}$ for a photon started at the upper model boundary in the Monte Carlo model is calculated, by simply multiplying all probabilities:

$$\mathcal{P}_{D,i}(\lambda) = W_i \cdot p_{D,i}(\lambda) \cdot \mathcal{T}_{\mathrm{HDAC}}(\lambda) \tag{6.25}$$

Taking the sum of $\mathcal{P}_{D,i}(\lambda)$ for all photons arriving at the detector at a certain spacecraft position $\mathbf{x}_{\mathrm{Cas}}$ yields the measured count rate:

$$n(\mathbf{x}_{\mathrm{Cas}}) = \sum_{i=0}^{j} \mathcal{P}_{D,i}(\lambda), \tag{6.26}$$

where the sum extends over all photons that are scattered within the FOV.

Subsequent path

When applying the "splitting" technique, the photon that is being scattered within the FOV, will continue its way into the direction $\mathbf{k}'$, but now with a reduced weight:

$$W_i' = W_i - \mathcal{P}_D, i. \tag{6.27}$$

This is of importance in the case, where a given photon undergoes two or more scattering events, that lie within the FOV at a given spacecraft position. The weight for the subsequent scattering is hence reduced.

6.3.3 Spacecraft trajectory

The spacecraft coordinates during the flybys were obtained using the NASA routine "SPICE". Using SPICE, one obtains the spacecraft position, velocity and viewing direction at a specific time. In order to simulate the flyby in the reference frame considered in this work, a coordinate transformation needs to be performed:

In this work the reference frame is centered at Titan's center with the x-axis pointing towards the Sun. From Spice one obtains the spacecraft coordinates and viewing direction in the so called "IAU_Titan" frame. The "IAU_Titan" frame is a body-fixed, planetocentric frame (here: Titan), with the z-axis aligned with the spin axis. The positive z-axis points toward the north side of the invariable plane of the Solar System. The invariable plane is normal to the Solar System's angular momentum vector. The x-axis defines the prime meridian, whereas the y-axis completes the right-handed frame.

Since the new x-axis is defined by the coordinates of the subsolar point on Titan's surface, SPICE is used to calculate the coordinates of the subsolar point during the flybys. By normalization one obtains a unit vector $\hat{\mathbf{e}}_x$, which

is defined as the new x-axis. Using the SPICE routine CSPICE_FRAME, a right handed orthonormal frame is calculated where all additional vectors $(\hat{\mathbf{e}}_y, \hat{\mathbf{e}}_z)$ are also normalized. Since Titan's exosphere model is symmetric along the x-axis, the y- and z-axis can be chosen arbitrarily and do not need to be aligned with e.g. the spin axis of Titan. These vectors are fed into a matrix, which rotates the "IAU_Titan" frame into the reference frame chosen in this work. The conversion is simply performed by multiplying the rotation matrix with the initial vector in the "IAU_Titan" frame. This is done with the spacecraft coordinates as well as with the instrument viewing direction.

6.4 Simulating the HDAC measurement

The radiative transfer model calculates a certain number of photons, which is statistically representative. The actual number of photons arriving at Titan is of course much larger. Hence, one must multiply the number of photons from the radiative transfer model with a factor $\mathcal{N}$ in order to compare the simulated signal with the HDAC measurements. In other words, a single photon in the Monte Carlo radiative transfer calculations represents $\mathcal{N}$ real photons.

In the radiative transfer model the scattering of a statistical relevant number of N_{Model} photons is treated, started at the uppermost layer of the sunlit side of the model exosphere. From SORCE a spectral irradiance at the position of Earth at Lyman-α $I_{tot,\oplus} = 6.5 \cdot 10^{-7}\,\text{J}\,\text{cm}^{-2}\,\text{s}^{-1}$ can be retrieved during the flyby date. See figure 6.3 for the time variability of the spectral irradiance of solar Lyman-α radiation from May 2003 to June 2009.
With the energy of a Lyman-α photon $E_{\text{Ly}\alpha} = 1.63 \cdot 10^{-18}\,\text{J}$, one obtains a total Lyman-α photon irradiance of $F_{\text{total}} = 3.98 \cdot 10^{11}\,\text{ph}\,\text{cm}^{-2}\,\text{s}^{-1}$ at a distance to Sun of 1 AU.
Emerich et al. (2005) found a relation between the total solar Lyman-α photon irradiance F_{total} and the line center irradiance $f_{\text{Ly}\alpha}$. With the relation

$$\frac{f_{\text{Ly}\alpha}}{10^{11}\text{s}^{-1}\text{cm}^{-2}\text{Å}^{-1}} = 0.64 \left(\frac{F_{\text{total}}}{10^{11}\text{s}^{-1}\text{cm}^{-2}} \right)^{1.21} \tag{6.28}$$

a line center photon irradiance of $f_{\text{Ly}\alpha} = 3.41 \cdot 10^{11}\,\text{ph}\,\text{cm}^{-2}\,\text{s}^{-1}\,\text{Å}^{-1}$ at 1 AU can be obtained.
At the position of Titan during the T_9 flyby (9.09 AU) this translates into $f_{\text{Ly}\alpha,\text{Titan}} = 4.13 \cdot 10^{9}\,\text{ph}\,\text{cm}^{-2}\,\text{s}^{-1}\,\text{Å}^{-1}$.

In the Monte Carlo model, photons enter the exosphere within an area

$$A = \pi \cdot R^2 = \pi \cdot (32575 \cdot 10^5 \mathrm{cm})^2 = 3.33 \cdot 10^{19} \mathrm{cm}^2, \tag{6.29}$$

with R being the radius of the upper boundary. Hence, a Lyman-α intensity of $I_{\mathrm{Titan,model}} = 1.37 \cdot 10^{29}\,\mathrm{ph\,s^{-1}\,\AA^{-1}}$ needs to be considered.
Furthermore, the wavelength range needs to be taken into account, in which the calculation has been performed. For the Monte Carlo radiative transfer calculations only a tiny part of $\Delta\lambda_{\mathrm{Ly}\alpha} = 0.0451\,\mathrm{\AA}$ of the total solar Lyman-α line (see section 6.2) is considered which in turn has a total width of $\sim$1 Å. In total, one obtains within an integration time of $t = 1\mathrm{s}$:

$$N_{\mathrm{incoming}} = I_{\mathrm{Titan,model}} \cdot \Delta\lambda_{\mathrm{Ly}\alpha} \cdot t = 6.17 \cdot 10^{27}\,\mathrm{ph}. \tag{6.30}$$

Hence, taking into account e.g. $N_{\mathrm{Model}} = 4 \cdot 10^7$ photons in the calculations, the Data Sampling results need to be multiplied by a factor of $\mathcal{N} = N_{\mathrm{incoming}}/N_{\mathrm{Model}} = 1.55 \cdot 10^{20}$ in order to compare model and measurements.

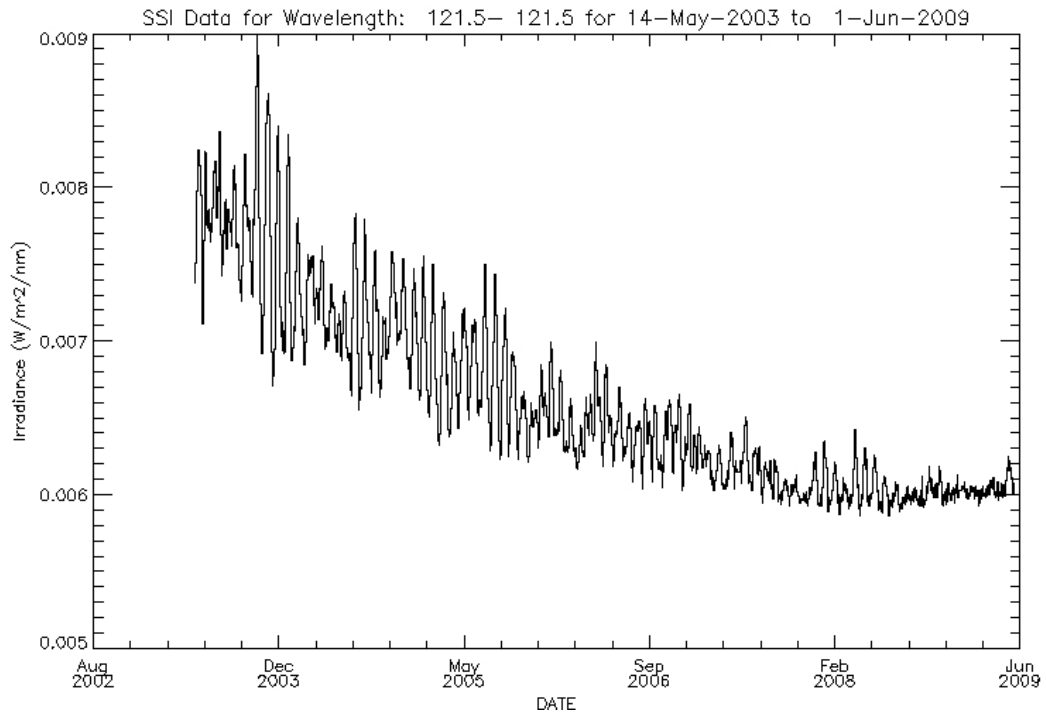

Fig. 6.3: Solar spectral irradiation time series for Lyman-α radiation from May 2003 to June 2009.
Image credits: SORCE (`http://lasp.colorado.edu/sorce`*)*

7. MONTE CARLO RADIATIVE TRANSFER CALCULATIONS

In the following section, the Monte Carlo radiative transfer calculations performed in this work will be discussed. Thereby, a parameter variation is performed in order to investigate the effects of the model input parameters as for one example fixed number of photons started on the sunlit side of the upper model boundary. Furthermore the results of the Monte Carlo radiative transfer model are reviewed for their statistical significance.
Note that in chapter 8 the Monte Carlo radiative transfer model is validated with a simple analytical model. In chapter 9 the calculations performed are compared to the measurements of HDAC during the T_9 flyby and the best fitting exospheric parameters are determined. Using these parameters, the expected signal during two future Titan flybys are calculated, where HDAC will be switched on again.

In order to determine the response of the Lyman-α emission on the model parameters considered in this work, a parameter variation is performed prior to the comparison of the calculated data with the measurements. The parameter variations include the following points:

- The Lyman-α line center photon irradiance during the T_9 flyby was $f_{\mathrm{Titan}} = 4.13 \cdot 10^9\,\mathrm{ph\,cm^{-2}\,s^{-1}\,\mathring{A}^{-1}}$. Thus, the radiative transfer model needs to treat a total number of $6.17 \cdot 10^{27}$ photons (see section 6.4). Due to limited computation capacities, only a low number of photons can be treated in the model. In order to find a statistically relevant number of photons that yield a converged result, the number of photons is varied and the statistical output of each calculation is discussed.

- Using the two exospheric density models described in chapter 5, calculations with varying atomic hydrogen number densities at the exobase are performed, which enter into both exospheric density models. The exobase number density of atomic hydrogen inferred from photochemical modeling or indirect measurements is presently uncertain within a factor of 20 (see overview in section 2.4.2). For each of the two den-

sity models, calculations are therefore performed with exobase atomic hydrogen densities in the range of literature values. Furthermore the statistical output for each calculation as well as the simulated signal during the T_9 flyby is discussed.

- The last parameter variation involves the effect of varying exospheric temperatures on the results. The temperatures are varied within the range of value suggested by de La Haye et al. (2007b). They find a temperature below 1,500 km from 147 K up to 158 K (depending on the Titan flyby considered). Above 1,500 km the inferred temperatures are in the range 149 K to 205 K from fitting the N_2 data or in the range 149 K to 223 K from fitting of the CH_4 data during the flybys. Measurements by the UVIS instrument also indicate temperatures in the range of 150–200 K (D. Shemansky, priv. com.). The temperatures are therefore varied in the range from 147 K up to 250 K and the response of the Lyman-α signal is investigated in detail.

7.1 Statistical significance and stability of the results against the number of model photons

In order to determine, which amount of photons must be treated in the radiative transfer calculations yield a converged result, the calculations are performed with $4{\cdot}10^5$ photons, $4{\cdot}10^6$ photons, $2{\cdot}10^7$ photons and $4{\cdot}10^7$ photons. For the radiative transfer calculations, an atomic hydrogen profile calculated using the Particle model with an exobase density of $8 \cdot 10^4\,\mathrm{cm}^{-3}$ as well as an exospheric temperature of 150 K is used. Five independent radiative transfer calculations are performed for each amount of photons considered.
The ratio of scattered to injected photons (f_{Scat}), as well as the fraction of single scattering events f_{SS}, i.e. the photon has been scattered only once and then either leaves the model at the upper or lower boundary or is absorbed, is shown in table 7.1. Although the number of scattered photons as well as the fraction of single scattering events does not change significantly when varying the amount of photons, it is nevertheless clearly visible, that when increasing the number of photons for the calculations the errors decrease.

Tab. 7.1: Statistics: Variation of the number of photons considered for the radiative transfer calculations. f_{Scats} denotes the ratio of scattered to injected photons, whereas f_{SS} indicates the fraction of single scattered photons.

Number of photons	f_{Scat} [%]	f_{SS} [%]
$4{\cdot}10^5$	8.267±0.052	72.179±0.494
$4{\cdot}10^6$	8.266±0.031	72.465±0.165
$2{\cdot}10^7$	8.265±0.010	72.950±0.125
$4{\cdot}10^7$	8.261±0.004	72.916±0.094

The most critical part however are the number of photons that will enter the detector, since the FOV is very narrow. The Data Sampling model is thus applied to the model output and the difference signal of calculations performed in photometer mode (both cells switched off) and calculations performed taking into account the absorption by the H cell is taken. Furthermore the median of the five independent calculations performed is used to calculate the difference signal.
Since only a minor fraction of photons are considered, that would enter Titan's exosphere in reality, the simulated signal needs to multiplied by the factor $\mathcal{N}$, which has been introduced section 6.4. The factors the signal need to be multiplied with are $\mathcal{N} = 1.55 \cdot 10^{22}$ when using $4{\cdot}10^5$ photons for the calculations, $\mathcal{N} = 1.55 \cdot 10^{21}$ for $4{\cdot}10^6$ photons, $\mathcal{N} = 3.10 \cdot 10^{20}$ for $2{\cdot}10^7$ photons and $\mathcal{N} = 1.55 \cdot 10^{20}$ for $4{\cdot}10^7$ photons.

Figure 7.1 shows the difference signal for the four different amounts of photons mentioned above. It is clearly visible, that with a very low number of $4{\cdot}10^5$ photons for the calculations the number of photons scattered into the detector is insufficient in order to determine the difference signal (blue diamonds in the figure). With an increased amount of $4{\cdot}10^6$ photons (green diamonds in the figure), the signal is much more stable, however still shows a strong noise pattern due to statistical errors. Furthermore increasing the amount of photons to $2{\cdot}10^7$ and even to $4{\cdot}10^7$ shows that the resulting signal that will be measured by the detector is converged and statistical errors are reduced.
In Figure 7.2 the error bars for calculations performed with a number of $2{\cdot}10^7$ and $4{\cdot}10^7$ photons are shown. During the flyby, the errors increase, reaching a maximum at timestep ~ 402. Here, the spacecraft was near to the closest encounter altitude, hence the number of scattering points within the FOV was reduced. Data points with a large error bar indicate statistical errors

of the computation, due to the limited number of Monte Carlo calculations. As is already visible from table 7.1, the statistical uncertainties for the lower amount of photons (shown as red error bars) are much higher compared to the calculation performed with $4{\cdot}10^7$ photons. Note that the error bars have been calculated using the median absolute deviation as the initial estimate, and then the points have been weighted using "Tukey's Biweight" (see, for example, Hoaglin et al. 1983). Note also, that in the following plots the error bars are omitted for clarity.

Henceforward, calculations are performed with a number of $4{\cdot}10^7$ photons in order to keep the computational time at a reasonable level: A single radiative transfer calculation takes about 22 hours on a 64 bit AMD Opteron dual core processor. Performing calculations with $2{\cdot}10^7$ photons decreases the computational time to about 11 hours. Hence the number of photons will not be increased any further in order to improve the statistics. However, five radiative transfer calculations for each parameter varied are performed using a computer cluster and the median value of the signal computed by the Data Sampling model is used furthermore.

In total, for each of both density distributions a set of 22 parameter combinations as input to the Monte Carlo radiative transfer model are used for the parameter variation shown in this chapter. Additionally three calculations were performed in order to check the stability of the signal, as was discussed above. As the signal of every parameter combination is determined using the median value of five independent calculations, this results in a total number of 125 independent radiative transfer calculations. In order to fit the data measured by HDAC, a much bigger set of parameters is required, thus choosing the amount of photons in a way that keeps the computational time at a reasonable level is strongly required.

The difference signal in Figure 7.1, is about $300\,\mathrm{cts\,s^{-1}}$ at the beginning of the T_9 encounter. Note that due to the Doppler speed of the instrument with respect to Titan, the H cell absorbs radiation in the wings of the Lyman-α line scattered in Titan's exosphere. Furthermore, the instrument is looking onto the sunlit hemisphere of Titan, hence the emitted radiation is very strong.

When the spacecraft was approaching Titan, the Doppler speed increased to zero and the H cell absorbed radiation in the line center of the emitted radiation. At timestep 402, the Doppler velocity was exactly zero. The Doppler shift is not necessarily zero during closest approach (hereafter denoted C/A),

as HDAC was not exactly pointing towards Titan's center. However, during C/A (timestep 439) the Doppler speed was still low ($0.9\,\mathrm{km}\,s^{-1}$).
At timestep 402, the maximum signal is about $900\,\mathrm{cts\,s^{-1}}$ (see Figure 7.1). The signal then decreased to about $50\,\mathrm{cts\,s^{-1}}$ at the end of the encounter when the Cassini orbiter was departing from Titan and the Doppler speed of the spacecraft with respect to Titan increased. Thus, the H cell absorbed radiation in the blueward line wings of the Lyman-α line emitted from the night-side of Titan.

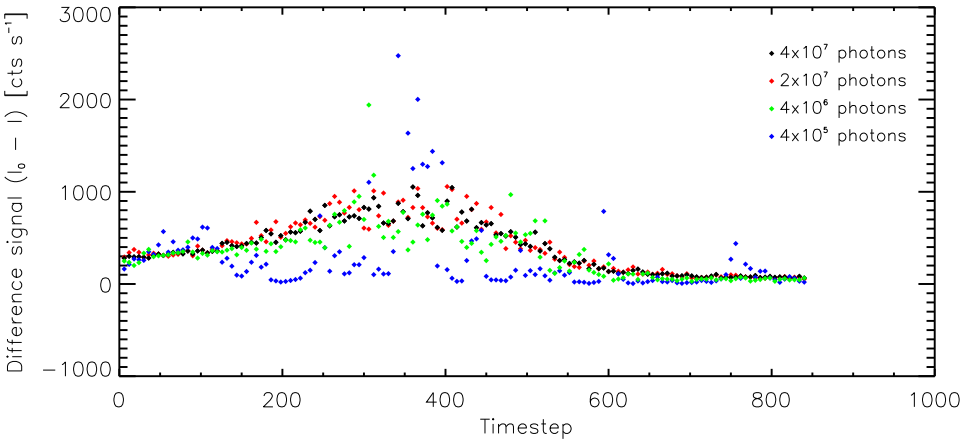

Fig. 7.1: Variation of the number of photons considered in the calculations. Difference signal of simulations performed in photometer mode (both cells off) and when the H cell was switched on during the T_9 flyby, using the Particle model with an exospheric temperature of 150 K and an exobase atomic hydrogen density of $n_{\mathrm{H}} = 8 \cdot 10^4\ cm^{-3}$.

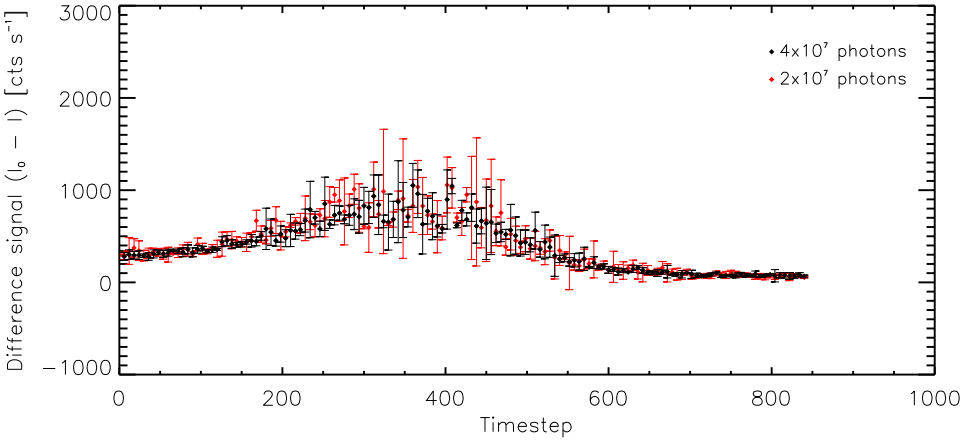

Fig. 7.2: Variation of the number of photons considered in the calculations. Same as Figure 7.1, but here only calculations performed with $2 \cdot 10^7$ and $4 \cdot 10^7$ photons are shown with the respective error bars. Data points with large error bars indicate statistical errors of the Monte Carlo method.

7.2 Hydrogen density variation

For the wide range of atomic hydrogen number densities found in the literature, calculations are performed using the exospheric models described in chapter 5. In the calculations shown here, exobase densities in the range from $n_{\mathrm{H}} = 2 \cdot 10^3\,\mathrm{cm}^{-3}$ to $n_{\mathrm{H}} = 1.0 \cdot 10^5\,\mathrm{cm}^{-3}$ cover the whole range of exobase values reported in the literature.

In Figure 7.3 the distribution of scattering points as calculated by the Monte Carlo radiative transfer model is shown for an exobase density of $n_{\mathrm{H}} = 1.0 \cdot 10^4\,\mathrm{cm}^{-3}$. The calculations are performed using an atomic hydrogen profile calculated by the Chamberlain model (left column in Figure 7.3) and by the Particle model (right column in the figure). In the following plots, the Sun is located at ($x \rightarrow \infty$,y=0,z=0), Titan is centered at x=y=z=0. Blue circles indicate Titan's surface, whereas the model boundaries are indicated by green circles. The top row shows the three-dimensional distribution of scattering positions in the model exosphere. Black dots correspond to first scattering ($n = 1$) positions, whereas red dots are positions of multiple scattering events ($n \geq 2$). For clarity, slices 200 km thick along the x-y-plane and the x-z-plane are shown. The distribution in the x-y-plane is shown in the lower row. Furthermore, Figure 7.4 shows intersecting histogram plots through Titan's disc, hence the y-axes range from -2,575 km to 2,575 km as marked by black horizontal lines in the lower plots of Figure 7.3, indicating the distribution of single and multiple scattering positions along the x-axis.

Clearly visible in both calculations is the absence of single scattering points behind Titan (when seen from Sun) - this region can only be reached by photons being multiply scattered.

Increasing the atomic hydrogen density, the number of photon scattering events increases for both exospheric density models used, as expected. Also the fraction of multiple scattering events increases. However, this increase does not follow a linear trend, as can be inferred from Figure 7.5. In the figure the effect of different density distributions is clearly visible: Black diamonds in the upper plot indicate the total fraction of photons scattered by using the Chamberlain model. Compared to the density profile using the Particle model (as indicated by red diamonds) the amount of scattering is increased simply due to the different density gradients (cf. Figure 5.2), causing more photons to be scattered. Also the density gradient is much steeper as compared to the Particle model, resulting in an increased amount

of multiple scattering events in the lower exosphere.

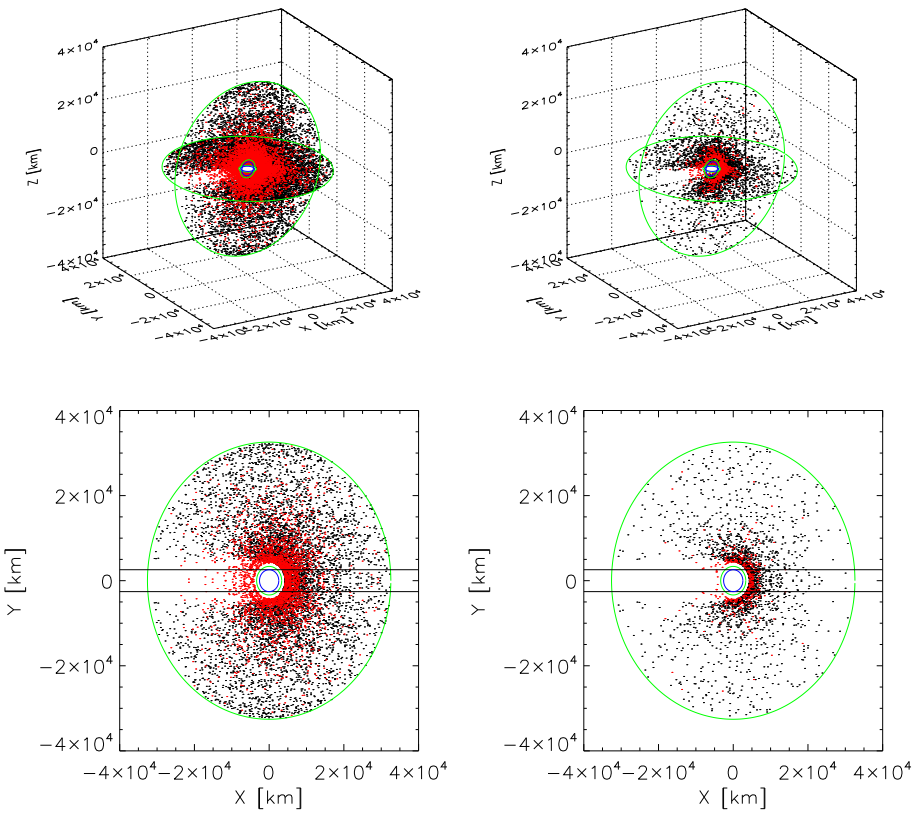

Fig. 7.3: Radiative transfer output for varying the atomic hydrogen distribution. Left diagrams: Distribution of scattering points when using the Chamberlain density distribution. Right diagrams of using the Particle model. The upper row shows the 3D distribution of first scattering positions (black) and multiple scattering positions (red). The bottom row shows the distribution in the x-y-plane. Black horizontal lines indicate the position of the intersecting histogram plot shown in Figure 7.4. Green circles indicate the model boundaries, the blue circle is Titan's surface. The Sun is located at ($x \rightarrow \infty$,y=0,z=0).

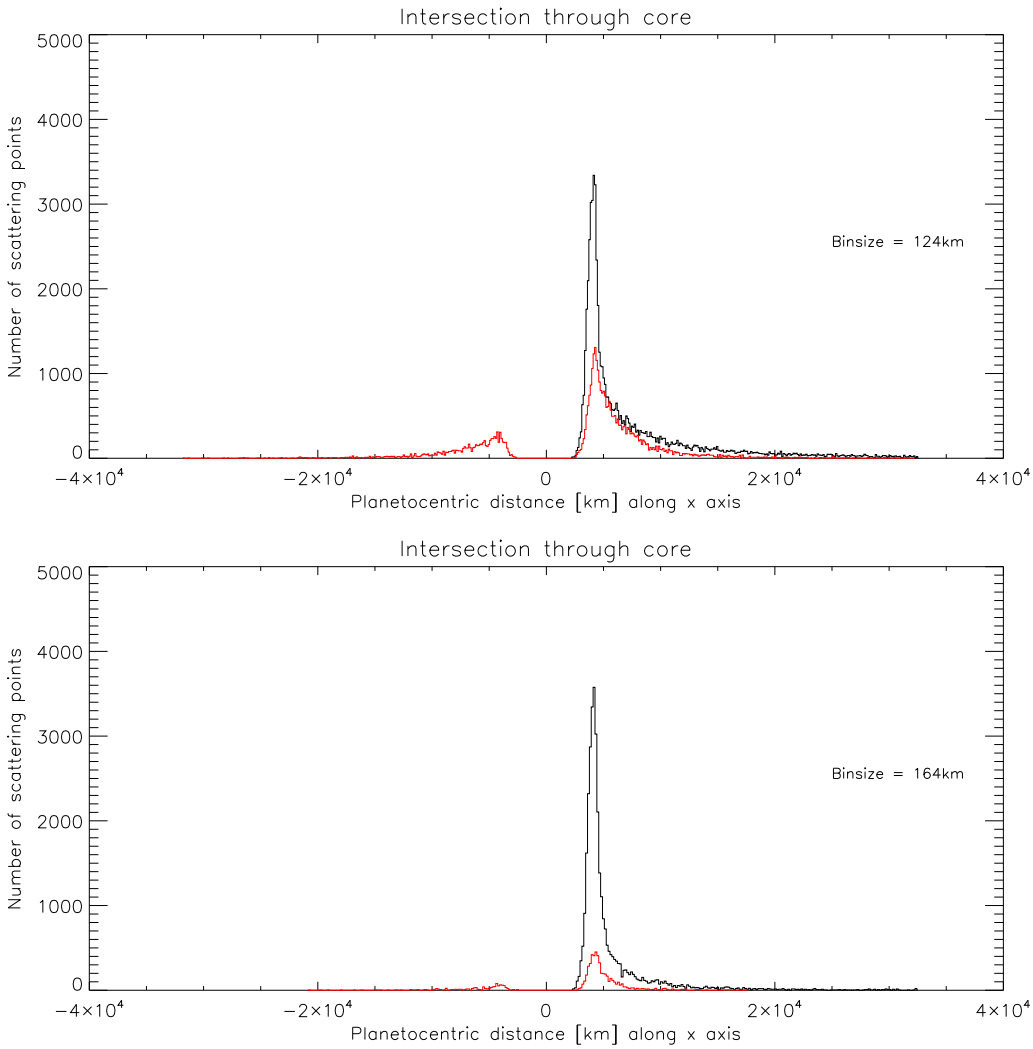

Fig. 7.4: Intersecting histogram plots in the range indicated by the black horizontal lines of the $x-y$-plots in Figure 7.3. Upper plot: Distribution of scattering points using the Chamberlain model; lower plot using the Particle model. The Sun is located at ($x \rightarrow \infty$,y=0,z=0).

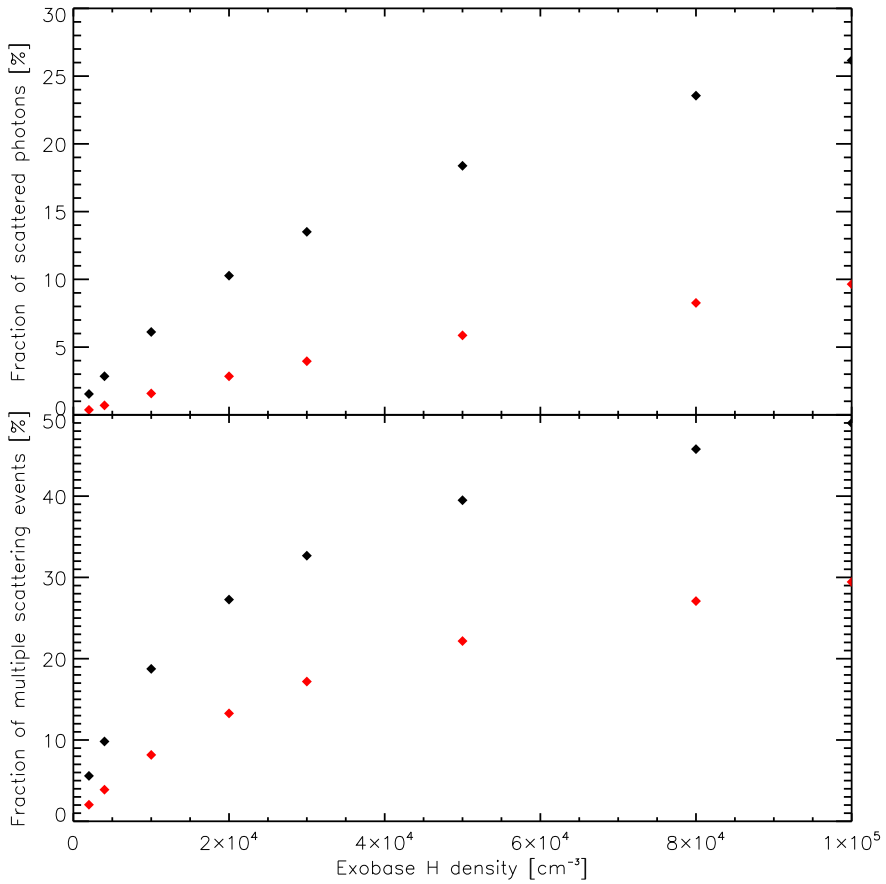

Fig. 7.5: Statistical output for the variation of the atomic hydrogen exobase densities. In the upper plot, the fraction of photons being scattered within the exosphere model (compared to the number of photons started) is shown (f_{Scat}), using the Chamberlain model (black diamonds) and using the Particle model (red diamonds). For the calculations an exospheric temperature of 150 K was assumed. The lower plot shows the fraction of multiple scattering events $f_{\mathrm{MS}} = 1 - f_{\mathrm{SS}}$, if the density of the exosphere is increased.

After applying the Data Sampling model the difference signal $I_0 - I$ of photometer mode (I_0), as well as when the H cell is switched on (I) is calculated. Contrary to the increase in the fraction of scattered photons by increasing the exospheric density, the difference signals ($I_0 - I$) in Figure 7.6 show a rather complex behavior:

The measured signal first increases with increasing exospheric density. This is especially visible at timestep 402, where the difference signal reaches its maximal value using an exobase density of about $n_{\mathrm{H}} = 1.0 \cdot 10^4\,\mathrm{cm}^{-3}$ for the Chamberlain model and about $n_{\mathrm{H}} = 2.0 \cdot 10^4\,\mathrm{cm}^{-3}$ for the Particle model. The difference signal then furthermore decreases rapidly. Since the Doppler

shift at timestep 402 is zero, the instruments absorbs radiation exactly in the line center. Figure 7.7 shows the value of the difference signals by varying the density at the beginning of the encounter (timestep 0), at closest encounter (timestep 419), and at the end of the encounter (timestep 840).

The behavior of measured signal can be explained, considering of which altitudes the detector is sensitive, hence where the optical depth in the line center as seen from the detector becomes unity. At low exospheric densities this level is reached at altitudes of about 1,750 km (depending on the spacecraft altitude). At these altitudes the absorption by methane is dominating the extinction in the exosphere (compared to the extinction caused by scattering of atomic hydrogen). Increasing the atomic hydrogen density allows radiation to be scattered effectively above this level.

However, above a certain density the extinction of the exosphere is dominated by scattering of atomic hydrogen, thus the exosphere becomes opaque at low altitudes, balancing the increased amount of scattering events. At even higher densities the optical depth of the exosphere becomes high enough such that radiation scattered into the direction of the detector is effectively attenuated in the line center, which is also known as "self-absorption".

The optical depth caused by scattering events along the photon flying direction thus becomes important by using exospheric densities as identified above. At higher densities the Lyman-α radiation is increasingly attenuated, as is indicated by the decreasing difference signal by increasing the densities. As the density gradient of the Chamberlain model distribution is much steeper than for the Particle model distribution, the decrease of Lyman-α radiation with increasing density takes place at even lower densities and much faster.

The signal excess at the beginning of the encounter, as measured by HDAC (see section 4.5.1) is also visible in the simulations, it therefore has no external source, as it was proposed in section 4.5.1 as a possible explanation. The difference signal at the end of the encounter shows also a weak excess, however with a much lower signal (see lowermost plot in Figure 7.7). The signal excess is due to the strong Lyman-α emission from the day side of Titan, at which HDAC looked at the beginning of the encounter. The absorption cell has therefore already absorbed the Lyman-α radiation in the line wings, although the Doppler shift was very high at the beginning of the encounter.

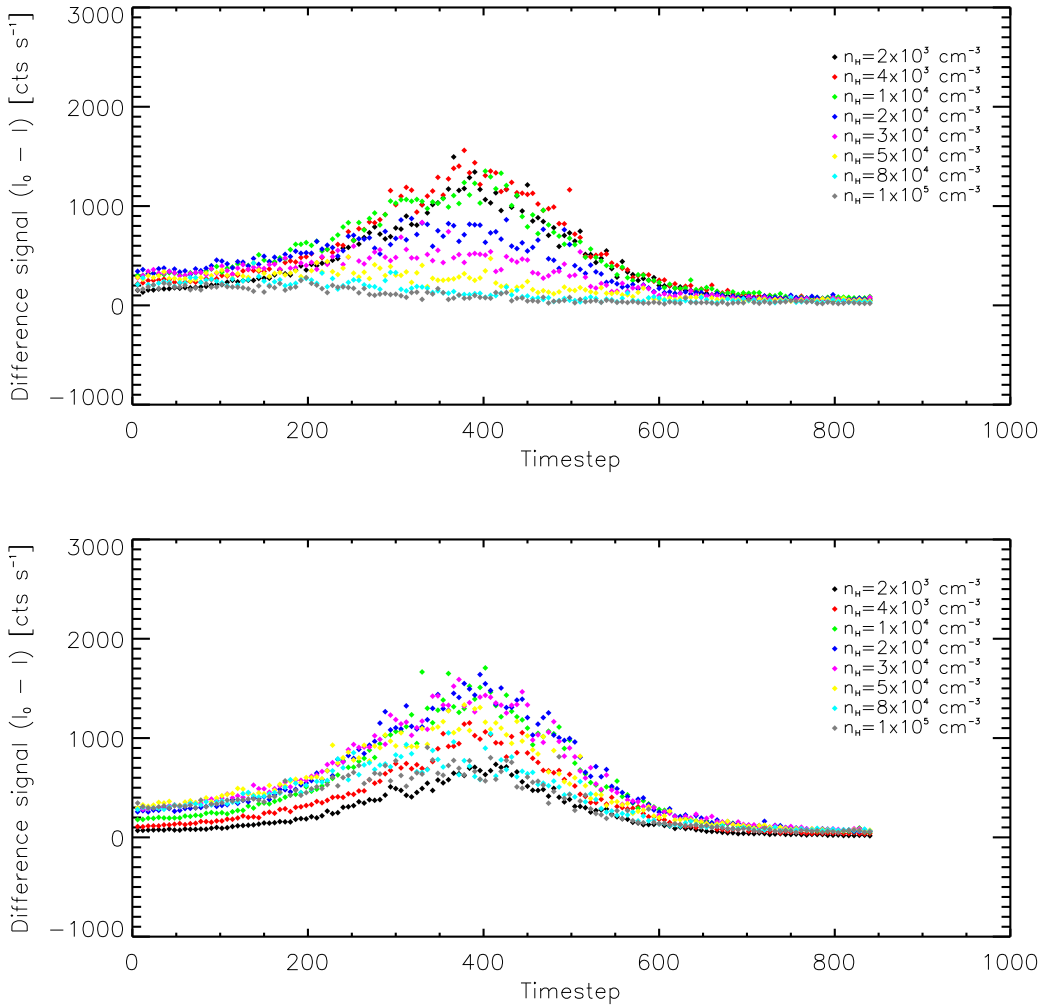

Fig. 7.6: Exobase hydrogen density variation: Difference signal of simulations performed in photometer mode (both cells off) and when the H cell was switched on during the T_9 flyby, using the Chamberlain model (upper plot) and using the Particle model (lower plot) for the calculation of exospheric H densities. For the calculations an exospheric temperature of 150 K was chosen.

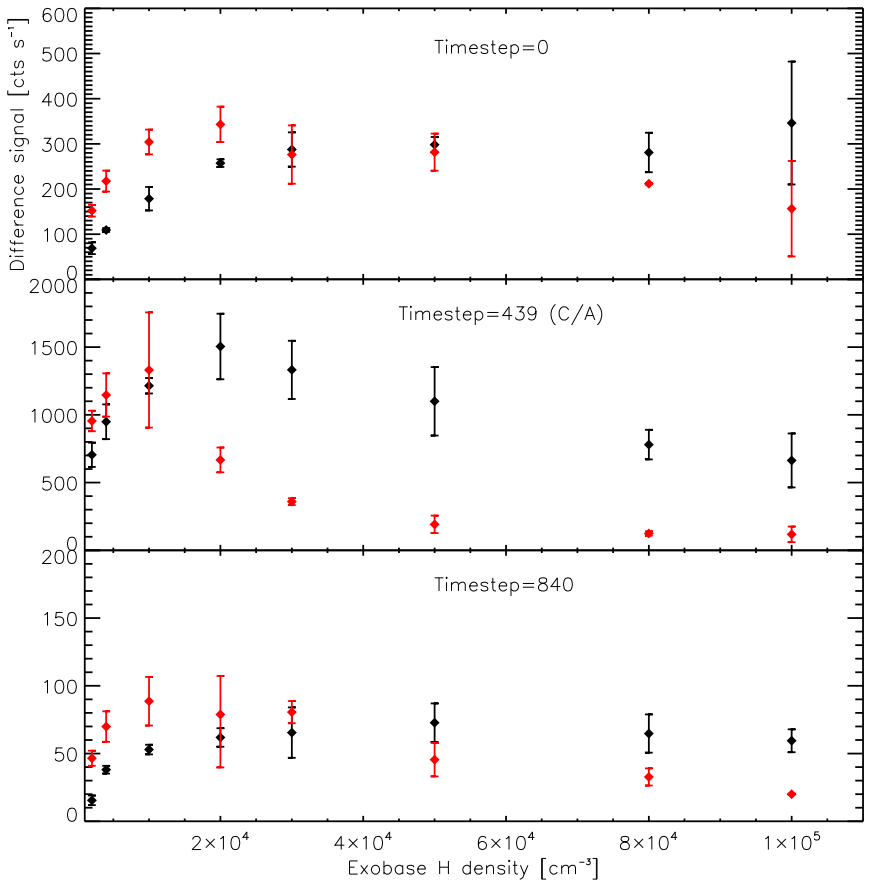

Fig. 7.7: Difference signals during the beginning (upper plot), during closest approach (center plot) and at the end of the encounter (lower plot), at timesteps of 0, 439 and 840, respectively, caused by varying the exobase densities (cf. Figure 7.6). Black diamonds indicate the difference signal when using the Particle model for the calculation of the atomic hydrogen distribution, whereas for the red diamonds the Chamberlain model was used. For the calculations an exospheric temperature of 150 K was chosen.

The amount of multiple scattering events in Titan's exosphere is low as can be already seen from Figure 7.5. In the difference signal this is also visible: Figure 7.8 shows the difference signal caused by single scattering events only, compared to the total difference signal. The radiative transfer calculations have been performing with exobase densities of $2.0 \cdot 10^3$ (upper plot) and $8.0 \cdot 10^4\,\mathrm{cm}^{-3}$ (lower plot) using the Particle model. For low exospheric densities, multiple scattering events are negligible, constituting only a fraction of about 1 to 2% of the signal, as can be seen in Figure 7.9 (black diamonds).

However, at the increased exospheric density (red diamonds in Figure 7.9), multiple scattering cannot be neglected: at the beginning of the encounter

about 85% of the signal is caused by single scattering, decreasing to about 70% during closest encounter and then increasing again when Cassini is departing from Titan. The amount of multiple scattering events is increased in the line center, which is measured when the spacecraft has a low Doppler shift, i.e. close to the closest approach. This is due to the higher optical depth in the line center and hence the shorter mean free path for photons having this wavelength.

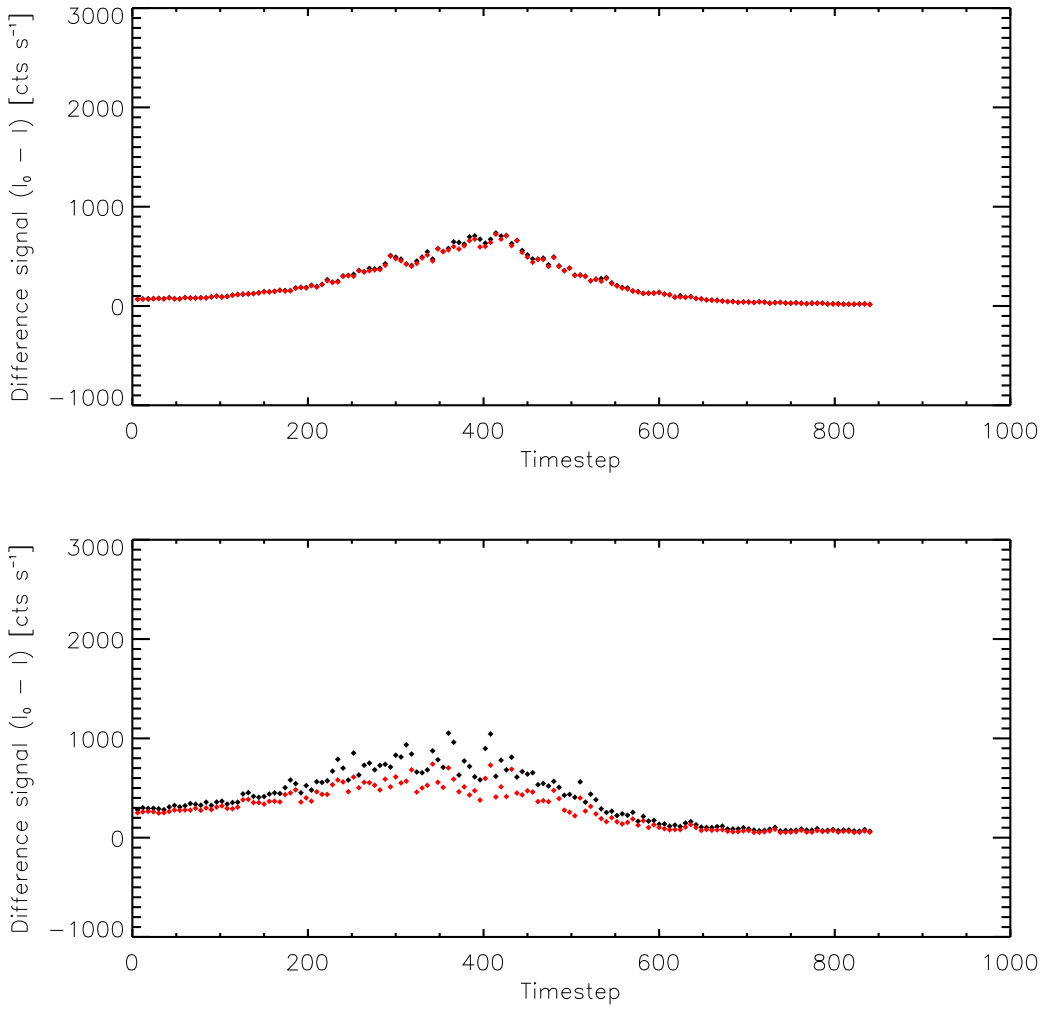

Fig. 7.8: Amount of single scattering events in the difference signal using the Particle model with an exobase density of $n_{\mathrm{H}} = 2.0 \cdot 10^3\ cm^{-3}$ (upper plot) and $n_{\mathrm{H}} = 8.0 \cdot 10^4\ cm^{-3}$ (lower plot). In the plots, black diamonds show the total difference signal whereas red diamonds show the difference signal caused by only single scattering events. For the calculations an exospheric temperature of 150 K was chosen.

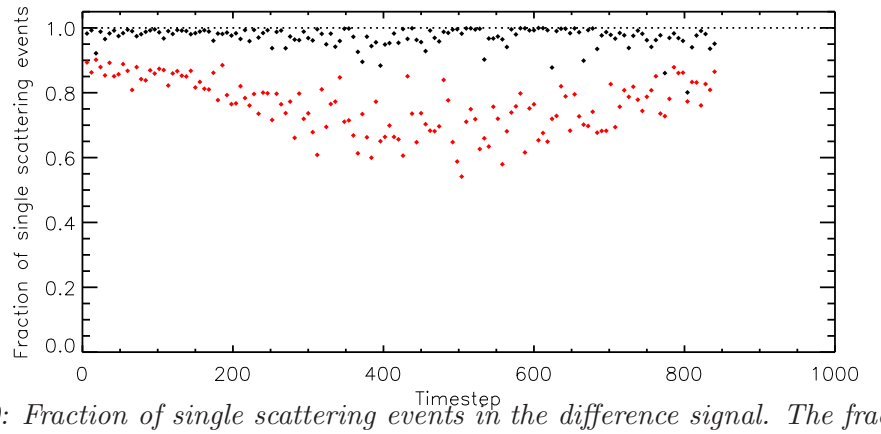

Fig. 7.9: Fraction of single scattering events in the difference signal. The fraction of single scattering events from Figure 7.8 is shown for exobase densities of $n_{\mathrm{H}} = 2.0 \cdot 10^3\, cm^{-3}$ (black diamonds) and $n_{\mathrm{H}} = 8.0 \cdot 10^4\, cm^{-3}$ (red diamonds). For the calculations an exospheric temperature of 150 K was chosen.

7.3 Exospheric temperature variation

The temperatures below Titan's exobase were recently inferred from INMS measurements (de La Haye et al., 2007b) yielding values from 149 K to 158 K. Above 1,500 km those authors find that a temperature of 149 K to 223 K is necessary to fit their data (cf. section 2.4). Also measurements performed by the UVIS instrument indicate temperatures of 150 to 200 K (D. Shemansky, priv. com.). Calculations are therefore performed with the Particle model density distribution and an exobase atomic hydrogen density of $n_{\mathrm{H}} = 8.0 \cdot 10^4\,\mathrm{cm}^{-3}$, using an temperature isoprofile with temperatures in the range measured (147 K, 150 K, and 158 K), as well as using increased temperatures of 175 K, 200 K and 250 K.

For clarity the difference signals are first shown for the temperature range from 147 to 158 K in Figure 7.10 and thereafter in an increased range with temperatures of 150 to 250 K in Figure 7.11.

Since the wavelength dependent resonance scattering cross section is proportional to the square root of the temperature, the cross section increases in the line wings with increasing temperatures. This is especially visible at the beginning and end of the encounter, because here HDAC is absorbing radiation in the line wings: With increasing exospheric temperature, the mean free path in the line wings becomes shorter (due to the increased optical depth) and hence the probability of an interaction is increased. Thus, the Lyman-α radiation emitted is increased in the line wings.

The exobase temperature variation within the range of literature values found has only a minor effect on the Lyman-α signal, when compared to the density variations mentioned above.

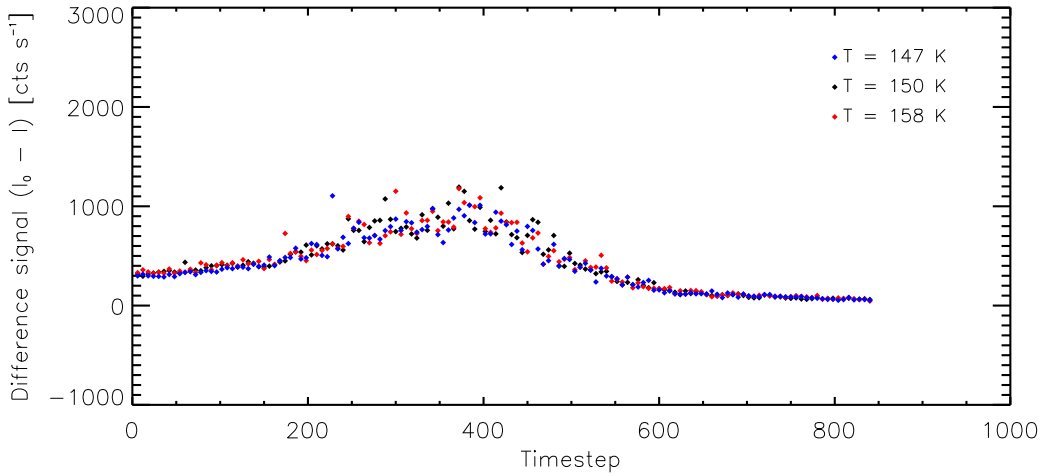

Fig. 7.10: Exospheric temperature variation in the temperature range from 147 K to 158 K: Difference signal of simulations performed in photometer mode (both cells off) and by the H cell was switched on during the T_9 flyby, using the Particle model with an exobase density of $n_{\mathrm{H}} = 8.0 \cdot 10^4\ cm^{-3}$.

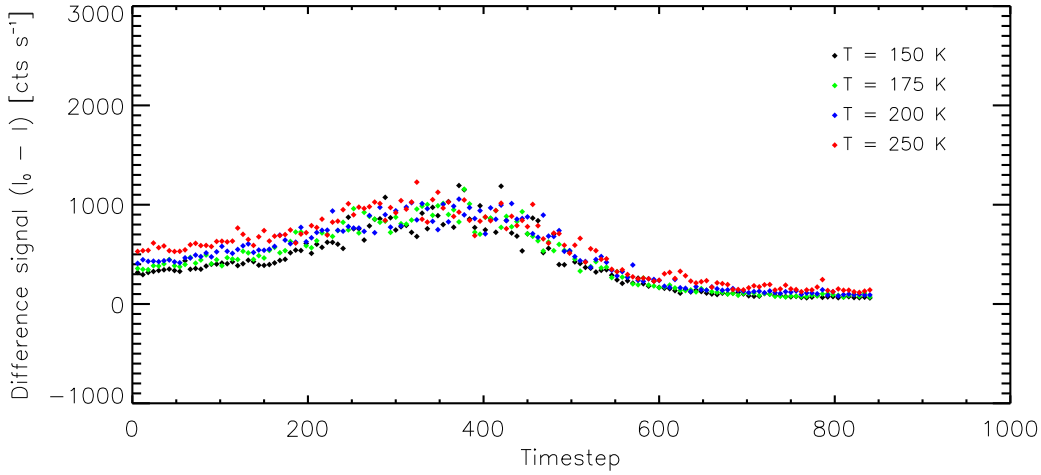

Fig. 7.11: Exospheric temperature variation in the temperature range from 150 K to 250 K: Difference signal of simulations performed in photometer mode (both cells off) and by the H cell was switched on during the T_9 flyby, using the Particle model with an exobase density of $n_{\mathrm{H}} = 8.0 \cdot 10^4\ cm^{-3}$.

8. MONTE CARLO RADIATIVE TRANSFER MODEL VALIDATION

In order to validate the Monte Carlo radiative transfer model described in chapter 6, a simple analytical model is constructed which includes only single scattering. The parameter variations performed in the last chapter are carried out again with this simple model and resulting differences are discussed.

8.1 Analytical approach

In the analytical model, a simplified approach of the radiative transfer equation is solved. Multiple scattering is neglected, hence only the resonant scattering of solar light into the line of sight of HDAC needs to be taken into account. This is justified for the outer exospheric regions, where the optical depth is low. However, since HDAC always points towards Titan, the lower exospheric layers are also sensed and multiple scattering can no longer be neglected. Nevertheless Monte Carlo radiative transfer calculations assuming a very low exospheric density (i.e. exobase densities of $2 \cdot 10^3\,\mathrm{cm}^{-3}$) have shown that the total contribution of multiple scattering events to the signal is negligible (see Figure 7.9). At higher densities, multiple scattering events contributes significantly to the signal. Thus, in the limit of low exospheric densities, the Monte Carlo model can be validated with the assumption of single scattering. For higher densities, only a qualitative comparison can performed. It will be shown in the next chapter, that the HDAC measurements can only be fitted taking multiple scattering into account. Thus, this simple approach cannot be applied to simulate the measurements, but it is very important to validate the required Monte Carlo model.

A further assumption is that the scattering is coherent, i.e. contrary to the Monte Carlo model, the wavelength of the photon does not change after scattering. This assumption is based on the fixed wavelength grid that is used for the analytical model calculations. Taking into account non-coherence effects, with changing wavelengths is thus demanding and beyond the aim of this model validation.

The radiative transfer (equation 3.14) can be expressed as

$$\frac{\mathrm{d}I_\nu(s,\hat{\mathbf{k}})}{\mathrm{d}s} = -\chi_\nu I_\nu(s,\hat{\mathbf{k}}) + \bar{s}_\nu(s)\frac{1}{4\pi}\int_\Omega I_\nu(s,\hat{\mathbf{k}}')\mathrm{d}^2\hat{k}', \tag{8.1}$$

with s being the line of sight of HDAC, I_ν the spectral intensity, $\hat{k}$ the direction, $\bar{s}_\nu$ the total scattering coefficient, and χ_ν the extinction coefficient, as introduced in chapter 3.

By defining the source function

$$S_\nu(s) = \frac{\bar{s}_\nu(s)}{\chi_\nu(s)}\frac{1}{4\pi}\int_\Omega I_\nu(s,\hat{\mathbf{k}}')\mathrm{d}^2\hat{k}', \tag{8.2}$$

equation 8.1 results in

$$\frac{\mathrm{d}I_\nu(s)}{\mathrm{d}s} = -\chi_\nu(I_\nu(s) - S_\nu(s)). \tag{8.3}$$

Division by $-\chi_\nu$ and introducing $-\chi_\nu \mathrm{d}s = \mathrm{d}\tau_\nu$ yields

$$\frac{\mathrm{d}I_\nu}{\mathrm{d}\tau_\nu} = (I_\nu - S_\nu). \tag{8.4}$$

Multiplying with the integrating factor $\exp(-\tau_\nu)$ and rearranging the above equation yields

$$-\frac{\mathrm{d}}{\mathrm{d}\tau_\nu}\left(I_\nu \exp(-\tau_\nu)\right) = S_\nu \exp(-\tau_\nu). \tag{8.5}$$

Integrating with respect to τ_ν and solving the left hand side of equation 8.5 results in

$$I_\nu(0) - I_\nu(\tau_\nu)\exp(-\tau_\nu) = \int_0^{\tau_\nu} S_\nu(\tau'_\nu)\exp(-\tau'_\nu)\mathrm{d}\tau'_\nu. \tag{8.6}$$

Finally, one obtains

$$I_\nu(0) = I_\nu(\tau_\nu)\exp(-\tau_\nu) + \int_0^{\tau_\nu} S_\nu(\tau'_\nu)\exp(-\tau'_\nu)\mathrm{d}\tau'_\nu. \tag{8.7}$$

Inserting the source function $S_\nu(\tau'_\nu)$ yields

$$I_\nu(0) = I_\nu(\tau_\nu)\exp(-\tau_\nu) + \int_0^{\tau_\nu} \frac{\bar{s}_\nu(\tau'_\nu)}{\chi_\nu(\tau'_\nu)}\frac{1}{4\pi}\int_\Omega I_\nu(\tau'_\nu,\hat{\mathbf{k}}')\exp(-\tau'_\nu)\mathrm{d}^2\hat{k}'\mathrm{d}\tau'_\nu. \tag{8.8}$$

The optical depth τ'_ν has been chosen in the viewing direction of the detector, being zero at the detector and τ_ν at the end of the line of sight (LOS).

Hence, $I_\nu(0)$ expresses the intensity measured by the detector. In equation 8.8, $I_\nu(\tau_\nu)$ is the direct radiation along the LOS of the instrument, weakened by the transmission $\exp(-\tau'_\nu)$ along the LOS. I_ν thus includes both the solar radiation and the radiation emitted from Titan. As the instrument (HDAC) is not looking at the Sun but rather at Titan's surface, this term becomes zero since Titan is not emitting radiation in the UV: Since multiple scattering is neglected and the solar position remains unchanged in the chosen coordinate system, the dependence on the viewing direction $\hat{\mathbf{k}}$ can be separated:

$$I_\nu(\tau_\nu, \hat{\mathbf{k}}) = \bar{I}_\nu(\tau_\nu) \cdot \omega_{I_\nu}(\hat{\mathbf{k}}) = \bar{I}_\nu(\tau_\nu) \cdot \delta(\hat{\mathbf{k}} - \hat{\mathbf{k}}_\odot), \tag{8.9}$$

with $\bar{I}_\nu(\tau_\nu)$ being the total spectral intensity emitted by the Sun and ω_{I_ν} describing the angular dependence. $\hat{\mathbf{k}}_\odot$ is the direction towards Sun, which in this work is given by

$$\begin{aligned} \hat{k}_{\odot,x} &= 1 \\ \hat{k}_{\odot,y} &= 0 \\ \hat{k}_{\odot,z} &= 0. \end{aligned} \tag{8.10}$$

The remaining part of equation 8.8 describes the scattering of solar radiation into the LOS of the detector, also weakened by the absorption along the LOS. Equation 8.8 hence becomes

$$I_\nu(0) = \int_0^{\tau_\nu} \frac{\bar{s}_\nu}{\chi_\nu} \frac{1}{4\pi} \bar{I}_\nu(\tau'_\nu) \exp(-\tau'_\nu) \mathrm{d}\tau'_\nu, \tag{8.11}$$

which can be solved using numerical integration schemes.

The total solar Lyman-α intensity entering the model boundaries $\bar{I}_\nu$ is obtained from SORCE (see section 6.4). Since the intensity does not change in the small wavelength range considered, the wavelength dependence of $\bar{I}$ is omitted. At a solar distance of Titan of 9.09 AU during the T_9 flyby a total solar Lyman-α intensity of $\bar{I} = 7.8665 \cdot 10^{-9}\,\mathrm{J\,cm^{-2}\,s^{-1}}$ is obtained. The radiative transfer calculations are then performed without the absorption pattern of the HDAC absorption cells. Since HDAC acts as photodetector and measures the signal in counts per second, the line center Lyman-α photon flux needs to be calculated: Using the relation between the total solar Lyman-α irradiance and the line center irradiance from Emerich et al. (2005), $\bar{I}$ is converted into a photon flux and the HDAC absorption pattern is finally considered.

8.2 Analytical model compared with Monte Carlo calculations

First the atomic hydrogen exobase density is varied in the range from $n_{\mathrm{H}} = 2 \cdot 10^3\,\mathrm{cm}^{-3}$ to $n_{\mathrm{H}} = 1 \cdot 10^5\,\mathrm{cm}^{-3}$, using both exospheric density models.
In the analytical approach the difference signals between calculations where both cells are switched off (photometer mode: I_0) and where the H cell is switched on (I), shows a similar behavior as found from calculations using the Monte Carlo radiative transfer model (see Figure 8.1): The emitted Lyman-α radiation first increases with increasing exospheric density and then falls off rapidly. The decrease of the difference signal at high densities during closest approach is mainly caused by the low altitude of the spacecraft and the higher optical depth of the exosphere: As the optical depth increases, the absorption along the LOS exceeds the effect of scattering and the Lyman-α line is attenuated in the line center. This self-absorption effect becomes important at lower exospheric densities in the analytical model calculations as compared to the Monte Carlo calculations: Using the Chamberlain atomic hydrogen profile, there is no maximum visible - however it is predicted to occur at slightly lower densities. Considering the Particle model profile, the maximal difference signal forms at an exobase density of $n_{\mathrm{H}} = 1{\cdot}10^4\,\mathrm{cm}^{-3}$, compared to $n_{\mathrm{H}} = 2 \cdot 10^4\,\mathrm{cm}^{-3}$ in the Monte Carlo calculations.
The reason for this is the assumption of a coherent scattering process. At timestep 403, where HDAC absorbs in the line center, the angle between the LOS direction and the solar direction (i.e. the scattering phase angle γ) is about 90° (cf. Figure 4.6; note that the scattering phase angle is given by $\gamma = \pi$-SZA). In the Monte Carlo calculations the non-coherence of the scattering event due to the Doppler shift in the external frame causes a wavelength shift of the emitted photon compared to the wavelength of the incident photon. At a scattering phase angle of about 90°, the non-coherence favors the emission of photons with wavelengths close to the line center (cf. section 6.2.4 and Figure 6.2). Thus, taking into account this effect would cause the difference signal close to closest encounter to be increased in the line center, covering the self-absorption effect.
The effects caused by FOV changes due to pointing corrections of the spacecraft are clearly visible - the statistical noise of the Monte Carlo radiative transfer calculations cover this effect.

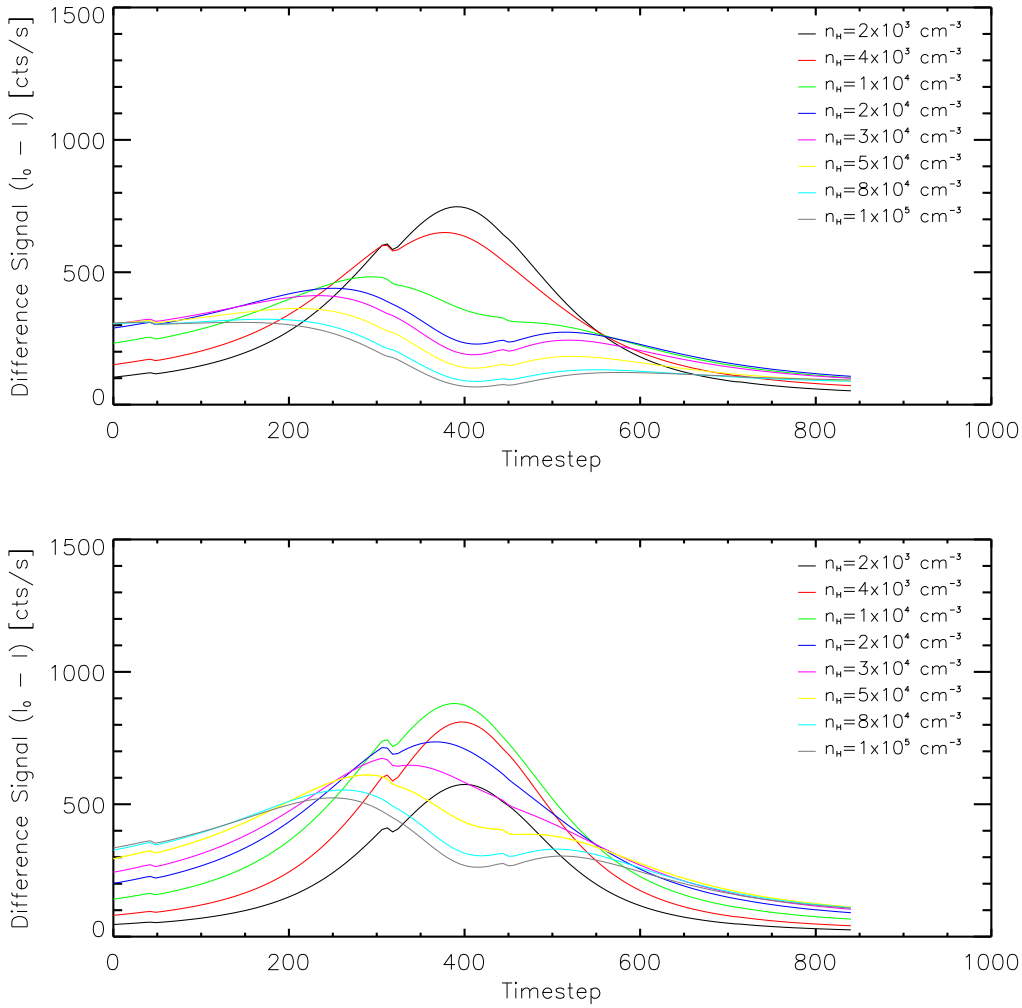

Fig. 8.1: Exospheric density variation: Calculated difference signal using a simplified analytical radiative transfer model.

The temperature variation was performed using an atomic hydrogen distribution calculated by the Particle model with an exobase density of $8 \cdot 10^4\,\mathrm{cm}^{-3}$. The analytical approach much more clearly indicates the temperature dependence of the Lyman-α emission (see Figure 8.2), which was also suggested by the Monte Carlo radiative transfer calculations in section 7.3. The increasing temperature causes the difference signal to increase in the line wings (especially visible at the beginning of the encounter) due to the temperature dependence of the scattering cross section. However, an increased scattering cross section also causes the line center to be more strongly absorbed due to the afore-mentioned self-absorption effect. This effect is particularly apparent above 200 K, where the signal decreases.

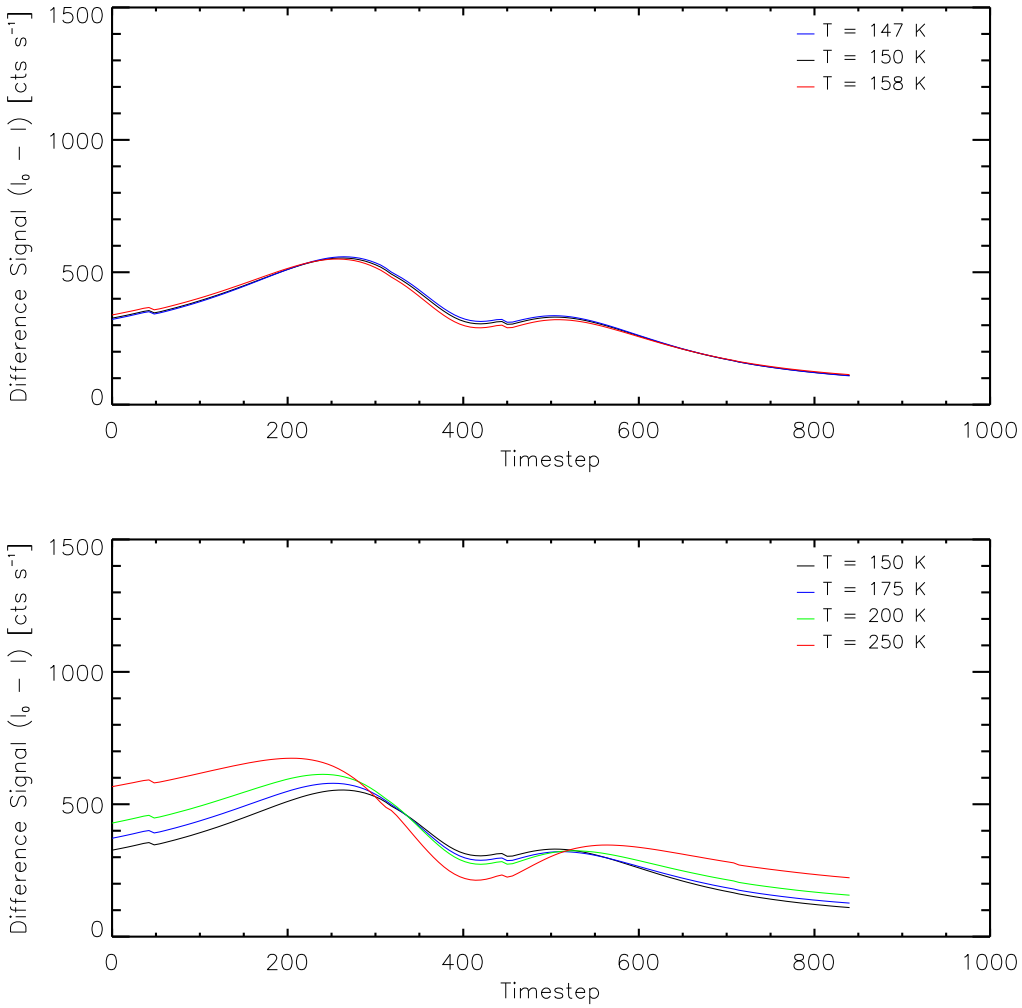

Fig. 8.2: Exospheric temperature variation: Difference signal using a simplified analytical radiative transfer model. The calculations were performed using an atomic hydrogen density profile calculated by the Particle model with an exobase hydrogen density of $n_{\mathrm{H}} = 8 \cdot 10^4\ cm^{-3}$.

In total, with the simplified analytical model presented here, the transfer of solar radiation through Titan's exosphere can be easily investigated qualitatively. However, a qualitative validation of the model is only possible in the exospheric regions where multiple scattering can be neglected. Also the amount of single scattering has to be low, in order to compensate for the disregarding of non-coherence scattering in the analytical solution.
Therefore, an exobase density of $n_{\mathrm{H}} = 2 \cdot 10^3\,\mathrm{cm}^{-3}$ is chosen as input for both exospheric density models, i.e. where the fraction of multiple scattering events is negligible (cf. Figure 7.9). The comparison is performed using the difference signal in the single scattering limit of the Monte Carlo radiative transfer model.

Figure 8.3 shows the output of both radiative transfer models. Using the Particle model distribution model, the analytical solution of the radiative transfer calculation yields a comparable signal to the Monte Carlo calculations. However, by applying the Chamberlain density profile, the difference is much bigger. As was seen before, the assumption of a coherent scattering is mainly responsible for the main differences between both radiative transfer models. The difference using the Chamberlain distribution is much higher since the scattering is increased with respect to the Particle model profile. Hence non-coherence scattering plays a decisive role.

A quantitative comparison is thus only partly possible in the outer parts of the exosphere, where single scattering dominates. Since the measurements performed by HDAC also sense the lower exosphere, a comparison can be only made assuming very low exospheric densities where the amount of single scattering is high. However, calculations performed by both radiative transfer models differ slightly due the assumption of a coherent scattering process in the analytical approach.

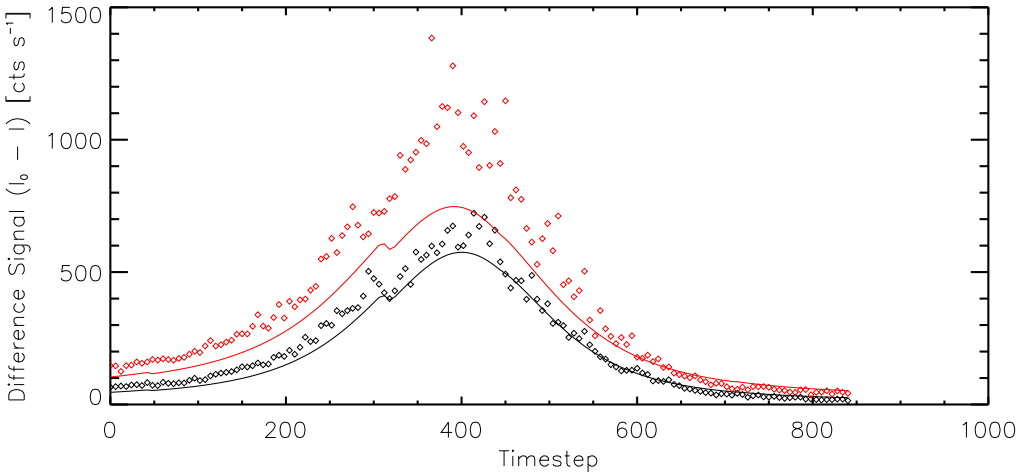

Fig. 8.3: Comparison of calculations performed using the analytical radiative transfer model (solid lines) and using the Monte Carlo approach (diamonds). The calculations were performed with a fixed exobase density of $n_{\mathrm{H}} = 2 \cdot 10^3\ cm^{-3}$ *for the Chamberlain model (red) and for the Particle model (black). The calculations have been performed with an exospheric temperature 0f 150 K.*

9. COMPARISON WITH MEASURED DATA

In this chapter the Monte Carlo radiative transfer calculations are compared with data measured by HDAC during the T_9 flyby. Since the background level in the HDAC data is a priori unknown, first the difference signals are compared in order to find the best fit and then the contribution by background sources to the signal is determined.

9.1 Results

In chapter 7 a parameter study was performed in order to infer the response of the difference signal. It could be shown that the exospheric density has the strongest effect on the signal detected, whereas the temperature variation had only a minor effect.
In order to fit the measured HDAC data and to save computation time[1], first the difference signals computed by the set of parameters used for the parameter study in chapter 7 are compared to the HDAC data. This involves exobase densities of $2 \cdot 10^3\,\mathrm{cm}^{-3}$, $4 \cdot 10^3\,\mathrm{cm}^{-3}$, $1 \cdot 10^4\,\mathrm{cm}^{-3}$, $2 \cdot 10^4\,\mathrm{cm}^{-3}$, $3 \cdot 10^4\,\mathrm{cm}^{-3}$, $5 \cdot 10^4\,\mathrm{cm}^{-3}$, $8 \cdot 10^4\,\mathrm{cm}^{-3}$,$1 \cdot 10^5\,\mathrm{cm}^{-3}$ and an exospheric temperature of 150 K for each of both density models. The best fitting density from this data set is found by determining the minimum of the least squares value

$$\chi^2 = \sum_{i=0}^{n} [y_i - f(x_i)]^2, \tag{9.1}$$

where n denotes the total number of measured data points y and $f(x)$ denotes the respective value obtained from the simulation. At a fixed temperature of 150 K, the best fit within the above mentioned parameter set was achieved by using the Chamberlain model distribution with $n_H = 2 \cdot 10^3\,\mathrm{cm}^{-3}$, whereas for the Particle model, the best fit was achieved with $n_H = 8 \cdot 10^4\,\mathrm{cm}^{-3}$.
This approach is justified since the density variation has the strongest effect on the signal near the closest encounter, and only a minor effect at the beginning and at the end of the flyby. The temperature variation however,

[1] One calculation takes about 25 hours. Note that for every parameter set the median of five independent calculations was used to calculate the resulting signal.

showed only a slight impact on the difference signal at the beginning of the encounter, whereas during the closest approach and at the end of the encounter it shows only a negligible effect.

Having identified the best fitting parameters from the variation, the parameter range that is used for the final fit is thus increased for a more precise determination of the values. Additional calculations are performed using the Chamberlain model with densities of $1 \cdot 10^4\,\mathrm{cm}^{-3}$, $2 \cdot 10^4\,\mathrm{cm}^{-3}$, $3 \cdot 10^4\,\mathrm{cm}^{-3}$ and temperatures of 175 K, 200 K and 250 K. Using the Particle model, additional calculations with densities of $7 \cdot 10^4\,\mathrm{cm}^{-3}$, $8 \cdot 10^4\,\mathrm{cm}^{-3}$, $9 \cdot 10^4\,\mathrm{cm}^{-3}$ and $1 \cdot 10^5\,\mathrm{cm}^{-3}$ and temperatures of 175 K, 200 K and 250 K are performed. This parameter grid was chosen due to the strong noise in the measured HDAC signal, which do not allow for calculations on a much finer grid. On this grid, finally the best fitting parameters are determined by using the above mentioned least squares method.

Using the density profile calculated by the Particle model, the best fit is achieved with an exospheric temperature of 175 K and an density distribution with an exobase atomic hydrogen density of $n_\mathrm{H} = 9 \cdot 10^4\,\mathrm{cm}^{-3}$ (see Figure 9.1 for a comparison, as well as for the residual signal). The residual signal of the fit indicates a high-frequency noise pattern caused by the HDAC signal, which was already identified in section 4.5.3. Due to this noise pattern the measurement can also be fitted with an exobase density of $n_\mathrm{H} = 8 \cdot 10^4\,\mathrm{cm}^{-3}$ with a temperature of 150 K or with $n_\mathrm{H} = 1 \cdot 10^5\,\mathrm{cm}^{-3}$ and 200 K. Taking into account this uncertainty, the best fit is thus given by $n_\mathrm{H} = (9 \pm 1) \cdot 10^4\,\mathrm{cm}^{-3}$ and $T = (175 \pm 25)\,\mathrm{K}$.

Using the Chamberlain density profile, one obtains the best fit with a density profile with a much lower exobase density of $n_\mathrm{H} = 2 \cdot 10^4\,\mathrm{cm}^{-3}$ (see Figure 9.2) and an exospheric temperature of $T = 175\,\mathrm{K}$. As for the Particle profile, the signal can also be fitted with exospheric temperatures of 150 K and 200 K. However, the uncertainty in the density determination is much lower, since in this density range the difference signal decreases rapidly with increasing exospheric density (see Figure 7.7). The best result is hence achieved with an exobase density of $n_\mathrm{H} = (2 \pm 0.5) \cdot 10^4\,\mathrm{cm}^{-3}$ and $T = (175 \pm 25)\,\mathrm{K}$.

Both difference signals are comparable within the error bars of both calculations, (cf. Figure 9.3). Here also the residual signal is shown. Only near to the closest encounter of the flyby both difference signals differ slightly mainly due to statistical errors in the computations.

The resulting exobase atomic hydrogen densities found are comparable to literature values, with an exobase density using profile computed by the Particle model being comparable to the value inferred by (de La Haye et al., 2007a). Using the density distribution calculated by the Chamberlain model, the best fitting exobase value found is lower than the value from recent publications (Garnier et al., 2007; Krasnopolsky, 2009; de La Haye et al., 2007a), but still within the range of values published (cf. table 2.2).

The best fitting exospheric temperature determined lies within the range suggested by INMS measurements of de La Haye et al. (2007b), indicating a temperature in the range of (147–228) K, as well as comparable to measurement by the UVIS instrument, indicating an exospheric temperature of (150–200) K (D. Shemansky, priv. com.). However, due to the noise pattern in the HDAC measurements, an exact temperature determination is not possible. However, with more accurate measurements HDAC could have provided useful information on the exospheric temperature.

A good indicator, for the altitude range to which HDAC is sensitive is the optical depth in the Lyman-α line center. The altitude seen by HDAC, at which the optical depth along the LOS becomes unity indicates that the transmission is of about 37% to the detector. As the spacecraft approaches Titan during ingress and departs during egress, the instrument detects radiation from different altitudes, allowing the determination of atomic hydrogen densities at different altitudes. The resulting values of these altitudes differ whether the Chamberlain or the Particle model density profile is used. The corresponding values for the Chamberlain model will thus be given in brackets in the following:

At the beginning of the encounter, the optical depth becomes unity in the line center at an altitude of about 4,334 km (4,014 km). During the closest encounter the altitude decreases to 3,716 km (3,090 km) and then increases to 4,402 km (4,076 km), as the spacecraft departs from Titan. These altitudes are considerably higher than the exobase altitude of 1,500 km. However, independently of the density model used, the atomic hydrogen density is about $7 \cdot 10^3\,\mathrm{cm}^{-3}$ in this altitude range (see Figure 9.4).

Figure 9.4 shows both atomic hydrogen profiles which fit the measured data at best, as well as the altitudes, at which the optical depth becomes unity in the line center. The HDAC measurement thus allows the estimation of the atomic hydrogen distribution in the altitude range above about 3,500 km, up to the spacecraft altitude (see Figure 4.5).

The average density profile of both exospheric density models in the altitude

range, to which HDAC is sensitive, is shown in Figure 9.5. The error of this fit has been estimated from the deviation of both profiles from the average value at the lowest altitudes, at which the optical depth becomes unity as seen by HDAC. Due to the noise pattern of the HDAC measurements as well as due to statistical errors of the Monte Carlo radiative transfer calculations, the error in the exospheric densities is estimated to be about 25% (indicated by the blue long-dashed lines in Figure 9.5). The decision, whether one density distribution model fits the distribution of atomic hydrogen better than the other can therefore not be made from the HDAC observations during the T_9 encounter alone, especially not for the lower exosphere, where both density distribution models have their largest differences. More accurate measurements in a lower altitude range are thus required in order to determine the parameters at the exobase. Two reasonable Titan flyby's of the Cassini orbiter in 2010, where HDAC is due to this work planned to be used again are T_{66} and T_{67} in 2010. The trajectories and estimated signals during both flybys are discussed below in section 9.2.

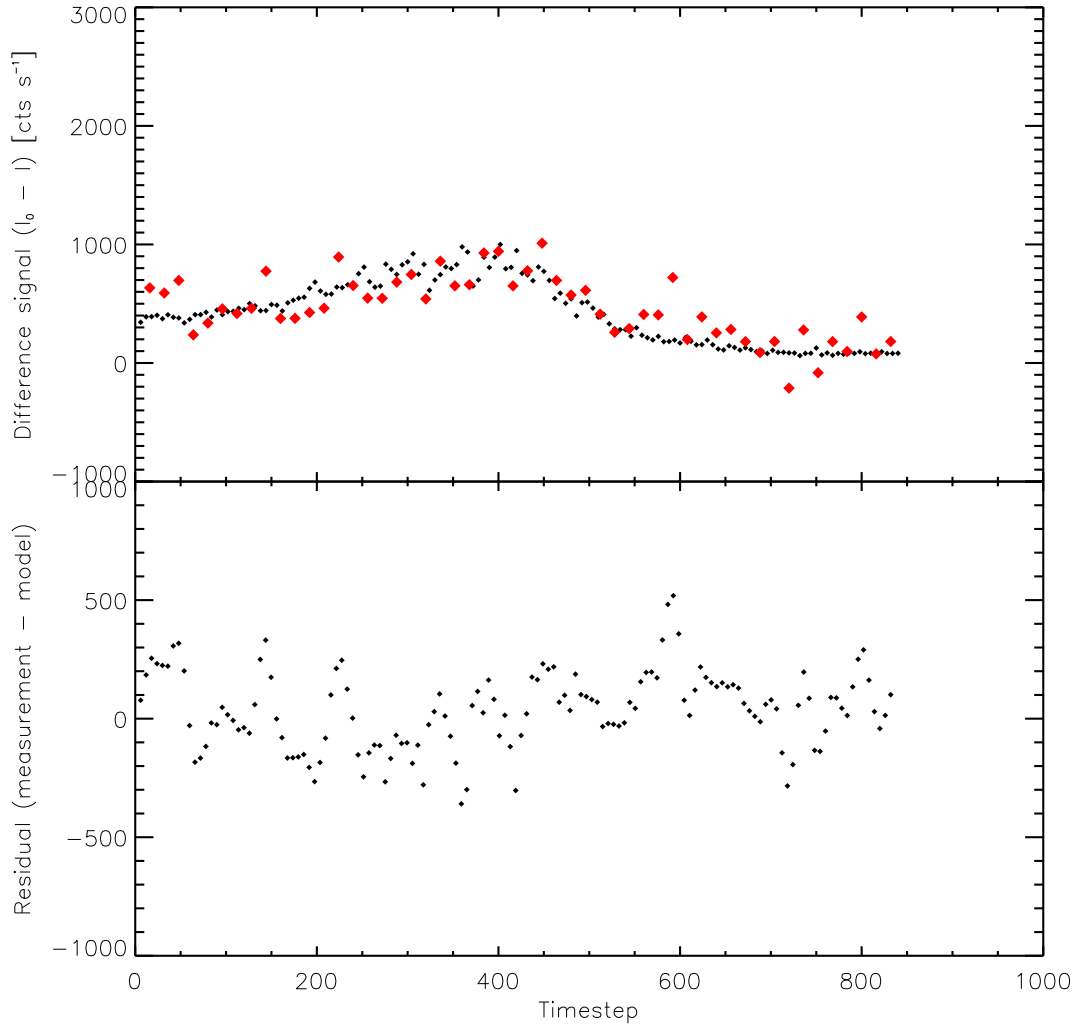

Fig. 9.1: Best fitting simulated signal (black diamonds) as compared to measurements during the T_9 encounter (red diamonds) using the Particle model for the calculation of exospheric atomic hydrogen densities. The top figure shows the best fitting difference signal, simulated using the Particle model with an exobase density of $n_{\mathrm{H}} = 9 \cdot 10^4\, cm^{-3}$ and an exospheric temperature of 175 K, whereas the bottom figure shows the residuals signal of the fit.

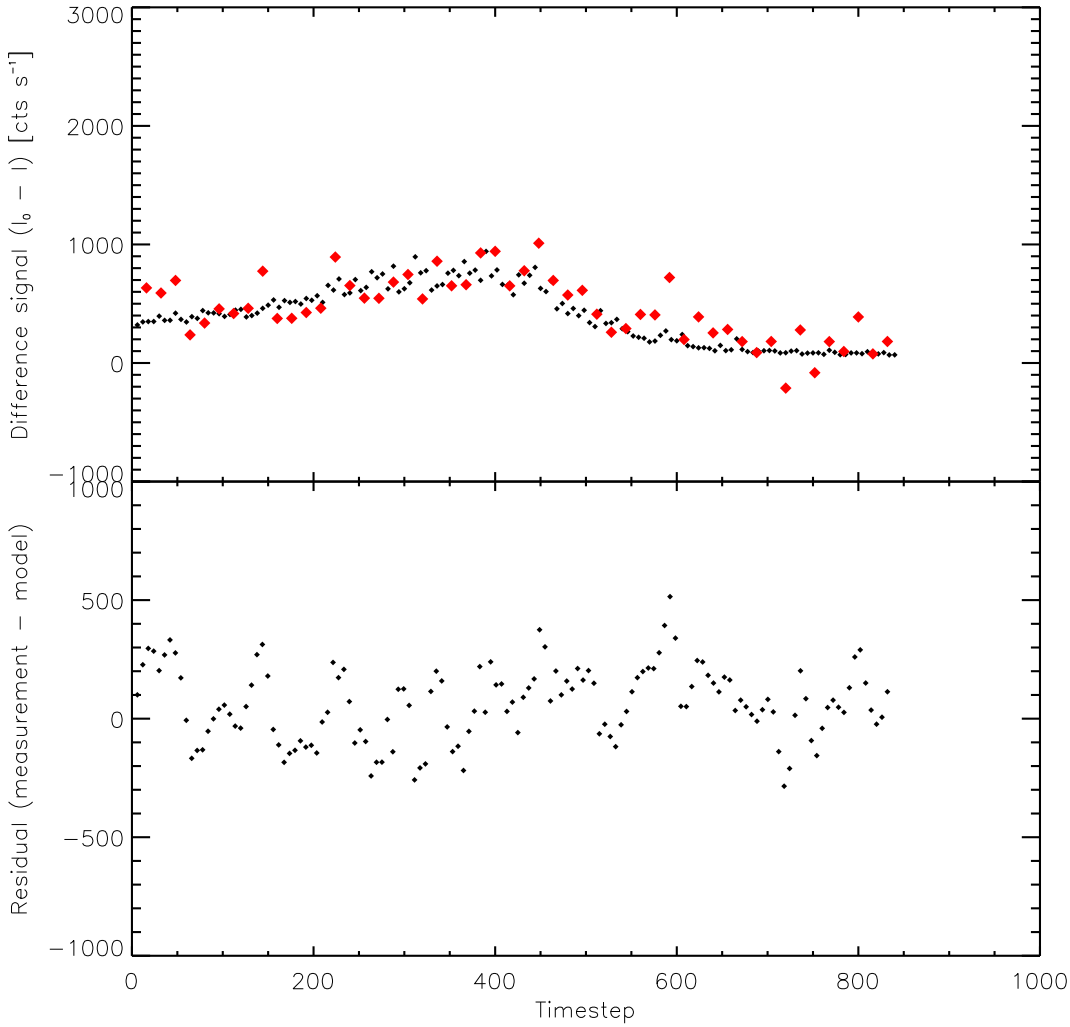

Fig. 9.2: Best fitting simulated signal (black diamonds) as compared to the measurement during the T_9 encounter (red diamonds) using the Chamberlain model for the calculation of exospheric atomic hydrogen densities. The top figure shows the best fitting difference signal, simulated using the Chamberlain model with an exobase density of $n_{\mathrm{H}} = 2 \cdot 10^4\, cm^{-3}$ and an exospheric temperature of 175 K, whereas the bottom figure shows the residuals signal of the fit.

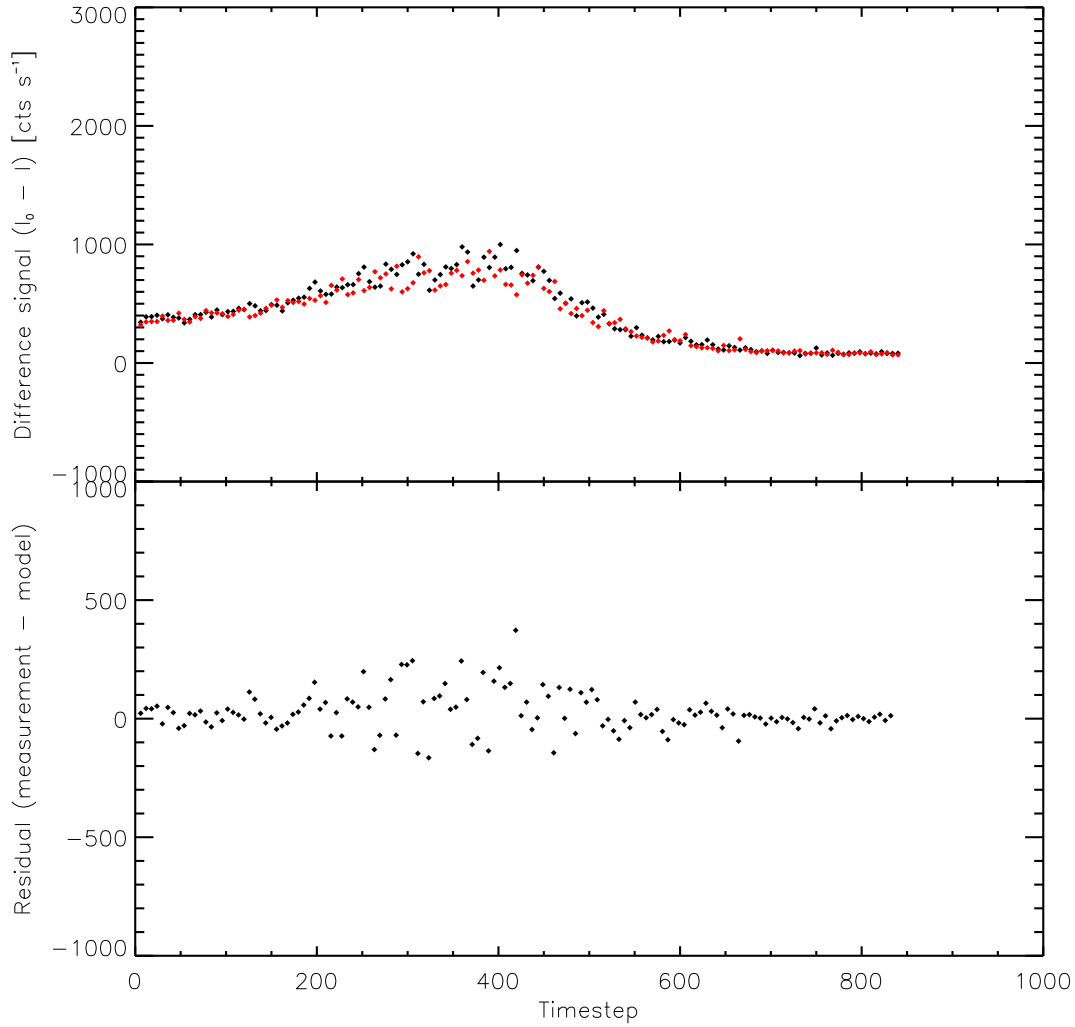

Fig. 9.3: Comparison of the best fitting difference signals using the Particle model (black diamonds) and using the Chamberlain model (red diamonds). In the lower figure the residual is shown.

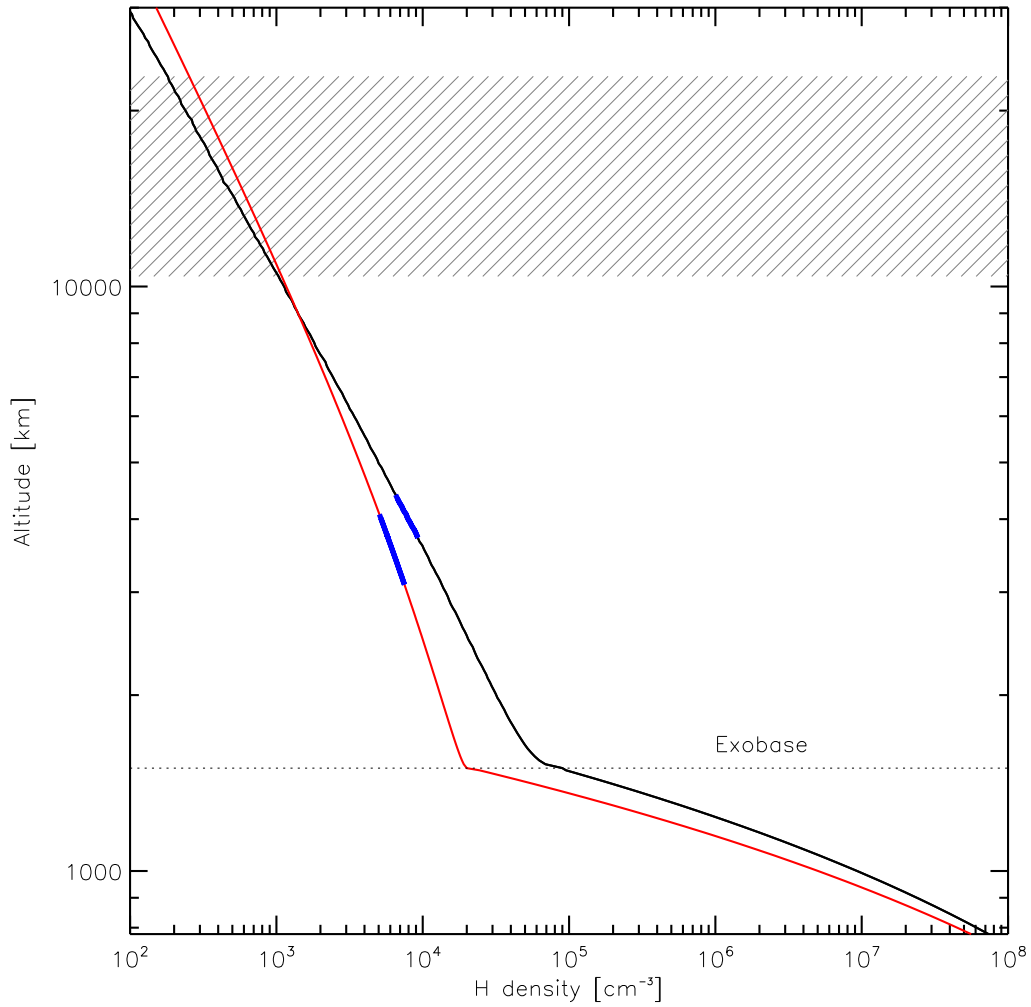

Fig. 9.4: Best fitting atomic hydrogen profile using the Particle model (black line) as compared to the best fitting profile using the Chamberlain model (red line). In the figure, blue lines indicate at which altitudes the optical depth between the detector and the emission altitude become unity, hence the exosphere becomes opaque for radiation in the line center. The shaded area indicates the altitude range of HDAC during the T_9 flyby.

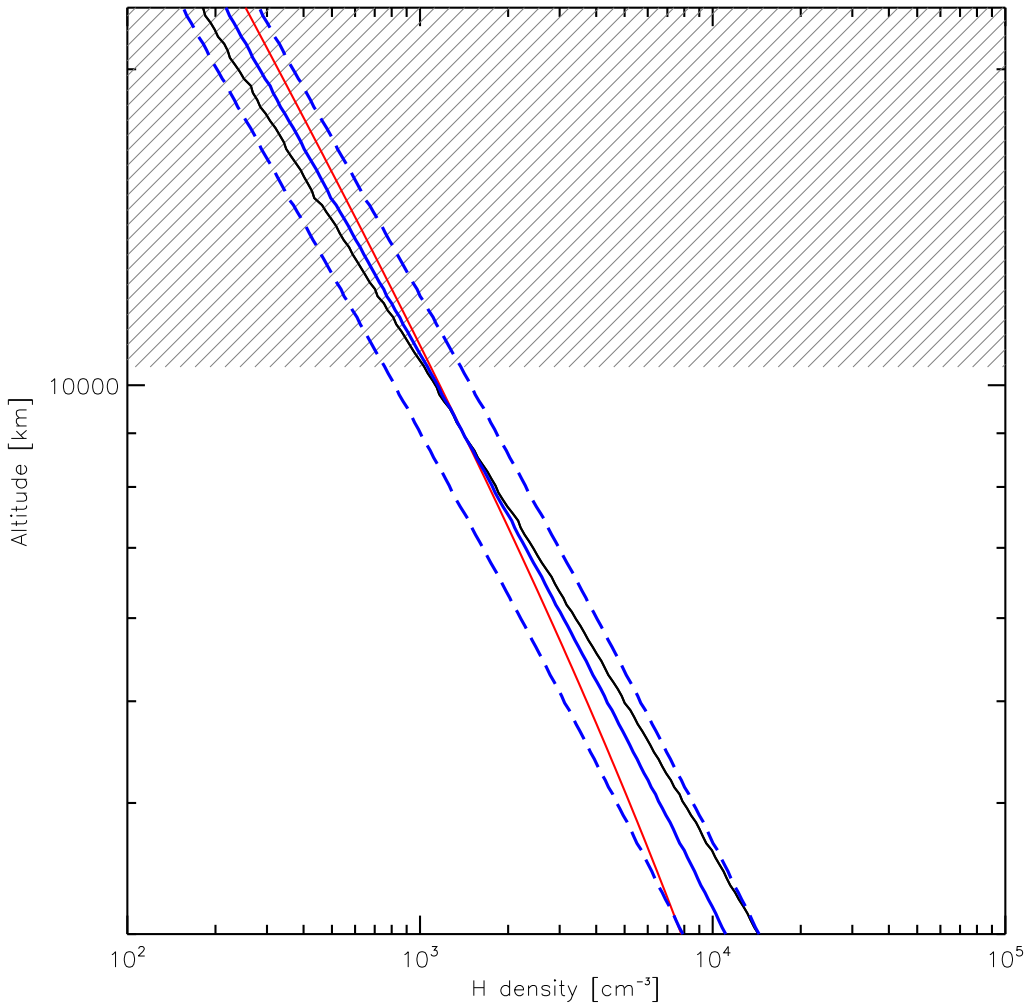

Fig. 9.5: Average density profile of both best fitting profiles (blue solid line). As a comparison also the Particle model distribution (black solid line) as well as the Chamberlain distribution (red solid line) is shown The error bar of this fit is indicated by long-dashed blue lines. The shaded area indicates the altitude range of HDAC during the T_9 flyby.

The simulated signals in photometer mode as well as when the H cell was switched on, yield a difference to the measured data of about $(12,000 \pm 1,000)\,\mathrm{cts\,s^{-1}}$ (see Figures 9.6 and 9.7). Considering the sensitivity of the detector ($S_{\mathrm{LyA}} = (29 \pm 3)\,\mathrm{cts\,s^{-1}\,R^{-1}}$, see chapter 4), one obtains a difference of about $413^{+90}_{-70}\,\mathrm{R}$. The background signal in the HDAC measurements is not reduced as planned by the oxygen cell, allowing radiation to be detected in a broad wavelength range. The wavelength range from 175 nm to 240 nm is of main importance, since at this wavelength the UV output of the sun begins to increase rapidly with increasing wavelength (see Figure 4.8). The oxygen cell was originally included to act as a filter, absorbing radiation redwards of 175 nm. Also, Lyman-α radiation from the local interstellar

medium contributes to the background signal. At the end of the encounter, Saturn was within the FOV of Titan, becoming the main contributor to the background signal.
Correcting the HDAC observations for the additional background signal yields a comparable behavior for measurement and simulation at the beginning of the encounter until closest approach (see Figure 9.8). Afterwards, the measured signal increases rapidly, whereas the simulated signal remains constant at about 1,400 cts s^{-1} (about 50 R). The increase in the measurement originates from limb measurements, with background radiation from Saturn being detected by HDAC. These background sources have not been considered in the simulations.

The simulated signal yields a count rate of about 5,000 cts s^{-1} at the beginning of the encounter, which corresponds to a Lyman-α brightness in the FOV of about 172^{+20}_{-16} R, when HDAC was looking at the sunlit side of Titan under a zenith angle of about 20° (cf. Figure 4.6). At the end of the encounter, the night side of Titan was in HDAC's FOV, yielding a brightness of about 43 ± 5 R.
From UVIS measurements using the FUV spectrometer during the T_B flyby in December 2004, Ajello et al. (2008) found a day side Lyman-α brightness of 208 R and a night side brightness of 80 R. These values have been determined during ingress observations from a distance of $1.63 \cdot 10^5$ km and during egress from a distance of $5.05 \cdot 10^4$ km (see Ajello et al. 2007 for a description of the observations).
The brightness of both the day and night side as inferred from the radiative transfer model, is comparable to measurements of Ajello et al. (2008) taking into account the different altitudes of both measurements: The FOV of HDAC covered only about 14% of Titan's disc at the beginning of the encounter (the HDAC FOV is 3°, whereas at the angle diameter of Titan was about 8°) and at the end HDAC performed limb scans. Furthermore, HDAC was not aligned with the Sun and Titan, but instead looked at Titan with a zenith angle of about 20° at the beginning of the encounter.

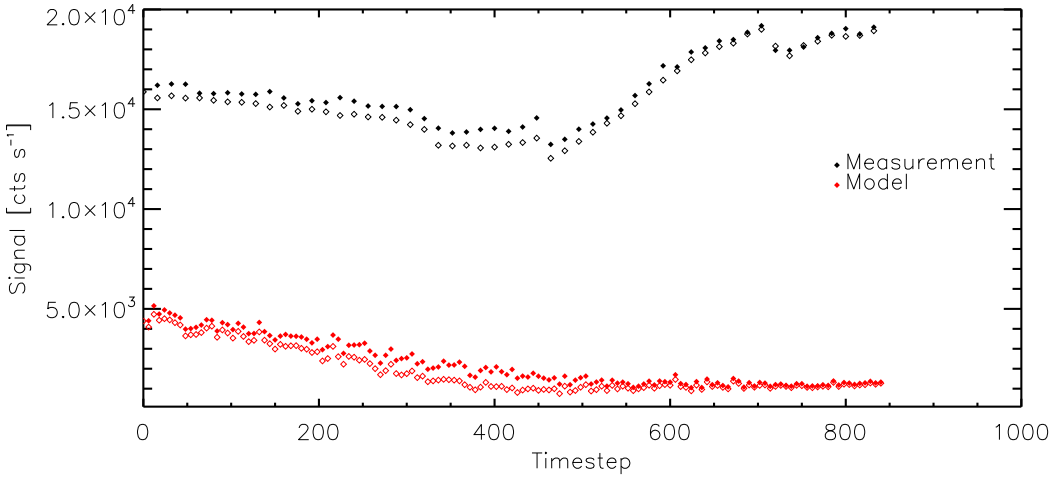

Fig. 9.6: Comparison of the HDAC measurements (black diamonds) with the simulation performed with the best fitting exobase parameters (red diamonds). Filled diamonds indicate data measured in photometer mode, whereas open diamonds are data measured when the H cell was taken into account.

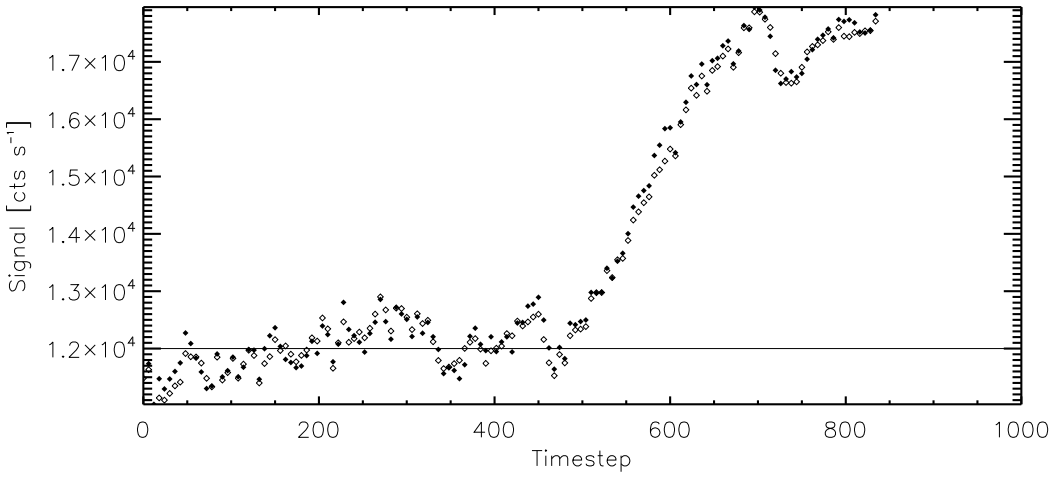

Fig. 9.7: Difference between measurement and simulation. The HDAC measurement has been interpolated with a spline fit, in order to compare measurement and simulation. As in Figure 9.6, filled diamonds indicate signals measured in photometer mode, whereas open diamonds indicate signals measured taking into account the H cell.

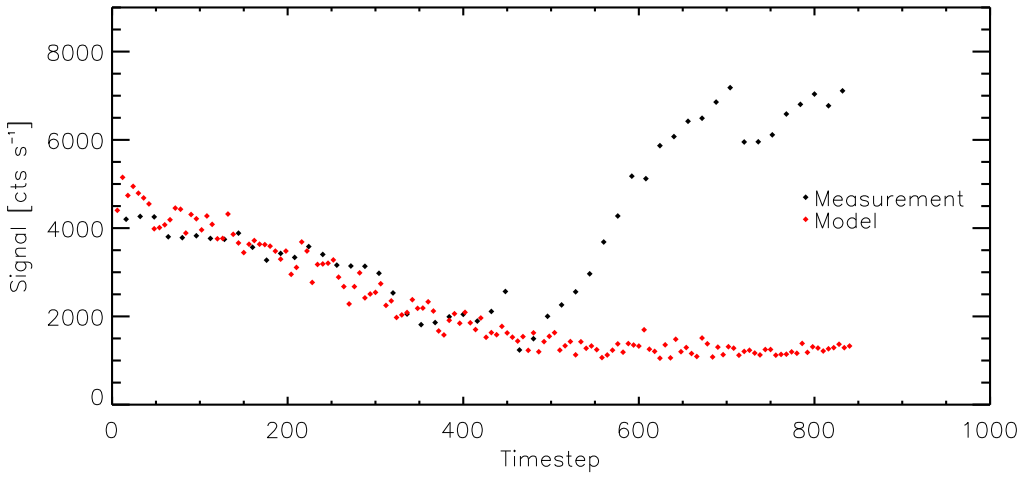

Fig. 9.8: Comparison of the signals as measured by HDAC (black diamonds, now corrected for background signal) and from the simulations (red diamonds). For clarity reasons, only the photometer measurements are shown.

9.2 Future Titan flybys

Based on this work, the HDAC instrument will be used again during two future flybys at Titan: The T_{66} will take place on January 28, 2010 whereas the T_{67} flyby will take place in May 04, 2010, respectively. This section hence focuses on these Titan flybys of the Cassini spacecraft. With the best fitting atomic hydrogen profiles obtained from the last section, the signal pattern for future flybys is estimated.

9.2.1 Flyby trajectories

Figure 9.9 shows the spacecraft trajectories during the three flybys. Here, the T_9 flyby trajectory is shown as the blue line, T_{66} by the green line and T_{67} by the red line. For calculations performed here it is assumed that HDAC will always look towards the center of Titan's disk since the exact viewing direction during the flybys has not yet been defined.

During the T_{66} encounter, Cassini will pass Titan on January 28, 2010 with a closest approach (C/A) distance of 10,065.4 km at 22:28:50 h (UTC; see Figure 9.9, green line as well as Figure 9.10). During the closest encounter Cassini will cross Titan at a latitude of -52.75° and a longitude of 297.1°.

The second flyby (T_{67} in the year 2010 is scheduled for May, 04 with a C/A distance to Titan's center of 10,036.9 km at 15:50:39 h (see Figure 9.9, blue line). Note that the orbital parameters (altitude and Doppler shift) are almost identical to the T_{66} and thus are not shown in an additional figure.

During C/A, Cassini will cross Titan at a latitude of 0° and a longitude of 240.4°. Cassini will start observations on the night side of Titan and end up with observations of the day side, contrary to T_9 and T_{66}.

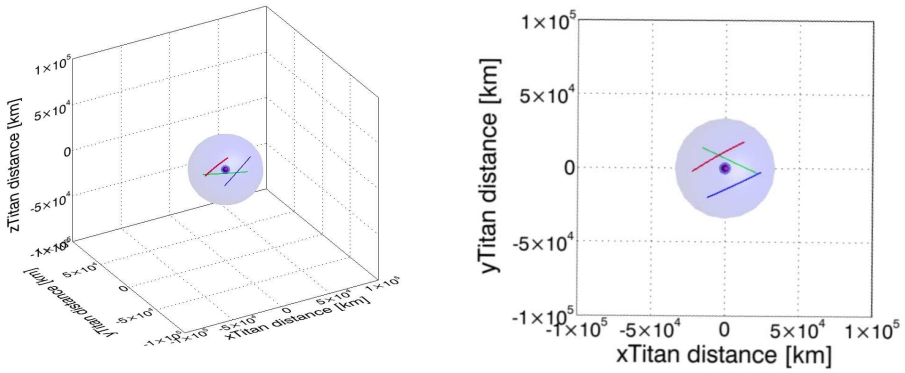

Fig. 9.9: Spacecraft trajectories during T_9 (blue), T_{66} (green) and T_{67} (red). The Sun is always centered at ($x \rightarrow \infty$, y=0, z=0. The left plot shows a 3D illustration with the blue globes representing the upper model boundary and the lower model boundary, whereas Titan is shown as the red sphere in the center of the plot. The right plot illustrates the trajectories as seen from top (x-y-plane). Note that during the T_{67} flyby, Cassini will approach Titan from the night side, contrary to T_9 and T_{66}

.

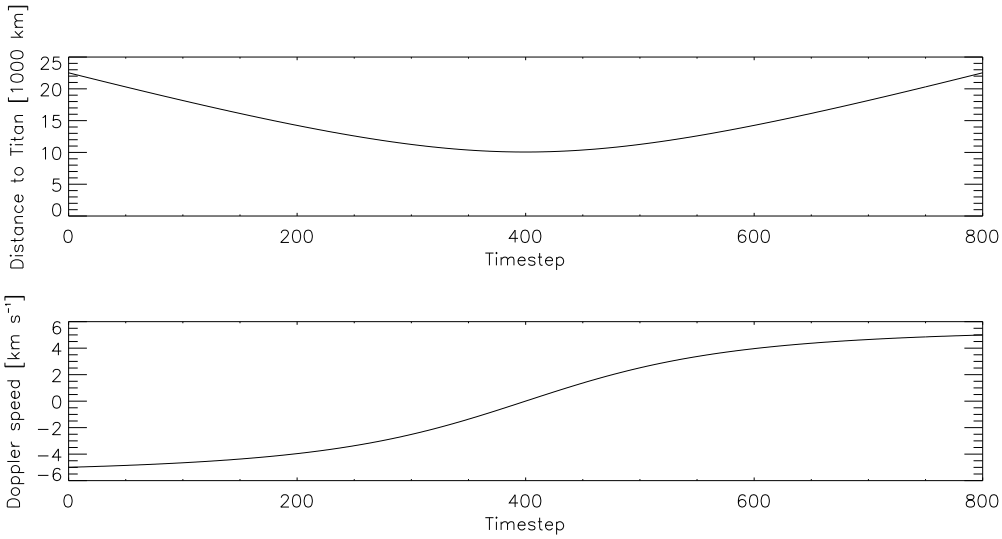

Fig. 9.10: Precalculated parameters for the T_{66} encounter of Cassini with Titan, assuming that HDAC looks always towards the center of Titan's disc: Uppermost plot shows the distance to Titan, the second plot shows the Doppler velocity. One timestep corresponds to 9 s, starting at 21:28:50 h UTC with the beginning of the observations.
Note that the orbital parameters of the T_{67} flyby are almost identical to T_{66} and thus are not shown in an additional figure.

9.2.2 Related radiative transfer calculations

Radiative transfer calculations are performed for both planned flybys using the best fitting model parameters obtained in section 9 using the Particle model. During the T_{66} and T_{67} flybys, Titan will have a heliocentric distance of 9.46 and 9.48 AU, respectively. For the radiative transfer calculations presented hereafter, the solar Lyman-α flux is assumed to be the same as during the T_9 encounter in 2005. This assumption is justified by extrapolating the solar spectral irradiation time series for Lyman-α radiation as shown in Figure 6.3. The corresponding factors, the output of the radiative transfer calculations has to be multiplied with (cf. section 6.4), are $\mathcal{N} = N_{\text{incoming}}/N_{\text{Model}} = 1.43 \cdot 10^{20}$ and $1.42 \cdot 10^{20}$ for T_{66} and T_{67}, respectively. For the calculations it is assumed that HDAC will always look in the direction of Titan's center. The calculations are performed in the time interval one hour before the closest encounter until one hour afterwards. The spacecraft trajectory is obtained using SPICE (see section 6.3.3).

The measured signal during the T_{66} flyby (see figure 9.11, green diamonds) at the beginning of the encounter (here: one hour before the closest approach) will be about 4,000 cts within an HDAC integration time of 1 s. The signal will then decrease to a value of about 500 cts during closest approach (timestep 400) and remain constant during the departure of HDAC.
The signal that will be measured during the T_{67} flyby is rather different to the earlier encounters (see figure 9.11, red diamonds), since Cassini approaches Titan from the night side. The signal at the beginning of the encounter will be around 400 cts s^{-1}. After timestep 350, HDAC begins to look on the terminator of Titan and furthermore it will observe the sunlit side of Titan. The signal will then increase to about 4,000 cts s^{-1}.
Note that the closest encounter altitudes of the both future flybys are considerably lower than during the T_9 flyby, with an altitude of about 7,500 km for T_{66} and T_{67} compared to 10,411 km. Thus, the day and night side brightness is not comparable, but will be much lower than estimated during the T_9 flyby due to the afore mentioned geometric reasons.

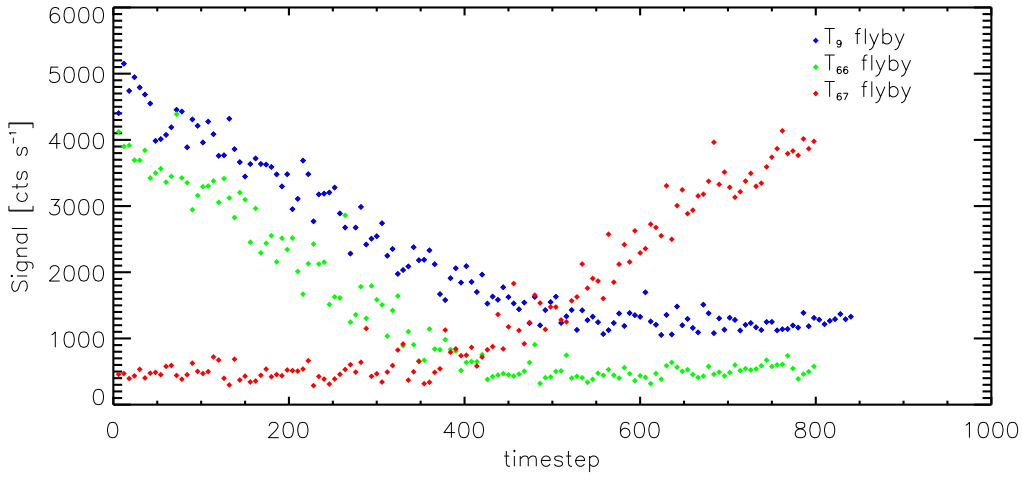

Fig. 9.11: Estimated signal measured by HDAC during the three encounters considered in the text, using the best fitting exospheric parameters for the radiative transfer calculation. For the calculations it is assumed that HDAC always points towards the center of Titan's disc. Note that Cassini will approach Titan from the night side during the T_{67} encounter.

Due to the lower flyby altitude, the difference signals in Figure 9.12 show a lower Lyman-α emission compared to the T_9 encounter (blue diamonds in the figure): During T_{66}, the signal is predicted to remain constant at a level of about 200 cts and decreases to zero after the closest encounter (timestep 400). The difference signal during the T_{67} will be zero at the beginning of the observations due to the afore mentioned flyby geometry, increasing to about 300 cts when HDAC crosses the terminator and looks onto the sunlit side of Titan.

Since the closest approach altitudes of both future flybys are considerably lower compared to the T_9 flyby, the HDAC instrument will be more sensitive to emissions from lower altitudes: The optical depth in the line center becomes unity in the altitude range from (3,100–3,900) km in both flybys, when the Particle model density distribution is applied or in the altitude range from (2,500–3,800) km, in case of application of the Chamberlain model distribution.

From the analysis of the HDAC data measured during the T_9 encounter, a potential undersampling problem was identified (see section 4.5.3) which should be considered for both future flybys: The H cell will be modulated by a voltage pattern of [0707070707070707] (cf. 4.5.2), i.e. the cell will be switched on and off alternately, contrary to the T_9 flyby where the H cell was switched on for the whole sequence except for one measurement in

photometer mode at the beginning of the sequence. This will presumably avoid the undersampling problem discovered and specified by this work and the noise in the signal will be decreased. Due to the known problems with the afore-mentioned D cell, this cell will not be used for those flybys.
The combined effect of a lower flyby altitude and a lower error in the measurements, the density and temperature structure of Titan's exosphere can be determined much more precisely. Together with the results of this work, providing the density structure above about 3,500 km, a realistic density distribution can be determined. Thus, judging which density distribution model describes the atomic hydrogen in Titan's exosphere the best can be performed, and the exobase density can be determined much more accurately. Since the exobase density was so far determined only by photochemical models (except for one measurement in 1981), this in turn will provide useful information also for such models and in addition to models about the loss of atomic hydrogen from Titan's atmosphere, thus the evolution of Titan.

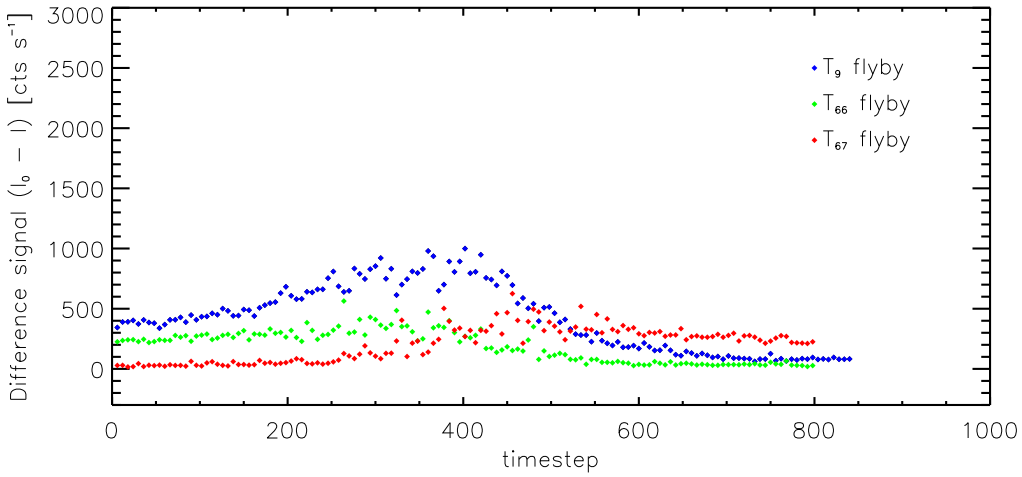

Fig. 9.12: Calculated difference signal between photometer mode measurements and H cell on measurements signal during the T_{66} (green diamonds) and T_{67} (red diamonds) encounters in 2010. As a comparison the difference signal during the T_9 flyby is shown in blue diamonds. Note that Cassini will approach Titan from the night side during the T_{67} encounter.

10. SUMMARY AND CONCLUSIONS

This work provides for the first time information on the distribution of atomic hydrogen in the upper exosphere of Titan. Based on measurements by the Hydrogen Deuterium Absorption Cell (HDAC) instrument aboard the Cassini orbiter, Monte Carlo radiative transfer calculations were performed in order to simulate the measurements. HDAC was originally designed to directly determine the D/H ratio of the atmospheres of Saturn and Titan by measuring the relative abundance of atomic deuterium and hydrogen from their Lyman-α emission at 121.533 nm and 121.567 nm, respectively. Furthermore the response of Titan's exosphere on varying exospheric densities of atomic hydrogen as well as on the exospheric temperature was investigated in detail.

Although HDAC's original purpose could not be achieved by the mission, data measured during the T_9 encounter in December 2005 was used to infer the distribution of atomic hydrogen in Titan's upper exosphere. Furthermore the exospheric temperature could be determined.

Based on the results of this work, HDAC will be used again during the T_{66} and T_{67} flybys in 2010, presumably providing more accurate measurements for the determination of densities and temperatures in Titan's exosphere.

10.1 Summary

Based on measurements performed by the HDAC instrument aboard the Cassini orbiter during the 9^{th} encounter with Titan ("T_9") in December 2005, this work aimed at simulating the measured signal. Exospheric densities and temperatures in the range of literature value were found, as summarized below. Atomic hydrogen exobase densities so far have only been obtained from photochemical models, except for one measurement from Voyager 1. This work thus provides additional information on Titan's exosphere using satellite measurements.

Since the distribution of atomic hydrogen is unknown in Titan's exosphere, two different exospheric density models have been applied to a spherical

model of Titan's exosphere in order to calculate the distribution throughout the model boundaries considered in this work. A static approach from Chamberlain (1963) was used (hereafter referred to as the "Chamberlain model"), which applies the Liouville theorem and takes into account different particle trajectories. The second model used (hereafter referred to as the "Particle model") is a dynamic approach from Wurz and Lammer (2003), which uses the Monte Carlo method to follow single particles released from the exobase with velocities obeying the Maxwell-Boltzmann distribution. Both models require the exobase density and temperature as input parameters.

For the purpose of this work the radiative transfer through the exospheric model including multiple scattering was solved using the Monte Carlo method. The radiative transfer model considers atomic hydrogen as the scattering medium, whereas methane acts as an effective absorber of Lyman-α radiation especially in the lower exosphere. The scattering direction was assumed to be isotropic and non-coherent scattering was treated. An isothermal temperature profile was assumed for the radiative transfer calculations. The Monte Carlo radiative transfer model has been validated in the single scattering limit against a simple analytical radiative transfer model, in which only single scattering was assumed and the scattering was treated coherently.

In order to fit the data measured by HDAC, a parameter study was performed using the atomic hydrogen exobase densities as well as exospheric temperatures found in the literature. Furthermore the statistical significance and stability of the results against the number of model photons was investigated. The parameter variation has shown that the emitted Lyman-α radiation strongly depends on the atomic hydrogen density in the exosphere. Varying the exospheric temperature, the simulated signal however shows only a minor effect (compared to the effect of the density variation). This effect is predominantly visible at the beginning of the encounter as a signal increase, when increasing the temperature.

A least-squares fit to the data measured by HDAC was applied using radiative transfer calculations performed with different parameter combinations of exobase density and temperature.

Comparison with the HDAC data showed that radiative transfer calculations using both density distribution models are able to fit the measured data: Using the Chamberlain model for the calculation of exospheric densities, a best fitting exobase atomic hydrogen density of $n_{\mathrm{H}} = (2 \pm 0.5) \cdot 10^4\,\mathrm{cm}^{-3}$ and

an exospheric temperature of (175±25) K is needed in order to fit the measurement. However, when using the Particle model, a much higher exobase density of $n_{\mathrm{H}} = (9 \pm 1) \cdot 10^4\,\mathrm{cm}^{-3}$ and again an exospheric temperature of (175±25) K is necessary to fit the measured data. Note that the best fitting profiles of both models differ mainly close to the exobase: The density decreased much faster with height for the Particle model profile when compared to the Chamberlain profile. At high altitudes above about 3,500 km nevertheless both models feature comparable densities. The uncertainty of the inferred values arise from a strong noise pattern in the HDAC measurement, which is caused by an undersampled signal.

Detailed calculations have shown that the HDAC measurements are sensitive only to altitudes from 3,500 km up to the spacecraft altitude. This is well above the exobase altitude of 1,500 km. The simulated signal calculated using the best fitting parameters for both exospheric density models do not differ. Thus, any distinct judgement is anticipated, as to whether one density distribution model fits the data better than the other one - the atomic hydrogen density close to the exobase could not be inferred by the measurement during the T_9 flyby.

However, since both best fitting atomic hydrogen density profiles are comparable within about 25% above altitudes of 3,500 km. Thus, for the first time, the distribution of atomic hydrogen in the upper exosphere could be determined within the measurement uncertainties.

However, the afore mentioned best fitting exobase parameters that are required as input parameter for both exospheric distribution models are in the range of values published in the literature. The exospheric temperatures found are comparable to measurements from de La Haye et al. (2007a), which used the Ion Neutral Mass Spectrometer (INMS) aboard the Cassini spacecraft as well as to measurements performed by D. Shemansky (priv. com.), who used the "Ultraviolet Imaging Spectrograph" (UVIS) aboard Cassini. The exospheric density found using the Chamberlain model density distribution is lower than measurements performed by Voyager 1 and also lower than recent photochemical model results. When using the Particle model the inferred density is mostly comparable with recent model results.

Based on the results of this work, HDAC will be used again during two flybys in 2010. Having identified the undersampling as the main source of uncertainties in the measurements of the T_9 encounter, a different measurement strategy will be used during these future flybys. Thus, these flybys will perhaps provide a more accurate determination of exospheric atomic hydrogen

densities and exospheric temperatures.
Radiative transfer calculation for these two flybys have also been performed in this work. These flybys take place at lower altitudes, compared to the T_9 encounter, allowing to sense the exosphere at lower altitudes. Together with the results found from this work, the exospheric density structure can thus be determined more accurately, providing useful information for photochemical, as well as for evolutionary Titan models.

10.2 Conclusions

- HDAC T_9 measurements can be described with two different density distribution models applied to Titan.
- Lyman-α radiation scattered in Titan's exosphere strongly depends on the density, which might change during high solar activity.
- Exospheric temperatures have only a minor effect on the emitted radiation, compared to the response on density variations.
- HDAC measurements can be used in order to determine the distribution of atomic hydrogen in Titan's exosphere, as well as the exospheric temperature.
- The HDAC measurement features strong undersampling problems.
- Densities provided by both exospheric models differ by about 25% in the altitude range HDAC is sensitive for, due to the undersampling problem.
- Exobase densities inferred are comparable to values determined by recent photochemical models
- Best fitting exospheric temperatures are consistent with recent measurements by other instruments aboard the Cassini spacecraft.
- There is a need for more accurate measurements during future flybys in order to help in judging which density profile better fits the data. Furthermore the exospheric temperatures can be determined much more precisely. The undersampling problems during the T_9 measurement can be avoided in future measurements.
- Based on this work, HDAC will be used again during the T_{66} and T_{67} flyby in 2010.

11. OUTLOOK

This work has focussed on measurements performed with the modulated hydrogen cell aboard HDAC only. Although the amount of deuterium in the D cell is not known, the amount of hydrogen contaminating the D cell is well determined. So far, calculations with an increased optical depth in order to take into account the absorption of both cells (with the additional optical depth provided by atomic hydrogen in the D cell) cannot reproduce the signal measured, when both cells are switched on.

For this reason, the radiative transfer model presented in this work might be expanded in order to include the resonance scattering of deuterium. With literature values of D/H determined from other instruments, the inferred atmospheric amount of deuterium might be used as an initial parameter for the radiative transfer calculations in order to calibrate the D cell. Due to undersampling problems during the T_9 encounter this will be a challenging task though. If however this is successfully done and the amount of Deuterium can be determined in the D cell, HDAC might be used again during the "Solstice Mission" of Cassini beginning in 2010 in order to determine the D/H ratio of the bodies observed.

However, the radiative transfer model will be enhanced in order to drop the assumption of an isothermal exosphere with a Maxwellian distribution of velocities. For this purpose, the velocities obtained from the Particle model could be used in the calculations and the direction of the photons with respect to the the direction of the escaping hydrogen atoms will be taken into account.

Furthermore, the number of photons might be increased significantly in order to lower the statistical errors. Together with the analysis of the HDAC measurements performed in this work, the future flybys in 2010 will provide much more accurate data and the radiative transfer model should hence be improved in this respect.

Since HDAC continuously measures in photometer mode, these measurements might be used for the analysis of other bodies, Cassini has passed and that were in the FOV of HDAC. Although doing this, the Lyman-α line shape cannot be investigated in detail, however other useful information might be

inferred. The removal of the background is at this point the most challenging task, which might be solved by proper modeling of the contributing background signals.

Beyond the comparisons with HDAC data, the exospheric and radiative transfer model might be easily modified to calculate the transfer of radiation through the exospheres of other bodies in the Solar System. For close-in planets, like Mercury, as well as for comets, the radiative transfer calculations require the proper treatment of radiation pressure. However with the model improvements indicated above this should be a relatively straightforward task.
Also the application to extrasolar planets is possible. Emissions of Lyman-α radiation from extrasolar giant planets have already been detected. Unfortunately, the planets where the Lyman-α line has been observed orbit their central star in a very close orbit (closer than that of Mercury) and therefore they feature a strong hydrodynamic blow-off of hydrogen. The assumption of a spherical corona thus needs to be dropped and the radiation pressure must be taken into account properly. Also the exospheric density models must be improved in order to take into account the effect of hydrodynamic blow-off. The measurement principle of the HDAC instrument, however, can only be applied in the Solar System since the Doppler shift of the absorption compared to the emission from the body observed is only useable during close flybys. Applying this principle to extrasolar planet research is hence impossible. Furthermore, this kind of absorption cells might be used for close in flybys around comets. The determination of the D/H ratio of these objects would help in understanding the evolution of the Solar System.

APPENDIX

A. GLOSSARY

Clathrate - clathrates are a chemical substance consisting of a lattice of one type of molecule trapping and containing a second type of molecule. An example of a clathrate is a clathrate hydrate, a special type of gas hydrate in which a lattice of water molecules encloses molecules of a trapped gas.

Exosphere - transition region of the gravitationally bound atmosphere to free space. Within the exosphere, the mean free path of a particle is greater than its scale height. Thus, collisions between particles become negligible in this region.

Heterosphere - in the heterosphere (above the homopause) molecular diffusion is more important than eddy diffusion, hence each species has an individual scale height.

Hill sphere - the Hill sphere is the volume around an astronomical body (such as a planet) in which the gravitational attraction dominates over the gravitation of a larger body which it orbits.

Homosphere - within the homosphere the vertical transport is independent of molecular mass - one single scale height can be applied to characterize the vertical structure of the atmosphere. The homopause is the altitude at which molecular diffusion replaces eddy diffusion as the dominant vertical transport mechanism.

Hydrocarbon - hydrocarbons are organic compounds consisting entirely of hydrogen and carbon (C_xH_y).

Ionosphere - the ionosphere is the part of the atmosphere that is ionized by solar radiation. The ionosphere is coupled to both the magnetosphere and the neutral atmosphere.

Nitrile - nitriles are any organic compound, where the carbon atom and the

nitrogen atom are triple bonded together ($C_xN_yH_z$).

Mesosphere - the mesosphere is the layer of the atmosphere that is directly located above the stratosphere and directly below the thermosphere. The mesosphere is predominantly characterized by its thermal structure.

Polycyclic aromatic hydrocarbon - polycyclic aromatic hydrocarbons (PAHs) are chemical compounds that consist of fused aromatic rings and do not contain heteroatoms or carry substituents.

Polyyne - polyynes are a group of organic compounds with alternating single and triple bonds, for example diacetylene C_4H_2.

Rayleigh - One rayleigh (1 R) is defined as a column emission rate of 10^{10} photons per square meter per column per second. Note that a rayleigh is an apparent emission rate, as no allowances have been made for scattering or absorption. The relationship between radiance, L, (in units of photons per square meter per second per steradian) and I (in units of rayleighs) is simply $L = I \cdot 10^{10}/(4\pi)$.

Stratosphere - the stratosphere is a region of intense interactions among radiative, dynamical, and chemical processes, in which horizontal mixing of gaseous components proceeds much more rapidly than vertical mixing.

Thermosphere - the thermosphere is the part of the atmosphere which absorbs the Sun's extreme ultraviolet radiation and hence the temperatures increases steadily with altitude.

Tholin - tholins are nitrogen-rich organic substances produced by the irradiation of gaseous mixtures of nitrogen and methane.

Troposphere - the troposphere is the lowest layer of the atmosphere and is characterized by vertical mixing. The temperature of the troposphere generally decreases as altitude increases.

B. LIOUVILLE'S EQUATION

A detailed introduction in obtaining the distribution of particles within the exosphere from Liouville's equation can be found in (Chamberlain, 1963). The important points of his work are reviewed here.

In the exospheric layers, where collisions are by definition rare, the spatial and momentum distribution is governed by Liouville's equation, which is equivalent to Boltzmann's equation without collisions. Using the continuity equation

$$\frac{\partial N}{\partial t} + \nabla \cdot (N\mathbf{v}) = 0, \tag{B.1}$$

with N being the particle density and $\mathbf{v}$ the mean velocity. A large group of particles distributed over spatial (q_i) and momentum (p_i) coordinates in 6-dimensional phase space according to some function $f(q_i, p_i)$ have a "density" in phase space of $f(q_i, p_i)$. Replacing the velocity component by $\dot{q}_i$ and $\dot{p}_i$ Liouville's equation is then

$$\frac{\partial f}{\partial t} + \sum_{i=1}^{3} \left[\frac{\partial}{\partial q_i}(f\dot{q}_i) + \frac{\partial}{\partial p_i}(f\dot{p}_i) \right] = 0 \tag{B.2}$$

The particles are subject to the equations of motion, in this case the particles are under the influence of gravitation. In Hamiltonian form, one has

$$\dot{q}_i = \frac{\partial \mathcal{H}}{\partial p_i} \qquad \dot{p}_i = -\frac{\partial \mathcal{H}}{\partial q_i}, \tag{B.3}$$

where $\mathcal{H} = \mathcal{H}(q_i, p_i)$ is the Hamiltonian function which expresses the total energy in terms of q_i and p_i. Expanding the derivatives and using equation B.3 to eliminate $\partial\dot{q}/\partial q = -\partial\dot{p}/\partial p$ gives

$$\frac{\mathrm{d}f}{\mathrm{d}t} \equiv \frac{\partial f}{\partial t} + \sum_{i=1}^{3} \left[\frac{\partial f}{\partial q_i}\dot{q}_i + \frac{\partial f}{\partial p_i}\dot{p}_i \right] = 0 \tag{B.4}$$

The term on the left is the total derivative to be taken along the path in phase space followed by a closed element of "volume" as it "moves" according to the equations of motion. Liouville's theorem thus states that the density in phase space remains constant along a dynamical trajectory.

As an example, Liouville's theorem is applied to the density and velocity distribution in an exosphere. An isotropic Maxwellian distribution of velocities

for temperature T_e is assumed just below the critical level, which is at radial distance r_e from the center of the planet, and a total density $N(r_c) = N_c$. For spherical symmetry and time independence ($\partial f/\partial t = 0$), equation B.4 is

$$\frac{\partial f}{\partial r}\frac{\mathrm{d}r}{\mathrm{d}t} = -\frac{\partial f}{\partial p_r}\frac{\mathrm{d}p_r}{\mathrm{d}t}, \tag{B.5}$$

where p_r is the radial component of momentum and r is measured from the center of the planet. Adopting a Maxwellian motion at the exobase and considering the Hamiltonian in spherical coordinates as well as the equations of motion, one finally finds the radius dependent by integration over all momentum space

$$N(r) = \int f(q_i, p_i)\mathrm{d}^3 p_i = N_c \exp(-(\lambda_c - \lambda)), \tag{B.6}$$

with the absolute value of the potential energy in units of $k_B T_c$

$$\lambda(r) \equiv \frac{GMm}{k_B T_c r} = \frac{v_{\mathrm{esc}}^2}{U^2}, \tag{B.7}$$

where $v_{\mathrm{esc}}^2 = 2GM/r$ is the parabolic escape velocity and $U^2 = 2k_B T_c/M$ is the most probable Maxwellian velocity.

The derivation of equation B.6 from Liouville's equation is a direct consequence of the Maxwellian distribution holding even in the region free of collisions, provided the momenta do extend over all possible values. Hence the mean energy per atom is unchanged and the barometric law naturally emerges.

All this depends, however, on having the entire range of molecular momenta allowed. At substantial distances above the critical level this is not the case and the barometric law breaks down. If strictly true, equation B.6 would predict a finite density and pressure is achieved as $r \to \infty$ (and $\lambda \to 0$). To treat the density distribution accurately it is necessary to examine the individual particle orbits in the corona with the kinetic theory. Chamberlain (1963) therefore introduces an partition function ζ, describing the orbits of the particles released at the exobase and equation B.6 is then

$$N(r) = N_c \exp(-(\lambda_c - \lambda)) \cdot \zeta(\lambda). \tag{B.8}$$

C. RADIATION PRESSURE

Radiation pressure can be treated as an uniform anti-solar acceleration a, represented by a potential $m \cdot a \cdot r \cdot \cos(\chi)$ superposed on the planetary gravitational potential GMm/r. Here G is the gravitational constant, M the mass of Titan, m the hydrogen atom mass, r the planetocentric distance, and χ the solar zenith angle. Radiation pressure occurs via the resonant scattering of solar Lyman-α photons, which impart a momentum $h\nu/c$ per photon into the antisolar direction. The radiation pressure acceleration is then given by

$$p = g_{\nu'\nu''}\frac{h\nu}{mc}, \tag{C.1}$$

where g is the photon scattering coefficient (Chamberlain and Hunten, 1987). The photon scattering coefficient is expressed by Shefov (1984) as:

$$g_{\nu'\nu''} = w\frac{\lambda^3_{\nu',0}}{2hc^2}F_\lambda A_{\nu',0}\frac{A_{\nu'\nu''}}{\sum\limits_{\nu'} A_{\nu'\nu''}}, \tag{C.2}$$

where λ is the wavelength of the transition $(\nu', 0)$, A the probability of the spontaneous transition, and F_λ the radiation flux at the solar surface. Note that Shefov (1984) uses a similar equation as Chamberlain and Hunten (1987), (p.291). w is the dilution factor, defined by

$$w = \frac{1}{2}\left[1 - \sqrt{1 - (r_\odot/R)^2}\right], \tag{C.3}$$

where $r_\odot$ is the solar radius and R is the heliocentric distance. For Titan $w = 5.03 \cdot 10^{-8}$ and for solar Lyman-α radiation at the position of Titan (9.09 AU during the T_9 encounter), $g_{\nu'\nu''} = 2.78 \cdot 10^{-5}$ photon s^{-1} (Chamberlain and Hunten, 1987). One obtains a radiation pressure acceleration of $p = 9.062 \cdot 10^{-5}\,m\,s^{-2}$.

Setting this equal to the gravitational acceleration g

$$g = -\frac{MG}{r^2_{\mathrm{RP}}}, \tag{C.4}$$

and solving for the planetocentric distance r_{RP} one obtains r_{RP}=314,709 km or 122.21 R_{Titan}, which is far outside the exospheric model boundaries of this work (upper boundary is set to a distance to Titan's center of 32,575 km). Thus, the effect of radiation pressure on the hydrogen atoms in Titan's exosphere can be neglected within the model boundaries considered here.

D. SOURCE PHOTON GENERATION

In the Monte Carlo model presented here, the photons are injected at the upper boundary of a sphere. When creating photons with coordinates $(x, y, z) \in [r_{min}, r_{max}]$ uniformly distributed on a sphere, one would obtain an enhanced creation at the poles of the sphere. Since the photons should be created uniformly over the sphere, the cartesian coordinates need to be transformed to spherical coordinates. Thus, choosing three uniformly distributed variables $A_i \in [0,1], B_i \in [0,1], C_i \in [0,1]$ in cartesian coordinates (x, y, z), one is looking for the distribution in spherical coordinates (r, ϕ, θ), where $r_i \in [r_{min}, r_{max}]$, $\phi_i \in [0, 2\pi]$, and $\theta_i \in [0, \pi]$. The transformation reads:

$$\begin{aligned} x &= r\cos\phi\sin\theta \\ y &= r\sin\phi\sin\theta \\ z &= r\cos\theta \end{aligned} \tag{D.1}$$

The Jacobian then reads:

$$\frac{\partial(x,y,z)}{\partial(r,\phi,\theta)} = r^2 sin\theta \tag{D.2}$$

Since

$$1 = \int_{shell} w(x,y,z)\,\mathrm{d}x\,\mathrm{d}y\,\mathrm{d}z \Rightarrow w(x,y,z) = \frac{3}{4\pi}\left[r_{max}^3 - r_{min}^3\right]^{-1}, \tag{D.3}$$

and

$$w(x,y,z)\,\mathrm{d}x\,\mathrm{d}y\,\mathrm{d}z = Q(r,\phi,\theta)\,\mathrm{d}r\,\mathrm{d}\phi\,\mathrm{d}\theta, \tag{D.4}$$

one can write

$$Q(r,\phi,\theta) = Q_1(r)Q_2(\phi)Q_3(\theta) = r^2\sin\theta\frac{3}{4\pi}\left[r_{max}^3 - r_{min}^3\right]^{-1}. \tag{D.5}$$

Then,

$$Q_1(r) = q_1 \cdot r^2 \;\rightarrow\; q_1 = \left[\int_{r_{min}}^{r_{max}} r^2\mathrm{d}r\right]^{-1} = \left[\frac{1}{3}(r_{max}^3 - r_{min}^3\right]^{-1} \tag{D.6}$$

$$Q_2(\phi) = q_2 \cdot 1 \;\rightarrow\; q_2 = \left[\int_0^{2\pi} 1\mathrm{d}\phi\right]^{-1} = \frac{1}{2\pi} \tag{D.7}$$

$$Q_3(\theta) = q_3 \cdot \sin\theta \;\rightarrow\; q_3 = \left[\int_0^{\pi} \sin\theta\mathrm{d}\theta\right]^{-1} = \frac{1}{2}. \tag{D.8}$$

Hence,

$$
\begin{aligned}
A = \int_0^A 1\mathrm{d}a &= \int_{r_{min}}^{F(A)} Q_1(r)\mathrm{d}r = \left[r_{max}^3 - r_{min}^3\right]^{-1} \cdot \left([F(A)]^3 - r_{min}^3\right) \\
&\rightarrow F(A) = \sqrt[3]{A\,(r_{max}^3 - r_{min}^3) + r_{min}^3} \qquad \text{(D.9)} \\
B = \int_0^B 1\mathrm{d}b &= \int_0^{F(B)} Q_2(\phi)\mathrm{d}\phi = \frac{1}{2\pi}F(B) \\
&\rightarrow F(B) = 2\pi B \qquad \text{(D.10)} \\
C = \int_0^C 1\mathrm{d}c &= \int_0^{F(C)} Q_3(\theta)\mathrm{d}\theta = \frac{1}{2}(1 - \cos[F(C)]) \\
&\rightarrow F(C) = \arccos[1 - 2C]. \qquad \text{(D.11)}
\end{aligned}
$$

The desired transformation then reads

$$
A_i, B_i, C_i \in [0,1] \begin{cases} r_i = \sqrt[3]{C_i\,(r_{max}^3 - r_{min}^3) + r_{min}^3} \\ \phi_i = 2\pi B_i \\ \theta_i = \arccos[1 - 2C_i]. \end{cases} \qquad \text{(D.12)}
$$

In case of releasing photons form the surface of a sphere, $r_i = const. = R$, with R being the radius of the sphere. By using the above given transformation D.1 one gets equally distributed values for the initial coordinates on top of the sphere (x, y, z).

E. FLOW CHARTS OF THE MONTE CARLO RADIATIVE TRANSFER PROGRAMS

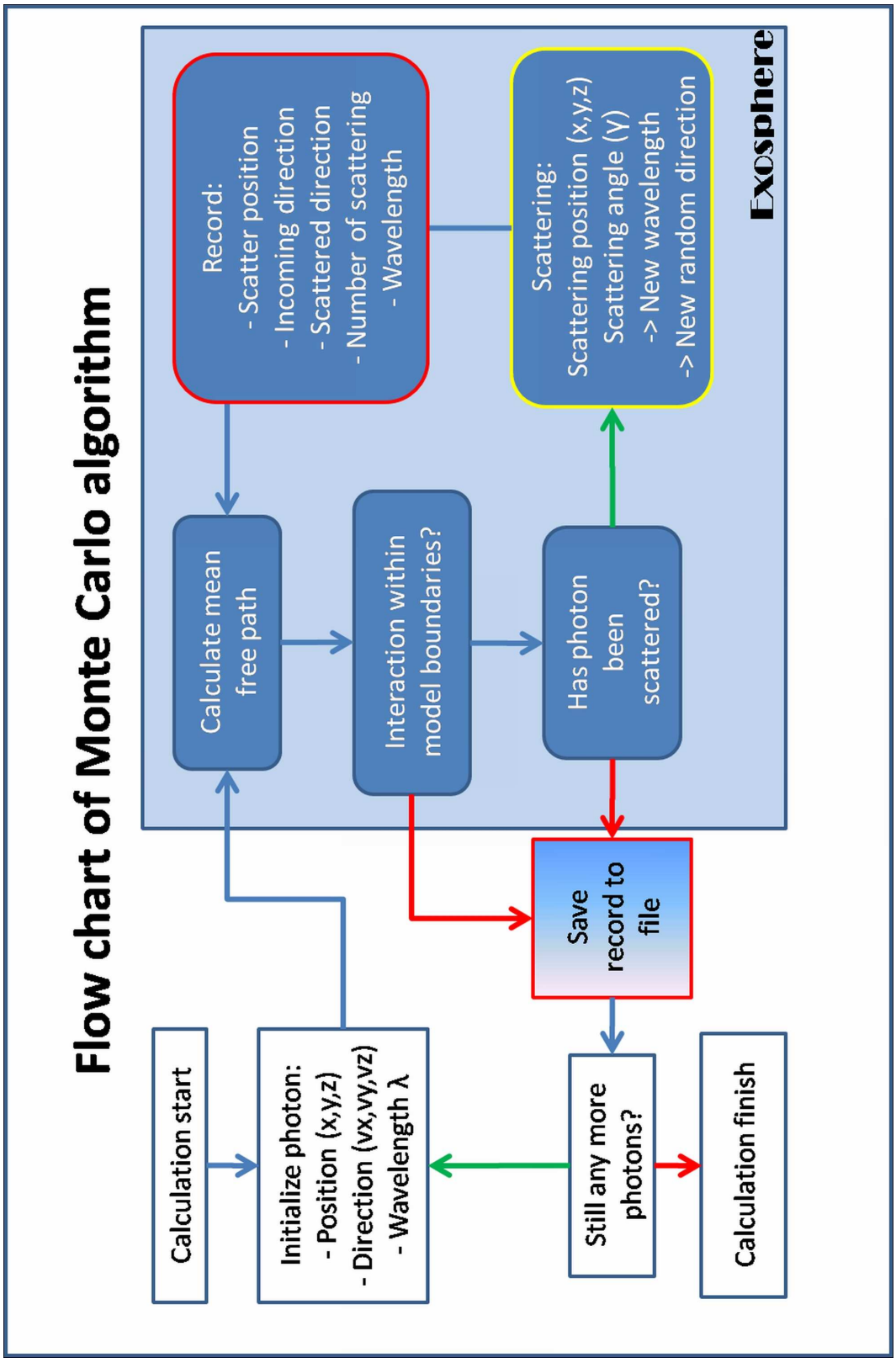

Fig. E.1: Flow chart of Monte Carlo radiative transfer algorithm used for this work. Using this algorithm, the scattering positions within the exosphere are determined.

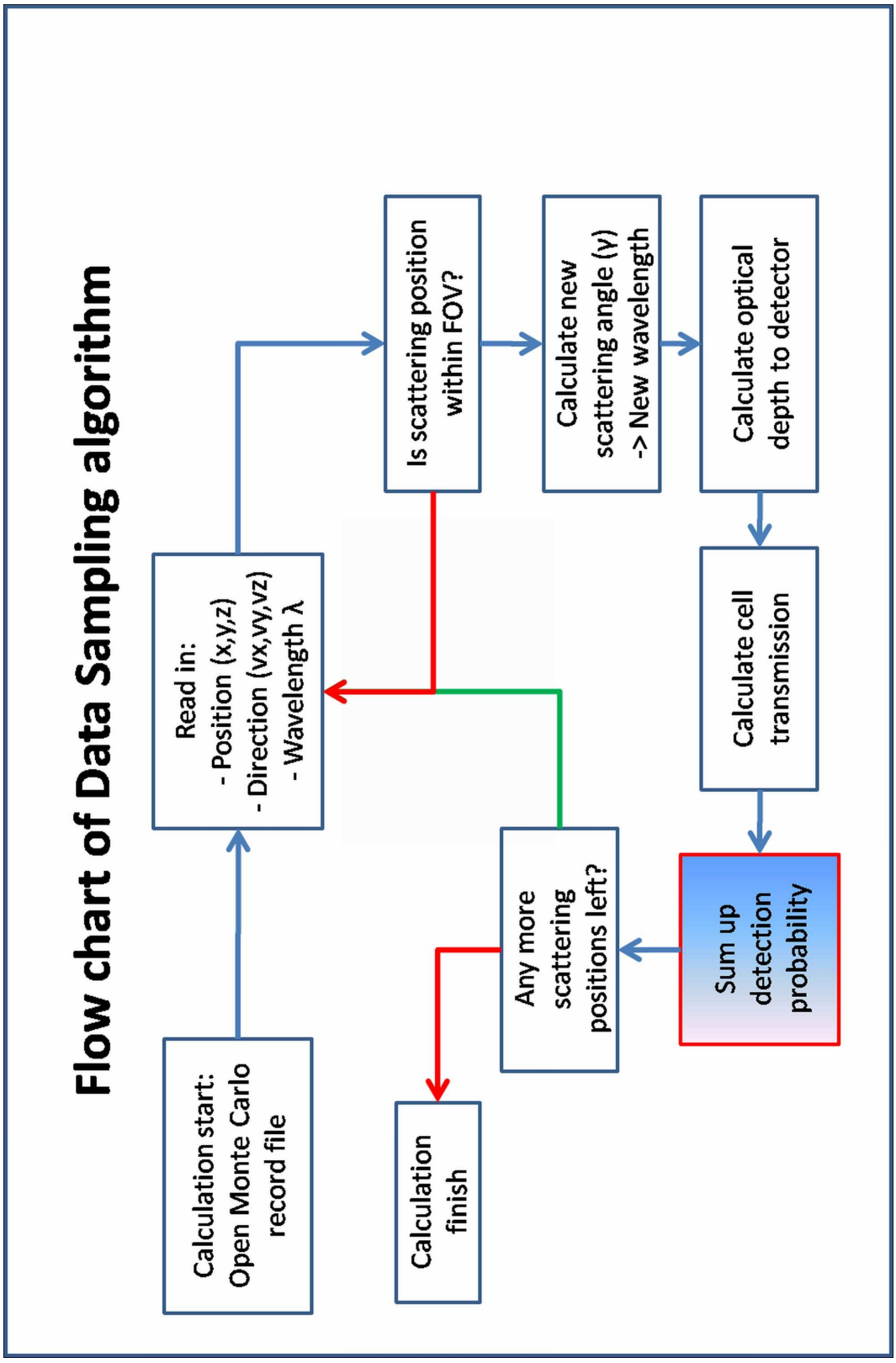

Fig. E.2: Flow chart of Data Sampling algorithm used for this work. Using the output of the Monte Carlo algorithm shown above, the Data Sampling model calculates the amount of photons that enter the detector.

BIBLIOGRAPHY

R. K. Achterberg, B. J. Conrath, P. J. Gierasch, F. M. Flasar, and C. A. Nixon. Titan's middle-atmospheric temperatures and dynamics observed by the Cassini Composite Infrared Spectrometer. *Icarus*, 194:263–277, March 2008.

J. M. Ajello, M. H. Stevens, I. Stewart, K. Larsen, L. Esposito, J. Colwell, W. McClintock, G. Holsclaw, J. Gustin, and W. Pryor. Titan airglow spectra from Cassini Ultraviolet Imaging Spectrograph (UVIS): EUV analysis. *Geophysical Research Letters*, 34:24204–+, December 2007.

J. M. Ajello, J. Gustin, I. Stewart, K. Larsen, L. Esposito, W. Pryor, W. McClintock, M. H. Stevens, C. P. Malone, and D. Dziczek. Titan airglow spectra from the Cassini Ultraviolet Imaging Spectrograph: FUV disk analysis. *Geophysical Research Letters*, 35, December 2008.

S. K. Atreya, E. Y. Adams, H. B. Niemann, J. E. Demick-Montelara, T. C. Owen, M. Fulchignoni, F. Ferri, and E. H. Wilson. Titan's methane cycle. *Planetary and Space Science*, 54:1177–1187, October 2006.

L. W. Avery and L. L. House. An Investigation of Resonance-Line Scattering by the Monte Carlo Technique. *Astrophysical Journal*, 152, May 1968.

S. J. Bauer. *The Astronomy and Astrophysics Encyclopedia.* Editor: S. P. Maran, Cambridge University Press, 1992.

J. L. Bertaux, J. Costa, E. Quémerais, R. Lallement, M. Berthé, E. Kyrölä, W. Schmidt, T. Summanen, T. Makinen, and C. Goukenleuque. Lyman-alpha observations of comet Hyakutake with SWAN on SOHO. *Planetary & Space Sciences*, 46:555–568, May 1998.

B. Bézard, C. A. Nixon, I. Kleiner, and D. E. Jennings. Detection of $^{13}CH_3D$ on Titan. *Icarus*, 191:397–400, November 2007.

M. K. Bird, M. Allison, S. W. Asmar, D. H. Atkinson, I. M. Avruch, R. Dutta-Roy, Y. Dzierma, P. Edenhofer, W. M. Folkner, L. I. Gurvits, D. V. Johnston, D. Plettemeier, S. V. Pogrebenko, R. A. Preston, and

G. L. Tyler. The vertical profile of winds on Titan. *Nature*, 438:800–802, December 2005.

A. H. Bouchez and M. E. Brown. Statistics of Titan's South Polar Tropospheric Clouds. *Astrophysical Journal*, 618:53–56, January 2005.

A. L. Broadfoot, B. R. Sandel, D. E. Shemansky, J. B. Holberg, G. R. Smith, D. F. Strobel, J. C. McConnell, S. Kumar, D. M. Hunten, S. K. Atreya, T. M. Donahue, H. W. Moos, J. L. Bertaux, J. E. Blamont, R. B. Pomphrey, and S. Linick. Extreme ultraviolet observations from Voyager 1 encounter with Saturn. *Science*, 212:206–211, April 1981.

P. D. Brown and T. J. Millar. Models of the gas-grain interaction - Deuterium chemistry. *Monthly Notices of the Royal Astronomical Society*, 237:661–671, April 1989.

E. D. Cashwell and C. J. Everett. *A practical manual on the Monte Carlo Method for random walk problems*. Pergamon Press, New York, 1959.

J. W. Chamberlain. Planetary coronae and atmospheric evaporation. *Planetary and Space Science*, 11:901, August 1963.

J. W. Chamberlain and D. M. Hunten. Theory of planetary atmospheres: an introduction to their physics and chemistry /2nd revised and enlarged edition/. *Orlando FL Academic Press Inc International Geophysics Series*, 36, 1987.

S. Chandrasekhar. *Radiative transfer*. editor: S. Chandrasekhar, New York: Dover, 1960.

R. Courtin. The spectrum of Titan in the far-infrared and microwave regions. *Icarus*, 51:466–475, September 1982.

A. Coustenis, B. Bezard, and D. Gautier. Titan's atmosphere from Voyager infrared observations. II - The CH_3D abundance and D/H ratio from the 900-1200/cm spectral region. *Icarus*, 82:67–80, November 1989.

A. Coustenis, A. Salama, E. Lellouch, T. Encrenaz, G. L. Bjoraker, R. E. Samuelson, T. de Graauw, H. Feuchtgruber, and M. F. Kessler. Evidence for water vapor in Titan's atmosphere from ISO/SWS data. *Astronomy & Astrophysics*, 336:85–89, August 1998.

A. Coustenis, A. Salama, B. Schulz, S. Ott, E. Lellouch, T. H. Encrenaz, D. Gautier, and H. Feuchtgruber. Titan's atmosphere from ISO mid-infrared spectroscopy. *Icarus*, 161:383–403, February 2003.

A. Coustenis, R. K. Achterberg, B. J. Conrath, D. E. Jennings, A. Marten, D. Gautier, C. A. Nixon, F. M. Flasar, N. A. Teanby, B. Bézard, R. E. Samuelson, R. C. Carlson, E. Lellouch, G. L. Bjoraker, P. N. Romani, F. W. Taylor, P. G. J. Irwin, T. Fouchet, A. Hubert, G. S. Orton, V. G. Kunde, S. Vinatier, J. Mondellini, M. M. Abbas, and R. Courtin. The composition of Titan's stratosphere from Cassini/CIRS mid-infrared spectra. *Icarus*, 189:35–62, July 2007.

A. Coustenis, D. E. Jennings, A. Jolly, Y. Bénilan, C. A. Nixon, S. Vinatier, D. Gautier, G. L. Bjoraker, P. N. Romani, R. C. Carlson, and F. M. Flasar. Detection of C_2HD and the D/H ratio on Titan. *Icarus*, 197: 539–548, October 2008.

A. Crespin, S. Lebonnois, S. Vinatier, B. Bézard, A. Coustenis, N. A. Teanby, R. K. Achterberg, P. Rannou, and F. Hourdin. Diagnostics of Titan's stratospheric dynamics using Cassini/CIRS data and the 2-dimensional IPSL circulation model. *Icarus*, 197:556–571, October 2008.

J. Cui, R. V. Yelle, and K. Volk. Distribution and escape of molecular hydrogen in Titan's thermosphere and exosphere. *Journal of Geophysical Research (Planets)*, 113(E12):10004–+, October 2008.

J. Cui, R. V. Yelle, V. Vuitton, J. H. Waite, W. T. Kasprzak, D. A. Gell, H. B. Niemann, I. C. F. Müller-Wodarg, N. Borggren, G. G. Fletcher, E. L. Patrick, E. Raaen, and B. A. Magee. Analysis of Titan's neutral upper atmosphere from Cassini Ion Neutral Mass Spectrometer measurements. *Icarus*, 200:581–615, April 2009.

C. de Bergh, B. Bezard, T. Owen, D. Crisp, J.-P. Maillard, and B. L. Lutz. Deuterium on Venus - Observations from earth. *Science*, 251:547–549, February 1991.

V. de La Haye, J. H. Waite, T. E. Cravens, A. F. Nagy, R. E. Johnson, S. Lebonnois, and I. P. Robertson. Titan's corona: The contribution of exothermic chemistry. *Icarus*, 191:236–250, November 2007a.

V. de La Haye, J. H. Waite, R. E. Johnson, R. V. Yelle, T. E. Cravens, J. G. Luhmann, W. T. Kasprzak, D. A. Gell, B. Magee, F. Leblanc, M. Michael, S. Jurac, and I. P. Robertson. Cassini Ion and Neutral Mass Spectrometer data in Titan's upper atmosphere and exosphere: Observation of a suprathermal corona. *Journal of Geophysical Research (Space Physics)*, 112:7309–+, July 2007b.

V. de La Haye, J. H. Waite, T. E. Cravens, I. P. Robertson, and S. Lebonnois. Coupled ion and neutral rotating model of Titan's upper atmosphere. *Icarus*, 197:110–136, September 2008.

P. Eberhardt, M. Reber, D. Krankowsky, and R. R. Hodges. The D/H and $^{18}O/^{16}O$ ratios in water from comet P/Halley. *Astronomy & Astrophysics*, 302, October 1995.

D. Ehrenreich, G. Tinetti, A. Lecavelier Des Etangs, A. Vidal-Madjar, and F. Selsis. The transmission spectrum of Earth-size transiting planets. *Astronomy & Astrophysics*, 448:379–393, March 2006.

C. Emerich, P. Lemaire, J.-C. Vial, W. Curdt, U. Schühle, and K. Wilhelm. A new relation between the central spectral solar H I Lyman α irradiance and the line irradiance measured by SUMER/SOHO during the cycle 23. *Icarus*, 178:429–433, November 2005.

L. W. Esposito, C. A. Barth, J. E. Colwell, G. M. Lawrence, W. E. McClintock, A. I. F. Stewart, H. U. Keller, A. Korth, H. Lauche, M. C. Festou, A. L. Lane, C. J. Hansen, J. N. Maki, R. A. West, H. Jahn, R. Reulke, K. Warlich, D. E. Shemansky, and Y. L. Yung. The Cassini Ultraviolet Imaging Spectrograph Investigation. *Space Science Reviews*, 115:299–361, December 2004.

H. Feuchtgruber, E. Lellouch, B. Bézard, T. Encrenaz, T. de Graauw, and G. R. Davis. Detection of HD in the atmospheres of Uranus and Neptune: a new determination of the D/H ratio. *Astronomy & Astrophysics*, 341: L17–L21, January 1999.

F. M. Flasar, R. K. Achterberg, B. J. Conrath, P. J. Gierasch, V. G. Kunde, C. A. Nixon, G. L. Bjoraker, D. E. Jennings, P. N. Romani, A. A. Simon-Miller, B. Bézard, A. Coustenis, P. G. J. Irwin, N. A. Teanby, J. Brasunas, J. C. Pearl, M. E. Segura, R. C. Carlson, A. Mamoutkine, P. J. Schinder, A. Barucci, R. Courtin, T. Fouchet, D. Gautier, E. Lellouch, A. Marten, R. Prangé, S. Vinatier, D. F. Strobel, S. B. Calcutt, P. L. Read, F. W. Taylor, N. Bowles, R. E. Samuelson, G. S. Orton, L. J. Spilker, T. C. Owen, J. R. Spencer, M. R. Showalter, C. Ferrari, M. M. Abbas, F. Raulin, S. Edgington, P. Ade, and E. H. Wishnow. Titan's Atmospheric Temperatures, Winds, and Composition. *Science*, 308:975–978, May 2005.

W. M. Folkner, S. W. Asmar, J. S. Border, G. W. Franklin, S. G. Finley, J. Gorelik, D. V. Johnston, V. V. Kerzhanovich, S. T. Lowe, R. A. Preston, M. K. Bird, R. Dutta-Roy, M. Allison, D. H. Atkinson, P. Edenhofer,

D. Plettemeier, and G. L. Tyler. Winds on Titan from ground-based tracking of the Huygens probe. *Journal of Geophysical Research (Planets)*, 111: 7–, July 2006.

M. Fulchignoni, F. Ferri, F. Angrilli, A. J. Ball, A. Bar-Nun, M. A. Barucci, C. Bettanini, G. Bianchini, W. Borucki, G. Colombatti, M. Coradini, A. Coustenis, S. Debei, P. Falkner, G. Fanti, E. Flamini, V. Gaborit, R. Grard, M. Hamelin, A. M. Harri, B. Hathi, I. Jernej, M. R. Leese, A. Lehto, P. F. Lion Stoppato, J. J. López-Moreno, T. Mäkinen, J. A. M. McDonnell, C. P. McKay, G. Molina-Cuberos, F. M. Neubauer, V. Pirronello, R. Rodrigo, B. Saggin, K. Schwingenschuh, A. Seiff, F. Simões, H. Svedhem, T. Tokano, M. C. Towner, R. Trautner, P. Withers, and J. C. Zarnecki. In situ measurements of the physical characteristics of Titan's environment. *Nature*, 438:785–791, December 2005.

A. Galli, P. Wurz, H. Lammer, H. I. M. Lichtenegger, R. Lundin, S. Barabash, A. Grigoriev, M. Holmström, and H. Gunell. The Hydrogen Exospheric Density Profile Measured with ASPERA-3/NPD. *Space Science Reviews*, 126:447–467, October 2006.

P. Garnier, I. Dandouras, D. Toublanc, P. C. Brandt, E. C. Roelof, D. G. Mitchell, S. M. Krimigis, N. Krupp, D. C. Hamilton, and H. Waite. The exosphere of Titan and its interaction with the kronian magnetosphere: MIMI observations and modeling. *Planetary and Space Science*, 55:165–173, January 2007.

J. Geiss and H. Reeves. Deuterium in the Solar System. *Astronomy & Astrophysics*, 93:189–199, January 1981.

C. A. Griffith, T. Owen, G. A. Miller, and T. Geballe. Transient clouds in Titan's lower atmosphere. *Nature*, 395:575–578, October 1998.

C. A. Griffith, J. L. Hall, and T. R. Geballe. Detection of Daily Clouds on Titan. *Science*, 290:509–513, October 2000.

C. A. Griffith, P. Penteado, K. Baines, P. Drossart, J. Barnes, G. Bellucci, J. Bibring, R. Brown, B. Buratti, F. Capaccioni, P. Cerroni, R. Clark, M. Combes, A. Coradini, D. Cruikshank, V. Formisano, R. Jaumann, Y. Langevin, D. Matson, T. McCord, V. Mennella, R. Nelson, P. Nicholson, B. Sicardy, C. Sotin, L. A. Soderblom, and R. Kursinski. The Evolution of Titan's Mid-Latitude Clouds. *Science*, 310:474–477, October 2005.

C. A. Griffith, P. Penteado, P. Rannou, R. Brown, V. Boudon, K. H. Baines, R. Clark, P. Drossart, B. Buratti, P. Nicholson, C. P. McKay, A. Coustenis, A. Negrao, and R. Jaumann. Evidence for a Polar Ethane Cloud on Titan. *Science*, 313:1620–1622, September 2006.

J. M. Hammersley and D. C. Handscomb. *Monte Carlo Methods*. Methuen and Co., London, 1964.

J. E. Hansen and L. D. Travis. Light scattering in planetary atmospheres. *Space Science Reviews*, 16:527–610, October 1974.

A.-M. Harri, T. Mäkinen, A. Lehto, H. Kahanpää, and T. Siili. Vertical pressure profile of Titan's observations of the PPI/HASI instrument. *Planetary & Space Sciences*, 54:1117–1123, October 2006.

D. F. Heath and P. A. Sacher. Effects of a simulated high-energy space environment on the ultraviolet transmittance of optical materials between 1050 Å and 3000 Å. *Applied optics*, 5:937–+, June 1966.

L. G. Henyey. The Doppler Effect in Resonance Lines. *Proceedings of the National Academy of Science*, 26:50–54, January 1940.

F. Hersant, D. Gautier, and J.-M. Huré. A Two-dimensional Model for the Primordial Nebula Constrained by D/H Measurements in the Solar System: Implications for the Formation of Giant Planets. *Astrophysical Journal*, 554:391–407, June 2001.

F. Hersant, D. Gautier, G. Tobie, and J. I. Lunine. Interpretation of the carbon abundance in Saturn measured by Cassini. *Planetary & Space Science*, 56:1103–1111, June 2008.

D. A. Hilton and D. M. Hunten. A partially collisional model of the Titan hydrogen torus. *Icarus*, 73:248–268, February 1988.

David C. Hoaglin, Frederick Mosteller, and John W. Tukey, editors. *Understanding robust and exploratory data analysis*. Wiley series in probability and mathematical statistics. Wiley-Interscience, 1983.

R. R. Hodges, Jr. Helium and hydrogen in the lunar atmosphere. *Journal of Geophysical Research*, 78:8055–8064, 1973.

J. Horner, O. Mousis, Y. Alibert, J. I. Lunine, and M. Blanc. Constraints from deuterium on the formation of icy bodies in the Jovian system and beyond. *Planetary & Space Sciences*, 56:1585–1595, November 2008.

L. L. House and L. W. Avery. The Monte Carlo technique applied to radiative transfer. *Journal of Quantitative Spectroscopy and Radiative Transfer*, 9: 1579–1591, 1969.

D. G. Hummer. Non-coherent scattering: I. The redistribution function with Doppler broadening. *Monthly Notices of the Royal Astronomical Society*, 125:21–37, 1962.

D. M. Hunten. The sequestration of ethane on Titan in smog particles. *Nature*, 443:669–670, October 2006.

W. T. Hutzell, C. P. McKay, and O. B. Toon. Effects of Time-Varying Haze Production on Titan's Geometric Albedo. *Icarus*, 105:162–174, September 1993.

A. P. Ingersoll, H. G. Roe, E. L. Schaller, and M. E. Brown. Scale Analysis of Convective Activity on Titan: Is the Surface Setting the Time Scale? In *Bulletin of the American Astronomical Society*, volume 37 of *Bulletin of the American Astronomical Society*, pages 719–+, August 2005.

R. A. Jacobson, P. G. Antreasian, J. J. Bordi, K. E. Criddle, R. Ionasescu, J. B. Jones, R. A. Mackenzie, M. C. Meek, D. Parcher, F. J. Pelletier, W. M. Owen, Jr., D. C. Roth, I. M. Roundhill, and J. R. Stauch. The Gravity Field of the Saturnian System from Satellite Observations and Spacecraft Tracking Data. *Astronomical Journal*, 132:2520–2526, December 2006.

L. Kaltenegger, W. A. Traub, and K. W. Jucks. Spectral Evolution of an Earth-like Planet. *Astrophysical Journal*, 658:598–616, March 2007.

H. U. Keller, B. Grieger, M. Küppers, S. E. Schröder, Y. V. Skorov, and M. G. Tomasko. The properties of Titan's surface at the Huygens landing site from DISR observations. *Planetary & Space Sciences*, 56:728–752, April 2008.

V. A. Krasnopolsky. A photochemical model of Titan's atmosphere and ionosphere. *Icarus*, 201:226–256, May 2009.

H. Lammer, W. Stumptner, and S. J. Bauer. Dynamic escape of H from Titan as consequence of sputtering induced heating. *Planetary & Space Sciences*, 46:1207–1213, October 1998.

L. M. Lara, E. Lellouch, J. J. López-Moreno, and R. Rodrigo. Vertical distribution of Titan's atmospheric neutral constituents. *Journal of Geophysical Research*, 101, 1996.

S. Lebonnois, D. Toublanc, F. Hourdin, and P. Rannou. Seasonal Variations of Titan's Atmospheric Composition. *Icarus*, 152:384–406, August 2001.

S. É. Lebonnois, E. L. O. Bakes, and C. P. McKay. Atomic and molecular hydrogen budget in Titan's atmosphere. *Icarus*, 161:474–485, February 2003.

C. Lécuyer, P. Grandjean, J.-A. Barrat, J. Nolvak, C. Emig, F. Paris, and M. Robardet. δ18O and REE contents of phosphatic brachiopods: a comparison between modern and lower Paleozoic populations. *Geochimica et Cosmochimica Acta*, 62:2429–2436, July 1998.

J.-S. Lee. Simulation of emission frequencies from angle-dependent partial frequency redistributions. *Astrophysical Journal*, 218:857–865, December 1977.

J.-S. Lee and R. R. Meier. Angle-dependent frequency redistribution in a plane-parallel medium - External source case. *Astrophysical Journal*, 240: 185–195, August 1980.

E. Lellouch, D. M. Hunten, G. Kockarts, and A. Coustenis. Titan's thermosphere profile. *Icarus*, 83:308–324, February 1990.

E. Lellouch, B. Bézard, T. Fouchet, H. Feuchtgruber, T. Encrenaz, and T. de Graauw. The deuterium abundance in Jupiter and Saturn from ISO-SWS observations. *Astronomy & Astrophysics*, 370:610–622, May 2001.

G. F. Lindal, G. E. Wood, H. B. Hotz, D. N. Sweetnam, V. R. Eshleman, and G. L. Tyler. The atmosphere of Titan - an analysis of the Voyager 1 radio occultation measurements. *Icarus*, 53:348–363, February 1983.

R. Lorenz. The weather on Titan. *Science*, 290(5491):467–468, October 2000.

R. D. Lorenz, J. C. Zarnecki, M. C. Towner, M. R. Leese, A. J. Ball, B. Hathi, A. Hagermann, and N. A. L. Ghafoor. Descent motions of the Huygens probe as measured by the Surface Science Package (SSP): Turbulent evidence for a cloud layer. *Planetary & Space Sciences*, 55:1936–1948, November 2007.

J. I. Lunine and W. C. Tittemore. Origins of outer-planet satellites. In E. H. Levy and J. I. Lunine, editors, *Protostars and Planets III*, pages 1149–1176, 1993.

J. I. Lunine, D. J. Stevenson, and Y. L. Yung. Ethane ocean on Titan. *Science*, 222:1229–+, December 1983.

J. I. Lunine, Y. L. Yung, and R. D. Lorenz. On the volatile inventory of Titan from isotopic abundances in nitrogen and methane. *Planetary & Space Sciences*, 47:1291–1303, October 1999.

J. N. Maki. *The Hydrogen Deuterium Absorption Cell in the Cassini Spacecraft: A Remote Sensing Instrument for Atomic D/H Measurements on Saturn and Titan.* PhD thesis, University of Colorado, 1993.

M. Mayor and D. Queloz. A Jupiter-Mass Companion to a Solar-Type Star. *Nature*, 378:355–+, November 1995.

T. R. McDonough and N. M. Brice. A Saturnian Gas Ring and the Recycling of Titan's Atmosphere. *Icarus*, 20:136–+, October 1973.

R. Meier, T. C. Owen, H. E. Matthews, D. C. Jewitt, D. Bockelee-Morvan, N. Biver, M. Senay, J. Crovisier, and D. Gautier. Deuterium in Comet C/1995 O1 (Hale-Bopp). In *Bulletin of the American Astronomical Society*, volume 29 of *Bulletin of the American Astronomical Society*, July 1997.

R. R. Meier and J.-S. Lee. A Monte Carlo Study of Frequency Redistribution in an Externally Excited Medium. *Astrophysical Journal*, 219:262–273, January 1978.

M. Michael and R. E. Johnson. Energy deposition of pickup ions and heating of Titan's atmosphere. *Planetary & Space Sciences*, 53:1510–1514, December 2005.

D. Mihalas. *Stellar atmospheres (2nd edition)*. San Francisco, W. H. Freeman and Co., 1978.

H. W. Moos, K. R. Sembach, A. Vidal-Madjar, D. G. York, S. D. Friedman, G. Hébrard, J. W. Kruk, N. Lehner, M. Lemoine, G. Sonneborn, B. E. Wood, T. B. Ake, M. André, W. P. Blair, P. Chayer, C. Gry, A. K. Dupree, R. Ferlet, P. D. Feldman, J. C. Green, J. C. Howk, J. B. Hutchings, E. B. Jenkins, J. L. Linsky, E. M. Murphy, W. R. Oegerle, C. Oliveira, K. Roth, D. J. Sahnow, B. D. Savage, J. M. Shull, T. M. Tripp, E. J. Weiler, B. Y. Welsh, E. Wilkinson, and B. E. Woodgate. Abundances of Deuterium,

Nitrogen, and Oxygen in the Local Interstellar Medium: Overview of First Results from the FUSE Mission. *Astrophysical Journal Supplement Series*, 140:3–17, May 2002.

D. H. Mordaunt, I. R. Lambert, G. P. Morley, M. N. R. Ashfold, R. N. Dixon, C. M. Western, L. Schnieder, and K. H. Welge. Primary product channels in the photodissociation of methane at 121.6 NM. *J. Chem. Phys.*, 98: 2054–2065, 1993.

O. Mousis, D. Gautier, and A. Coustenis. The D/H Ratio in Methane in Titan: Origin and History. *Icarus*, 159:156–165, September 2002.

A. F. Nagy, Y. Liu, K. C. Hansen, K. Kabin, T. I. Gombosi, M. R. Combi, D. L. DeZeeuw, K. G. Powell, and A. J. Kliore. The interaction between the magnetosphere of Saturn and Titan's ionosphere. *Journal of Geophysical Research*, 106:6151–6160, April 2001.

C. D. Neish, Á. Somogyi, J. I. Lunine, and M. A. Smith. Low temperature hydrolysis of laboratory tholins in ammonia-water solutions: Implications for prebiotic chemistry on Titan. *Icarus*, 201:412–421, May 2009.

H. B. Niemann, S. K. Atreya, S. J. Bauer, G. R. Carignan, J. E. Demick, R. L. Frost, D. Gautier, J. A. Haberman, D. N. Harpold, D. M. Hunten, G. Israel, J. I. Lunine, W. T. Kasprzak, T. C. Owen, M. Paulkovich, F. Raulin, E. Raaen, and S. H. Way. The abundances of constituents of Titan's atmosphere from the GCMS instrument on the Huygens probe. *Nature*, 438:779–784, December 2005.

E. J. Öpik and S. F. Singer. Distribution of Density in a Planetary Exosphere. II. *Physics of Fluids*, 4:221–233, February 1961.

G. Orton. Ground-based observations of Titan's thermal spectrum. In B. Kaldeich, editor, *Symposium on Titan*, volume 338 of *ESA Special Publication*, pages 81–85, April 1992.

T. Owen. The search for other planets: Clues from the Solar System. *Astrophysics & Space Science*, 212:1–2, February 1994.

T. Owen, J. P. Maillard, C. de Bergh, and B. L. Lutz. Deuterium on Mars - The abundance of HDO and the value of D/H. *Science*, 240:1767–1770, June 1988.

C. K. Pankratz, B. G. Knapp, R. A. Reukauf, J. Fontenla, M. A. Dorey, L. M. Connelly, and A. K. Windnagel. The SORCE Science Data System. *Solar Physics*, 230:389–413, August 2005. doi: 10.1007/s11207-005-5008-4.

S. K. Park and K. W. Miller. Random number generators: good ones are hard to find. *Commun. ACM*, 31(10), 1988.

P. F. Penteado, C. A. Griffith, T. K. Greathouse, and C. de Bergh. Measurements of CH_3D and CH_4 in Titan from Infrared Spectroscopy. *The Astrophysical Journal*, 629:L53–L56, August 2005.

J. P. Pinto, J. I. Lunine, S.-J. Kim, and Y. L. Yung. D to H ratio and the origin and evolution of Titan's atmosphere. *Nature*, 319:388–390, January 1986.

C. C. Porco, E. Baker, J. Barbara, K. Beurle, A. Brahic, J. A. Burns, S. Charnoz, N. Cooper, D. D. Dawson, A. D. Del Genio, T. Denk, L. Dones, U. Dyudina, M. W. Evans, S. Fussner, B. Giese, K. Grazier, P. Helfenstein, A. P. Ingersoll, R. A. Jacobson, T. V. Johnson, A. McEwen, C. D. Murray, G. Neukum, W. M. Owen, J. Perry, T. Roatsch, J. Spitale, S. Squyres, P. Thomas, M. Tiscareno, E. P. Turtle, A. R. Vasavada, J. Veverka, R. Wagner, and R. West. Imaging of Titan from the Cassini spacecraft. *Nature*, 434:159–168, March 2005.

W. H. Press, B. P. Flannery, S. A. Teukolsky, and W. T. Vetterling. *Numerical Recipes in C : The Art of Scientific Computing*. Cambridge University Press, October 1992.

K. Rages and J. B. Pollack. Vertical distribution of scattering hazes in Titan's upper atmosphere. *Icarus*, 55:50–62, July 1983.

R. L. Rairden, L. A. Frank, and J. D. Craven. Geocoronal imaging with Dynamics Explorer. *Journal of Geophysical Research*, 91:13613–13630, December 1986.

P. Rannou, F. Hourdin, and C. P. McKay. A wind origin for Titan's haze structure. *Nature*, 418:853–856, August 2002.

F. Raulin. Astrobiology and habitability of Titan. *Space Science Reviews*, 135:37–48, March 2008.

M. Regehly. Characterization and Verification of the Hydrogen Deuterium Absorption Cell. Master's thesis, Humboldt University, Berlin, 2003.

F. Robert, D. Gautier, and B. Dubrulle. The Solar System D/H Ratio: Observations and Theories. *Space Science Reviews*, 92:201–224, April 2000.

R. E. Samuelson. Radiative equilibrium model of Titan's atmosphere. *Icarus*, 53:364–387, February 1983.

A. Segura, K. Krelove, J. F. Kasting, D. Sommerlatt, V. Meadows, D. Crisp, M. Cohen, and E. Mlawer. Ozone Concentrations and Ultraviolet Fluxes on Earth-Like Planets Around Other Stars. *Astrobiology*, 3:689–708, December 2003.

N. N. Shefov. Photon scattering coefficients for H2O+ molecules. *Soviet Astronomy*, 28:70–72, February 1984.

M. B. Simakov. The possible sites for exobiological activity on Titan. In P. Ehrenfreund, O. Angerer, and B. Battrick, editors, *Exo-/Astro-Biology*, volume 496 of *ESA Special Publication*, pages 211–214, August 2001.

B. A. Smith, L. Soderblom, R. F. Beebe, J. M. Boyce, G. Briggs, A. Bunker, S. A. Collins, C. Hansen, T. V. Johnson, J. L. Mitchell, R. J. Terrile, M. H. Carr, A. F. Cook, J. N. Cuzzi, J. B. Pollack, G. E. Danielson, A. P. Ingersoll, M. E. Davies, G. E. Hunt, H. Masursky, E. M. Shoemaker, D. Morrison, T. Owen, C. Sagan, J. Veverka, R. Strom, and V. E. Suomi. Encounter with Saturn - Voyager 1 imaging science results. *Science*, 212: 163–191, April 1981.

B. A. Smith, L. Soderblom, R. Batson, P. Bridges, J. Inge, H. Masursky, E. Shoemaker, R. Beebe, J. Boyce, G. Briggs, A. Bunker, S. A. Collins, C. J. Hansen, T. V. Johnson, J. L. Mitchell, R. J. Terrile, A. F. Cook, J. Cuzzi, J. B. Pollack, G. E. Danielson, A. Ingersoll, M. E. Davies, G. E. Hunt, D. Morrison, T. Owen, C. Sagan, J. Veverka, R. Strom, and V. E. Suomi. A new look at the Saturn system: The Voyager 2 images. *Science*, 215:505–537, January 1982.

W. H. Smyth. Titan's hydrogen torus. *Astrophysical Journal*, 246:344–353, May 1981.

L. A. Soderblom, M. G. Tomasko, B. A. Archinal, T. L. Becker, M. W. Bushroe, D. A. Cook, L. R. Doose, D. M. Galuszka, T. M. Hare, E. Howington-Kraus, E. Karkoschka, R. L. Kirk, J. I. Lunine, E. A. McFarlane, B. L. Redding, B. Rizk, M. R. Rosiek, C. See, and P. H. Smith. Topography and geomorphology of the Huygens landing site on Titan. *Planetary & Space Sciences*, 55:2015–2024, November 2007.

N. Teanby. Planetary atmospheres: Cassini at Titan: the story so far. *Astronomy and Geophysics*, 46(5), October 2005.

G. E. Thomas. Lyman α Scattering in the Earth's Hydrogen Geocorona, 1. *Journal of Geophysical Research*, 68:2639–+, May 1963.

G. Tobie, J. I. Lunine, and C. Sotin. Episodic outgassing as the origin of atmospheric methane on Titan. *Nature*, 440:61–64, March 2006.

T. Tokano and F. M. Neubauer. Tidal Winds on Titan Caused by Saturn. *Icarus*, 158:499–515, August 2002.

D. Toublanc, J. P. Parisot, J. Brillet, D. Gautier, F. Raulin, and C. P. McKay. Photochemical modeling of Titan's atmosphere. *Icarus*, 113:2–26, January 1995.

S. Udry, X. Bonfils, X. Delfosse, T. Forveille, M. Mayor, C. Perrier, F. Bouchy, C. Lovis, F. Pepe, D. Queloz, and J.-L. Bertaux. The HARPS search for southern extra-solar planets. XI. Super-Earths (5 and 8 $M_{\oplus}$) in a 3-planet system. *A&A*, 469:L43–L47, July 2007.

R. K. Vatsa and H.-R. Volpp. Absorption Cross Sections for Some Atmospherically Important Molecules at the H Atom Lyman-a Wavelength (121.567 nm) . *Chemical Physical Letters*, 340:289–295, June 2001.

R. J. Vervack, B. R. Sandel, and D. F. Strobel. New perspectives on Titan's upper atmosphere from a reanalysis of the Voyager 1 UVS solar occultations. *Icarus*, 170:91–112, July 2004.

V. Vuitton, R. V. Yelle, and J. Cui. Formation and distribution of benzene on Titan. *Journal of Geophysical Research (Planets)*, 113(E12):5007–+, May 2008.

K. Warlich. *Simulation and Optimization of the Hydrogen-Deuterium-Absorption-Cell Experiment on Cassini*. PhD thesis, Technical University Berlin, 1997.

E. H. Wilson and S. K. Atreya. Chemical sources of haze formation in Titan's atmosphere. *Planetary & Space Sciences*, 51:1017–1033, December 2003.

E. H. Wilson and S. K. Atreya. Current state of modeling the photochemistry of Titan's mutually dependent atmosphere and ionosphere. *Journal of Geophysical Research (Planets)*, 109:6002, June 2004.

J. H. Wolfe, J. D. Mihalov, H. R. Collard, D. D. McKibbin, L. A. Frank, and D. S. Intriligator. Preliminary results on the plasma environment of Saturn from the Pioneer 11 plasma analyzer experiment. *Science*, 207: 403–407, January 1980.

A. Wolszczan and D. A. Frail. A planetary system around the millisecond pulsar PSR1257 + 12. *Nature*, 355:145–147, January 1992.

P. Wurz and H. Lammer. Monte-Carlo simulation of Mercury's exosphere. *Icarus*, 164:1–13, July 2003.

R. V. Yelle, D. F. Strobel, E. Lellouch, and D. Gautier. Engineering Models for Titan's atmosphere. (ESA SP-1178, European Space Agency, Noordwijk), 1997.

Y. L. Yung. An update of nitrile photochemistry on Titan. *Icarus*, 72: 468–472, November 1987.

Y. L. Yung, M. Allen, and J. P. Pinto. Photochemistry of the atmosphere of Titan - Comparison between model and observations. *Astrophysical Journal Supplement Series*, 55:465–506, July 1984.

M. Zelen and N.C. Severo. Probability functions. In Abramowitz, M.,Stegun, A. , editor, *Handbook of Mathematical Functions*, 1965.

Danksagung

An erster Stelle möchte ich mich bei Prof. H. Rauer für die Möglichkeit bedanken, diese interessante Doktorarbeit am Deutschen Zentrum für Luft und Raumfahrt anzufertigen. Weiterhin bedanke ich mich bei Prof. E. Sedlmayr für die Anfertigung des Zweitgutachtens dieser Arbeit.
Prof. L. Esposito, Prof. U. Keller und Prof. R. Reulke danke ich für die Bereitstellung der HDAC Daten, ohne die die gesamte Arbeit in dieser Form nicht möglich gewesen wäre. Yuichi Ito danke ich für die anfängliche Hilfe beim Progammieren des Monte Carlo Modells.
Helmut Lammer, Peter Wurz und Audrey Schaufelberger danke ich für die Berechnung der Exosphärendichten mit ihrem Teilchenmodell, ohne das keine exakte Berechnungen der Exospärendichten möglich gewesen wäre.
Besonderer Dank gilt meinen Arbeitskollegen am DLR und an der TU Berlin, insbesondere Philip von Paris, der immer für eine wissenschaftliche Diskussion aber auch bei Problemen mit Rat und Tat zur Verfügung stand. Auch Joachim Stock sei an dieser Stelle ein besonderer Dank ausgesprochen für die vielen anregenden Diskussionen und Tipps bei kleineren und größeren Problemen, sowie für die Hilfestellung beim Lösen der Strahlungstransportgleichung. Bei Letzterem ist auch die Hilfe von Dr. Beate Patzer und Daniel Kitzmann hervorzuheben.
Ich danke Anders Erikson, Lee Grenfell, Beate Patzer, Philip von Paris und Joachim Stock für das Gegenlesen dieser Arbeit.
Barbara Stracke möchte ich an dieser Stelle für das lockere Arbeitsklima in unserem Büro und die chaotischen Freitag-Nachmittage danken. Allen hier nicht namentlich genannten Mitarbeitern sei natürlich auch für die angenehme Arbeitsatmosphäre während der vergangenen Jahre gedankt.
Meiner Familie, insbesonders meiner geliebten Frau Jasmina und meiner süßen Tochter Amy Rose, gilt besonderer Dank für ihre Liebe und Unterstützung während der gesamten Arbeit, sowie auch für ihren Rückhalt und Motivation in schwierigen Momenten.